AD-A049 779 HARVARD UNIV CAMBRIDGE MA DIV OF APPLIED SCIENCES F/G 9/5
NONEQUILIBRIUM PROPERTIES OF VARIABLE-THICKNESS SUPERCONDUCTING--ETC(U)
JAN 78 M OCTAVIO N00014-77-C-0085
UNCLASSIFIED TR-13 NL

1 OF 3
AD A049779

AD A049779
AD No.
DDC FILE COPY

Office of Naval Research
Contract N00014-77-C-0085 NR-318-003
Contract N00014-75-C-0648
National Science Foundation Grant DMR76-11323

NONEQUILIBRIUM PROPERTIES OF VARIABLE-THICKNESS SUPERCONDUCTING MICROBRIDGES

DDC
FEB 9 1978
F

By
Miguel Octavio

January 1978

Technical Report No. 13

This document has been approved for public release and sale; its distribution is unlimited. Reproduction in whole or in part is permitted by the U. S. Government.

Division of Applied Sciences
Harvard University Cambridge, Massachusetts

Unclassified

SECURITY CLASSIFICATION OF THIS PAGE (When Data Entered)

REPORT DOCUMENTATION PAGE	READ INSTRUCTIONS BEFORE COMPLETING FORM
1. REPORT NUMBER (14) TR- Technical Report No. 13	2. GOVT ACCESSION NO.
3. RECIPIENT'S CATALOG NUMBER (9)	
4. TITLE (and Subtitle) (6) NONEQUILIBRIUM PROPERTIES OF VARIABLE-THICKNESS SUPERCONDUCTING MICRO-BRIDGES.	5. TYPE OF REPORT & PERIOD COVERED Interim Report.
	6. PERFORMING ORG. REPORT NUMBER
7. AUTHOR(s) (10) Miguel Octavio	8. CONTRACT OR GRANT NUMBER(s) (15) N00014-77-C-0085, N00014-75-C-0648, NSF DMR76-11323
9. PERFORMING ORGANIZATION NAME AND ADDRESS Division of Applied Sciences Harvard University Cambridge, Massachusetts 02138	10. PROGRAM ELEMENT, PROJECT, TASK AREA & WORK UNIT NUMBERS
11. CONTROLLING OFFICE NAME AND ADDRESS (11)	12. REPORT DATE January 1978
	13. NUMBER OF PAGES 206
14. MONITORING AGENCY NAME & ADDRESS (if different from Controlling Office) (12) 207 p.	15. SECURITY CLASS. (of this report)
	15a. DECLASSIFICATION/DOWNGRADING SCHEDULE

16. DISTRIBUTION STATEMENT (of this Report)

Approved for public release; distribution unlimited.

DDC RECEIVED FEB 9 1978 F

17. DISTRIBUTION STATEMENT (of the abstract entered in Block 20, if different from Report)

18. SUPPLEMENTARY NOTES

19. KEY WORDS (Continue on reverse side if necessary and identify by block number)

Superconductivity
Josephson Effects
Thin-Film Microbridges
Nonequilibrium Effects
Microwave and Far Infrared Detectors

20. ABSTRACT (Continue on reverse side if necessary and identify by block number)

The experimental properties of tin and lead variable-thickness microbridges have been investigated. We find that the dc I-V characteristics and the high frequency response of these Josephson devices are determined or modified by nonequilibrium effects. → next page

We find that the improved cooling of the variable-thickness geometry allows us to observe microwave-induced Josephson steps to voltages as high as 4.2 mV, a factor of 4 improvement over conventional thin-film microbridges. This

DD FORM 1 JAN 73 1473 EDITION OF 1 NOV 65 IS OBSOLETE S/N 0102-014-6601

410 457

Unclassified

SECURITY CLASSIFICATION OF THIS PAGE (When Data Entered)

Abstract continued

improved performance is analyzed in terms of a simple heating approximation for three-dimensional weak links. From this analysis we find that the critical current decreases with the dissipated power P as e^{-P/P_o} where P_o is a material- and temperature-dependent parameter. This prediction of the heating model is found to be in very good agreement with the reduction of the amplitude of the microwave-induced ac steps at all voltages as well as the temperature dependence of the maximum voltage at which these steps are observed.

We use the gap and the subharmonic gap structure observed in the dc I-V characteristics of our microbridges as a local thermometer in order to demonstrate the correlation between low dissipation, reduced hysteresis, and the good high frequency performance of our variable-thickness microbridges.

Measurement of low voltage foot-like features of the I-V characteristics are found to be consistent with a voltage-dependent enhancement of the supercurrent induced by the disequilibrium of the quasi-particles during the Josephson cycle. Comparison of the experimental data with the predictions of the models of Golub and of Aslamazov and Larkin show many points of agreement in the regimes where these theories are applicable.

We also report on the general characteristics of these devices such as the magnitude and temperature dependence on the critical currents, $I_{co}R_N$ products, and the Wyatt-Dayem effect. Exploratory experiments on series arrays of microbridges and detection of far-infrared radiation are also discussed.

ACCESSION for
NTIS
DDC
UNANNOUNCED
JUSTIFICATION
BY
DISTRIBUTION/AVAILABILITY CODES
Dist.
A

Office of Naval Research

Contract N00014-77-C-0085 NR-318-003

Contract N00014-75-C-0648

National Science Foundation Grant DMR76-11323

NONEQUILIBRIUM PROPERTIES OF VARIABLE-THICKNESS SUPERCONDUCTING MICROBRIDGES

By

Miguel Octavio

Technical Report No. 13

Reproduction in whole or in part is permitted for any purpose of the United States Government. Approved for public release; distribution unlimited.

The research reported in this document was made possible through support extended the Division of Applied Sciences, Harvard University, by the Office of Naval Research, under Contract N00014-77-C-0085, Contract N00014-75-C-0648 and by the National Science Foundation under Grant DMR76-11323.

Division of Applied Sciences

Harvard University · Cambridge, Massachusetts

ABSTRACT

The experimental properties of tin and lead variable-thickness microbridges have been investigated. We find that the dc I-V characteristics and the high frequency response of these Josephson devices are determined or modified by nonequilibrium effects.

We find that the improved cooling of the variable-thickness geometry allows us to observe microwave-induced Josephson steps to voltages as high as 4.2 mV, a factor of 4 improvement over conventional thin-film microbridges. This improved performance is analyzed in terms of a simple heating approximation for three-dimensional weak links. From this analysis we find that the critical current decreases with the dissipated power P as e^{-P/P_o} where P_o is a material- and temperature-dependent parameter. This prediction of the heating model is found to be in very good agreement with the reduction of the amplitude of the microwave-induced ac steps at all voltages as well as the temperature dependence of the maximum voltage at which these steps are observed.

We use the gap and the subharmonic gap structure observed in the dc I-V characteristics of our microbridges as a local thermometer in order to demonstrate the correlation between low dissipation, reduced hysteresis, and the good high frequency performance of our variable-thickness microbridges.

Measurement of low voltage foot-like features of the I-V characteristics are found to be consistent with a voltage-dependent enhancement of the supercurrent induced by the disequilibrium of the quasi-particles during the Josephson cycle. Comparison of the experimental data with the predictions of the models of Golub and of Aslamazov and Larkin show many points of agreement in the regimes where these theories are applicable.

We also report on the general characteristics of these devices such as the magnitude and temperature dependence on the critical currents, $I_{co}R_N$ products, and the Wyatt-Dayem effect. Exploratory experiments on series arrays of micro-bridges and detection of far-infrared radiation are also discussed.

TABLE OF CONTENTS

		Page
	ABSTRACT	i
	LIST OF FIGURES	v
	LIST OF TABLES	x
I.	INTRODUCTION	1
II.	EXPERIMENTAL TECHNIQUES	10
	2.1 Sample Preparation	10
	2.2 Experimental Details	18
III.	STATIC PROPERTIES OF VARIABLE-THICKNESS SUPERCONDUCTING MICROBRIDGES: CRITICAL CURRENTS AND $I_{co}R_N$ PRODUCTS	23
	3.1 The Critical Current	24
	3.1.1 Regime Close to T_c	24
	3.1.2 Low Temperature Regime: $I_{co}R_N$ Products	40
	3.2 The Wyatt-Dayem Effect	43
IV.	NONEQUILIBRIUM ENHANCED SUPERCURRENTS AT NONZERO VOLTAGES	51
	4.1 Introduction	51
	4.2 The Experimental Phenomena	52
	4.3 Theoretical Interpretation	56
	4.3.1 Qualitative Picture	58
	4.3.2 Golub's Theory	64
	4.3.3 The Theory of Aslamazov and Larkin .	84
	4.4 Discussion of Experimental Results . .	87
V.	HIGH-FREQUENCY PROPERTIES OF VARIABLE-THICKNESS MICROBRIDGES	102
	5.1 The ac Josephson Effect and Variable-Thickness Microbridges	104
	5.2 The Heating Model	116

Table of Contents (Continued) Page

5.2.1 Introduction 116
5.2.2 Reduction of I_{co} by Heating 119
5.2.3 The Variable-Thickness Geometry . . 123
5.2.4 Voltage Limit for Microwave-Induced Steps: Temperature and Material Dependence 126
5.2.5 Heating Effects at Low Voltages . . 136
5.2.6 Optimum Design of Thin-Film Microbridges for High Frequency Applications 143

5.3 Further Evidence of the Well-Cooled Nature of the Variable-Thickness Geometry 145

5.3.1 Hysteresis 145
5.3.2 The Subharmonic Gap Structure . . . 149

VI. OTHER TOPICS 163

6.1 Detection of Far-Infrared Radiation with Variable-Thickness Microbridges . . . 163
6.2 Arrays of Microbridges in Series . . . 168

VII. CONCLUSIONS 174

APPENDIX A. CHARACTERISTIC PROPERTIES OF TIN AND LEAD MICROBRIDGES USED IN THIS REPORT . 183

REFERENCES 187

ACKNOWLEDGEMENTS 193

LIST OF FIGURES

Figure		Page
1.1	a) Long Microbridge; b) Two-dimensional, uniform thickness microbridge; c) Variable-thickness microbridge	2
1.2	I-V characteristics of: a) well-cooled microbridge (#9); b) Very Well cooled microbridge (#11)	6
2.1	Schematic of bridge fabrication	15
2.2	Scanning electron micrographs of a bridge. Top: Overview of bridge and banks. Bottom: close-up of the microbridge	16
2.3	Circuits used in measuring a) I-V characteristics; b) dI/dV versus V	19
3.1	Schematic of a) hyperbolic neck geometry; b) collinear cone geometry	28
3.2	Critical currents near T_c for two variable-thickness microbridges (#22 and #21) . . Inset shows the critical currents very close to T_c	36
3.3	Critical currents for a lead variable-thickness microbridge	39
3.4	$I_{co}R_N$ products vs. R_N for tin variable-thickness microbridges	42
3.5	Enhancement of the critical currents at 10 and 32 GHz for bridge #21	46
4.1	I-V characteristics as a function of temperature for bridge #3. The inset defines the equilibrium critical current I_{co}, the excess supercurrent $\overline{I}_s$, and the maximum enhanced supercurrent I_{c1}. The dotted curves show the shape above I_{c1} predicted by Aslamazov and Larkin	53

List of Figures (Continued)

Figure		Page
4.2	Low voltage part of the I-V characteristics of Fig. 4.1 showing the development of the foot as a function of temperature	55
4.3	a) Spatial variation of the gap in the middle of the Josephson cycle showing the quasiparticle states that can not diffuse into the banks. b) Temporal variation of the gap in equilibrium (solid line) and in the presence of a lag (dashed line). c) Temporal variation of excitation energy E_k for $\epsilon_k = \Delta_o/2$. d) Temporal variation of the quasi-particles occupation numbers for different values of the Josephson period relative to τ_E	60
4.4	The functions N_1, N_2 and R_2 as a function of E/Δ for different values of $\tau_E\Delta$; a) $\tau_E\Delta = 1$; b) $\tau_E\Delta = 5$; c) $\tau_E\Delta = 25$	67
4.5	Shape of the longitudinal correction f_L to the equilibrium distribution function f_o as a function of E/Δ. The inset shows the overall distribution function with the nonequilibrium correction greatly exaggerated for the cases $d\Delta/dt > 0$ and $d\Delta/dt < 0$	72
4.6	Variation of I_γ with $\tau_E\Delta$	74
4.7	Plot of the complex parameter at equal time intervals; each line corresponds to the values of the order parameter along the length of the bridge. a)Equilibrium case $u_T = u_L = 0$; b) Nonequilibrium case for $u_T = d\bar{\varphi}_o/dt$ $u_L = 5$	75
4.8	Plot of the magnitude of the order parameter as a function of space and time. The solid lines correspond to the first half of the cycle with the order parameter decreasing and the dashed lines to the second half of the cycle when the order parameter increases.	

List of Figures (Continued)

Figure		Page
	There is a one-to-one correspondence between these curves and those shown in Fig. 4.7. a) $u_T = u_L = 0$; b) $u_T = 0$, $d\bar{\varphi}_o/dt\ u_L = 0$	78
4.9	Correction to the total supercurrent at low voltages.	81
4.10	Spatial and temporal variation of the phase for a) equilibrium case $u_L = u_T = 0$; b) $u_T = 0$, $d\bar{\varphi}_o/dt\ u_L = 5$. In the second plot one curve has been removed in the regime where the approximation $\Psi_o >> \Psi_1$ breaks down	82
4.11	Predictions of the model of Golub for the normalized resistance of the foot as a function of temperature for different values of the bridge length. The solid lines correspond to $\tau_E = 8 \times 10^{-10}$ seconds and the dashed lines to 2×10^{-10} seconds.	88
4.12	The normalized differential resistance of the foot versus temperature. The data points are for six different microbridges and the dashed curves are Golub's predictions for several values of the length parameter L	90
4.13	The ratio of the enhanced supercurrent I_{c1} to the equilibrium critical current I_{co} as a function of temperature for the same bridges as in Fig. 4.12. The dashed curves correspond to the Aslamazov and Larkin prediction, for different values of KL where $K \sim 1$	93
4.14	The currents I_{c1} and I_{co} for bridge #22, showing the saturation of the growth of I_{c1} at temperatures far from T_c. The dashed lines indicate the regime of the Aslamazov and Larkin theory	94

List of Figures (Continued)

Figure		Page
4.15	Plots of the equilibrium critical current I_{co}, the excess supercurrent $\bar{I}_s$, and the enhanced supercurrent I_{c1} as a function of temperature for bridge #3	97
4.16	I-V characteristics of a lead microbridge (L-2) close to the critical temperature .	100
5.1	Response of bridge #3 to 32 GHz radiation. The Josephson voltage corresponds to 66 μV. Attenuation values are negative	107
5.2	Full step widths normalized to the critical current I_{co} for the first 10 steps at 10 GHz	109
5.3	Step amplitudes at 10 GHz for different values of P_o compared with the experimental amplitudes for tin bridge #11	127
5.4	Temperature dependence of $P_o(T)$ for a high performance microbridge (Bridge #16) . . .	132
5.5	Experimental values of the maximum width of the first Josephson step as a function of the normalized frequency. The solid line corresponds to the predictions of the current-biased RSJ model	137
5.6	Effects of heating on the maximum width of the first Josephson step for different values of $\alpha = 1.5 \hbar\omega/4e^2R_NP_o$, assuming the dissipated power is V^2/R_N at the step . .	139
5.7	Effects of heating on the second maximum of the width of the first ac step as a function of frequency for different values of P_oR_N . .	141
5.8	Schematic of a bilayer microbridge for improved high frequency performance . . .	146
5.9	I-V characteristics of a) well cooled microbridge (#9); b) very well cooled microbridge (#11)	148

List of Figures (Continued)

Figure		Page
5.10	Derivative curves showing the variation of the subharmonic gap structure with temperature (Bridge #4)	151
5.11	Gap values determined from the subharmonic gap structure: a) bridge #11; b) bridge #4; c) low voltage limits from (a) and (b) compared to the BCS theory (solid line) .	152
5.12	Inferred temperature rise from the gap and n = 2 subharmonic of bridge #4 as a function of the power dissipated	154
5.13	Dependence of the temperature rise inferred from the gap and subharmonic gap structure on the power dissipated (bridges #4 and #11)	157
5.14	Shape of the gap structure for various bridges with different degrees of cooling at $T/T_c \sim 0.885$	159
6.1	a) I-V characteristic of bridge #17; b) Response I_{ac} of the same bridge to far-infrared radiation. The inset shows the antenna geometry	164
6.2	Response of a high resistance pair of microbridges to 32 GHz radiation	172

LIST OF TABLES

Table		Page
3.1	Characteristic Properties of some tin variable-thickness microbridges	32
3.2	Comparison of the Wyatt-Dayem effect observed in different materials and geometries	49
4.1	Foot parameters for a selection of tin microbridges	98
5.1	Some characteristic properties of representative tin microbridges	112
5.2	Some characteristic properties of lead microbridges	114
5.3	Parameters for the best performance obtained in variable-thickness microbridges of different materials	134
5.4	Values of V_{max} and V_1 for a selection of tin microbridges	155

CHAPTER ONE

INTRODUCTION

Superconducting microbridges, in which a superconducting film is narrowed down to a small constriction, are ideal for the study of a large variety of physical phenomena. In very long, narrow microbridges (length L larger than a few μm, width w less than 5 μm), as shown in Fig. 1.1 (a), one has an essentially one-dimensional system in which the superconducting order parameter varies only along the length of the bridge. Thus such bridges provide a simple system for the study of time-dependent, dissipative, nonequilibrium processes in superconductors. For short ($L < 1$ μm) and narrow ($w < 1$ μm) microbridges, in either a two-dimensional (Fig. 1.1 (b)) or variable-thickness geometry (Fig. 1.1 (c)), one can study the conditions for the existence of ideal Josephson behaviour and how this behaviour is modified or limited by nonequilibrium processes.

Despite a considerable amount of work, the understanding of these weak superconducting systems has progressed slowly mainly due to the complex behaviour of nonequilibrium superconductors. In the case of short microbridges, of interest in this work, it became clear in the earlier work of Dayem and Anderson[1] that many of the properties of bridges could be attributed to some extent to Josephson behaviour.

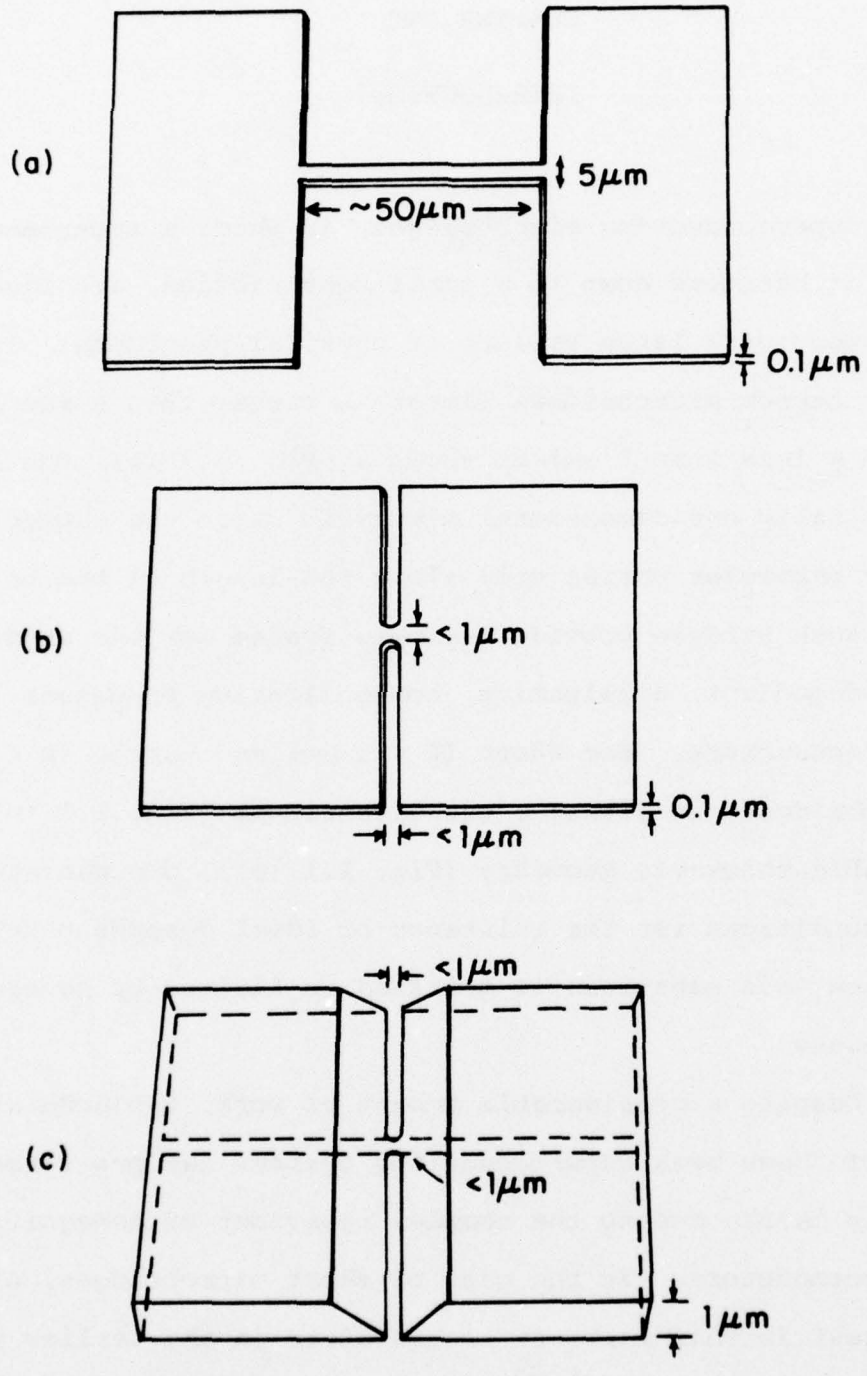

Fig. 1.1 a) Long microbridge; b) Two-dimensional, uniform-thickness microbridge; c) Variable-thickness bridge.

Subsequent improvement in fabrication techniques[2,3], which reduced the size of the microbridges by almost an order of magnitude, showed that at least near T_c the properties of microbridges were in qualitative and to some extent quantitative agreement with ideal Josephson behaviour.

It was not until 1973 that Skocpol, Beasley and Tinkham[4] showed that Joule dissipation played a major role in determining the properties of all constriction weak links. In particular, this idea explained the pronounced hysteresis observed in the I-V characteristics of planar microbridges and the fact that the ac Josephson effect was only observed up to voltages of the order of 0.5 mV, corresponding to frequencies of 500 GHz. This voltage limit is significantly lower than that of superconducting point contacts, in which ac effects are observed up to voltages of the order of 15 mV. It was suggested that the superiority of the point contact geometry arises from its three dimensionality, which more efficiently removes the heat generated in the contact. Furthermore, point contacts have higher resistances, which implies lower dissipation at the same voltage since the dissipation scales as V^2/R_N. Thus, it was recognized that a reduced-heating or variable-thickness geometry, in which a thin bridge is connected to much thicker banks, would significantly reduce heating effects due to the improved cooling provided by the thicker banks. At the same time, Likharev[5] and coworkers in the Soviet Union considered variable-thickness

microbridges, not only because of their better cooling, but also because the lower current density in the banks should restrict nonlinearities to the bridge region, so that the microbridges should behave more like ideal Josephson junctions.

At that point we began to try to make lead and tin variable-thickness superconducting microbridges. The advantage of a thin film geometry for high frequency applications is that it is a permanent structure which is compatible with thin-film techniques for the fabrication of antennas, arrays, and other complex systems. It was our goal to fabricate variable-thickness bridges in which heating effects would be significantly reduced and, if possible, in which the ac Josephson effect could be observed at far-infrared frequencies.

Once a reliable fabrication technique was developed, as discussed in Chapter Two, it was found that the properties of our microbridges were remarkably different from those of two-dimensional microbridges. The most significant difference was the observation of the ac effect up to voltages a factor of four higher than had previously been observed in any thin-film weak link. This implied the presence of ac supercurrents flowing through the weak links at far-infrared frequencies and suggested the possibility of using our variable-thickness microbridges for the detection of far-infrared radiation.

In Figure 1.2, the I-V characteristics of two of our tin microbridges are shown. The bridge in Fig. 1.2 (a) corresponds to a well-cooled bridge in which the ac Josephson effect was observed up to 2.3 mV. Note that at the lowest temperatures a multivalued curve develops. (The segments of negative slope are the result of averaging over circuit-controlled relaxation oscillations[4]). Furthermore, very sharp "bumps" corresponding to the gap and subharmonic gap structures, discussed in Chapter Five, are observed. While the performance of this bridge is already a considerable improvement over planar microbridges it should be contrasted with the I-V characteristics shown in Fig. 1.2 (b). This corresponds to a bridge of resistance similar to the previous one, but which is better cooled because of much thicker banks. In this case, the I-V characteristics are very smooth, with no multivaluedness even at the lowest temperatures. When microwave radiation is applied to this bridge, ac Josephson steps are observed up to 3.7 mV. That this improved behaviour is due to better cooling is confirmed by the presence of the gap structure at much higher voltages corresponding to lower temperatures than in the first bridge. As discussed in Chapter Five, we have used this gap structure as a local thermometer of the average temperature rise in the bridge region in order to quantitatively demonstrate the connection between high frequency performance, hysteresis, and heating.

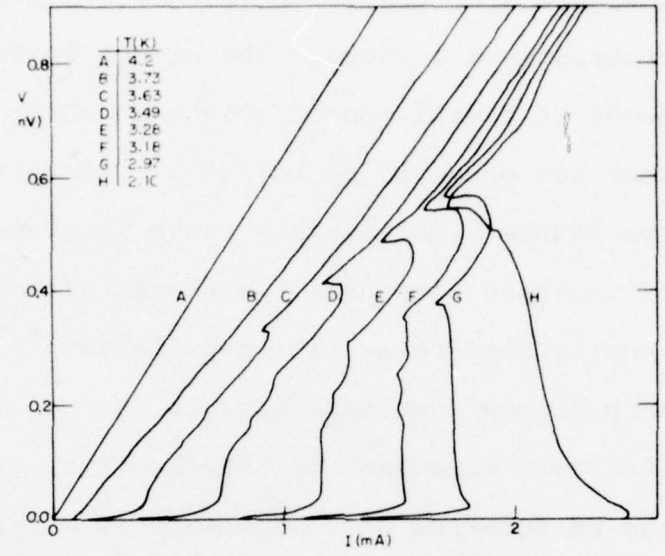

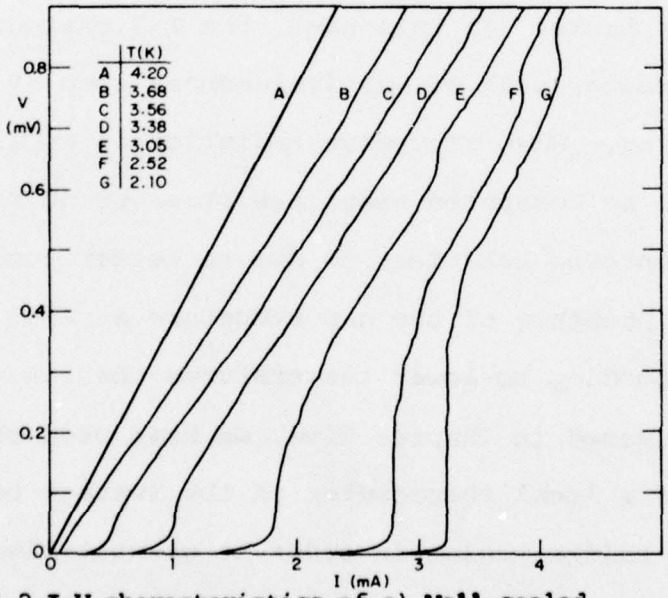

Fig. 1.2 I-V characteristics of a) well-cooled microbridge (#9). b) very well-cooled microbridge (#11).

Because of the novel nature of our microbridges, we have attempted to characterize their overall properties. In the course of our work, we accumulated a large amount of data on the critical currents of bridges with a wide distribution of resistances. It was found that our results differed quantitatively from theory both near T_c and at low temperatures, as discussed in Section 3.1. On the other hand, the temperature dependence of the critical current was found to be Josephson-like (linear) for both tin and lead bridges near T_c, despite their differences in coherence length.

Due to the reduced hysteresis, some of the features of the I-V characteristics became very pronounced and could be followed over a much wider temperature range than had previously been possible. We became very interested in the foot-like features at low voltages which can be seen in the I-V characteristics of both bridges shown in Fig. 1.2. Note that in the case of the better-cooled bridge this feature can be observed all the way down to 2.1 K, because of the absence of hysteresis. As discussed in Chapter Four, these features are found to be consistent with a voltage-dependent enhancement of the supercurrent induced by the disequilibrium of the quasiparticles during the Josephson cycle. Comparison of our experimental results[6] with the predictions of the theories of Golub[7] and of Aslamasov and Larkin[8] yield good agreement with many aspects of our data, although some

questions remain open.

Earlier indications were that the voltage limit for the ac Josephson effect scaled with the superconducting energy gap $2\Delta/e$, which favors high T_c materials.[4] However, our experimental results on lead microbridges differed little from those on tin, suggesting that a more careful analysis of the three-dimensional problem was required. This, together with our experimental observations indicating that at high dissipation levels the basic Bessel-function-like periodicity of the amplitudes of the ac steps remained, led us to a simple heating model for three dimensional geometries, discussed in Chapter Five. This model predicts that the critical current decreases exponentially with power as e^{-P/P_o} where P is the power dissipated in the junction and P_o depends on temperature, material parameters, and junction geometry. From this model it is possible to infer the best possible materials and geometries for good high-frequency performance. The predictions of the model are in very good agreement with our results in variable-thickness microbridges as well as with other results found in the literature for both variable-thickness microbridges and point contacts.

The observation of ac steps at voltages corresponding to far-infrared frequencies encouraged us to attempt the observation of an ac Josephson step induced by a far-infrared laser. This unsuccessful effort is described in Section 6.1. The main difficulty was our inability to couple enough far-

infrared radiation to our low impedance microbridges ($R_N < 1\Omega$). While a very small decrease of the critical current was observed, it was not possible to determine whether this was due to heating or to the Josephson effect. While it might be possible to increase the impedance of the microbridges by proper choice of materials and design, another possibility is to use arrays of microbridges in series. In Section 6.2, we include some of our experimental results with series pairs of microbridges. While no coupling effects were observed at high voltages, some interesting effects were observed at low voltages, indicating that further study of these systems is needed.

The organization of this report is as follows: In Chapter Two the experimental techniques used in the fabrication and measurement of the properties of our bridges are presented. Chapter Three discusses the general characteristics of our microbridges, such as critical currents and the Wyatt-Dayem effect. Chapter Four deals with the theory and experimental results on the nonequilibrium-enhanced supercurrents at low voltages. In Chapter Five the heating model is described and comparison is made to our experimental results both at high and low voltages. Chapter Six contains some discussion of our exploratory experiments with far-infrared radiation as well as with arrays of microbridges.

CHAPTER TWO

EXPERIMENTAL TECHNIQUES

2.1 Sample Preparation

Since our primary goal was the study of the physical properties of variable-thickness microbridges, we decided upon a simple and quick microfabrication technique which allowed us to fabricate a complete sample using only diamond knives and microneedles. While this technique has drawbacks in terms of reproducibility and size control, once a film was evaporated a good quality sample could be made in less than half an hour. Furthermore, this technique allowed us to make very thick banks without the limitations of more involved techniques using resists, in which the maximum thickness is limited by the resist thickness.

Because of the stresses associated with cutting the films with a diamond knife, it was found essential that the films adhere well to the substrate. To achieve this, we use a technique similar to that described by Chiao et al[11]. We first clean the sapphire substrates ultrasonically in successive solutions of Sparkleen detergent, distilled water and isopropyl alcohol. The substrates are then wiped clean with Kodak lens paper and are placed on a hot plate where small indium patches are attached to them. Two three-inch solder-coated Nb_3Sn tapes are then attached to the indium

patches in order to provide electrical contact to the films which will be evaporated on top of the substrates. The substrates are then placed on a copper plate which is screwed to a copper block in the evaporator. This copper block can be cooled to liquid nitrogen temperatures.

Once in the evaporator, the substrates are cleaned in an oxygen glow discharge for periods of half an hour to an hour. The glow discharge is produced by a pure aluminum wire at a voltage of 600 volts and currents of 25-30 mA corresponding to pressures of 0.03 Torr. Care is taken that there is no direct line of sight between the aluminum wire and the substrates as this yields buckled films, presumably because of the sputtering of aluminum atoms onto the substrates. After this step, a thin tin or lead undercoat (50-100 Å thick depending on the ultimate thickness of the film to be evaporated) is evaporated and allowed to oxidize in the glow discharge for periods of two to four hours. After the samples are cooled to liquid nitrogen temperatures, a thick 1-3 μm film is evaporated at pressures of 2×10^{-6} Torr and rates of 90-200 Å/sec. The thickness of the film is monitored with a Sloan 200 deposition thickness monitor.

Using the above technique we obtain very well adhered films which withstand the "tape test", in which a piece of Scotch-Brand tape is attached to the film and pulled without any of the film coming off the substrate. The good adhesion also offers two additional desirable features. First, the

leads can be attached to the films after the evaporation. This is very convenient if a large number of samples are fabricated or if a lead accidentally comes off the substrate after the microbridge has been fabricated. Second, the good adhesion significantly reduces the burnout rate of our samples. In those cases in which a bridge with good adhesion was accidentally destroyed, the burnout region was restricted to the bridge region only. In the case of a film with poor adhesion this burnout region was found to spread into the banks for several μm.

In attempting to reduce the burnout rate of our bridges, we also fabricated our microbridges on germanium substrates[12] to provide a high temperature short to the bridge. While this was found to be helpful, the germanium substrates were found to be inconvenient to handle as they were brittle and had a tendency to break along any cut made on the substrate with a diamond knife. Another disadvantage was that while our sapphire substrates could be reused repeatedly, the germanium substrates could not. Cleaning the films off the germanium substrates produced an oxide layer on the surface of the substrate and thus there was no electrical contact between the substrate and the film evaporated on it.

Two types of diamond knives, both manufactured by the J. Robert Moore Co., were used in cutting our films. The first type was a sharp point knife formed by the intersection of three cleaved planes which was used for making small

grooves in the substrates. The second type was a long (2 mm.) straight-edge knife which was used for the removal of large areas of film and in the fabrication of the microbridges.

The diamond knives are mounted at the end of a rotatable rod attached to a micromanipulator. This micromanipulator provides coarse and fine control in the vertical direction as well as angular control. Thus the edge of the knife can be aligned parallel to the surface of the film to be cut. The substrates are placed on a differential screw translation stage which provides translational motion in the X-Y directions. The knife and the area to be cut can be viewed through a Bausch and Lomb StereoZoom microscope with a maximum power of 140X.

The grooves on the sapphire substrates are made by sliding the substrates beneath the single point knife while periodically adjusting the height of the knife to ensure that the smallest possible groove is made. In this manner we obtained grooves typically 0.2-0.3 μm wide and 0.1-0.3 μm deep. Typically 5-10 of these grooves were made on each substrate so that a different groove could be used each time a substrate was reused. This was done to avoid possible shorts caused by scratches on the sapphire substrate over areas which were previously used.

After the films are evaporated onto the grooved substrates, the flat long knife is used to remove the film from several small rectangular regions on each side of the groove as shown

in Fig. 2.1 (a) and (b). Then the flat knife is aligned parallel to the film surface by rotating the knife edge until it is parallel to its own reflection on the surface of the shiny film. The long flat edge is then gently pressed against the film, leaving a small thin bridge in the groove, but separating the thick banks attached to it as shown in Fig. 2.1 (c) and in the SEM pictures in Fig. 2.2. The essential difference from previous "double-scratch" techniques is that the whole film is cut simultaneously by a single edge rather than by a point dragged through the film. This has the advantage that a simple manual scheme can be used since the sapphire substrates stop the diamond knife from penetrating through the bridge. (The knife actually penetrates a little in order to separate the banks but this is usually not enough to cut completely through the bridge in the groove.) Using this fabrication technique, an experienced operator can obtain an 80-90% yield; the main problem is not in obtaining a microbridge, but in aligning the knife edge so that the banks are completely separated in regions far from the bridge.

After 15-30 bridges are made along a single groove, they are inspected with an optical microscope at 400X and the best bridge is selected for testing. Best is defined as the optimum combination of a small bridge, located where the groove is small, with the banks completely separated. A Circon microneedle is then used to isolate the selected

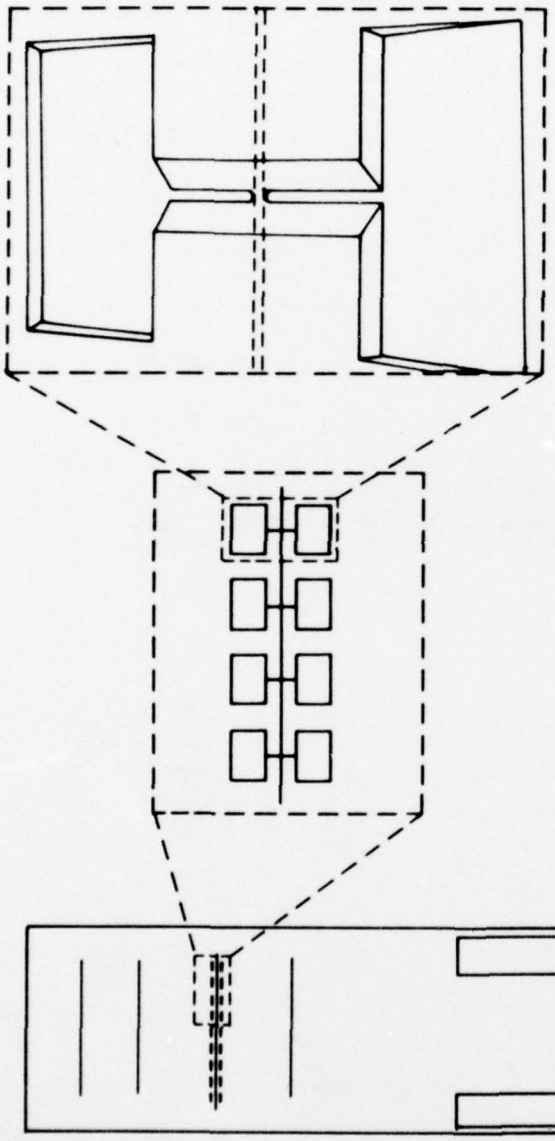

Fig. 2.1 Schematic of bridge fabrication.

Figure 2.2. Scanning electron micrographs of a bridge.
Top: Overview of bridge and banks.
Bottom: Close-up of the microbridge.

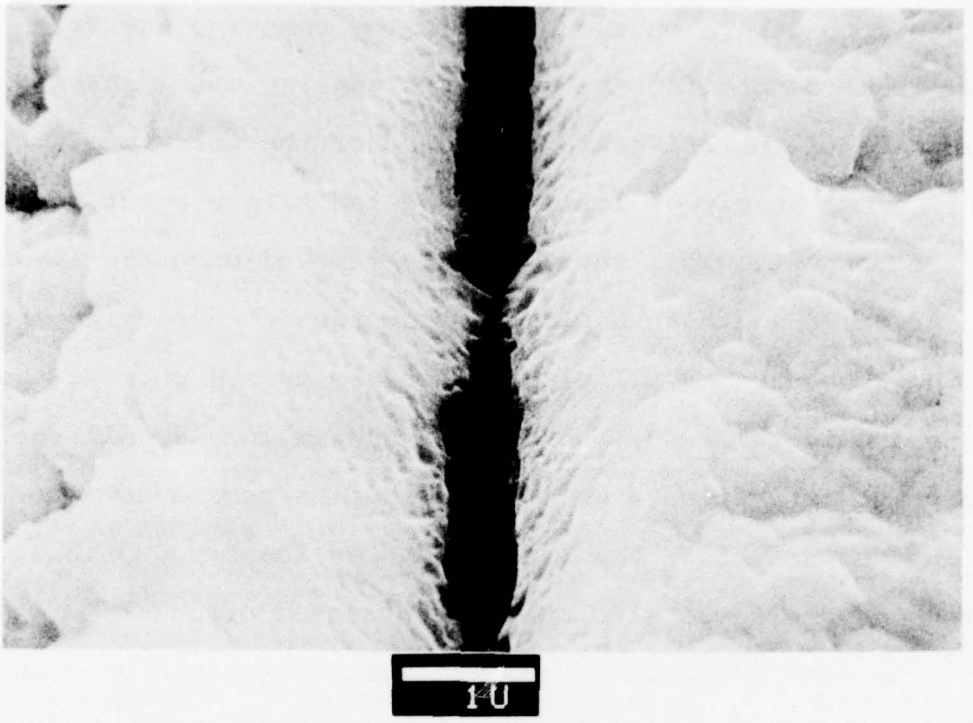
1U

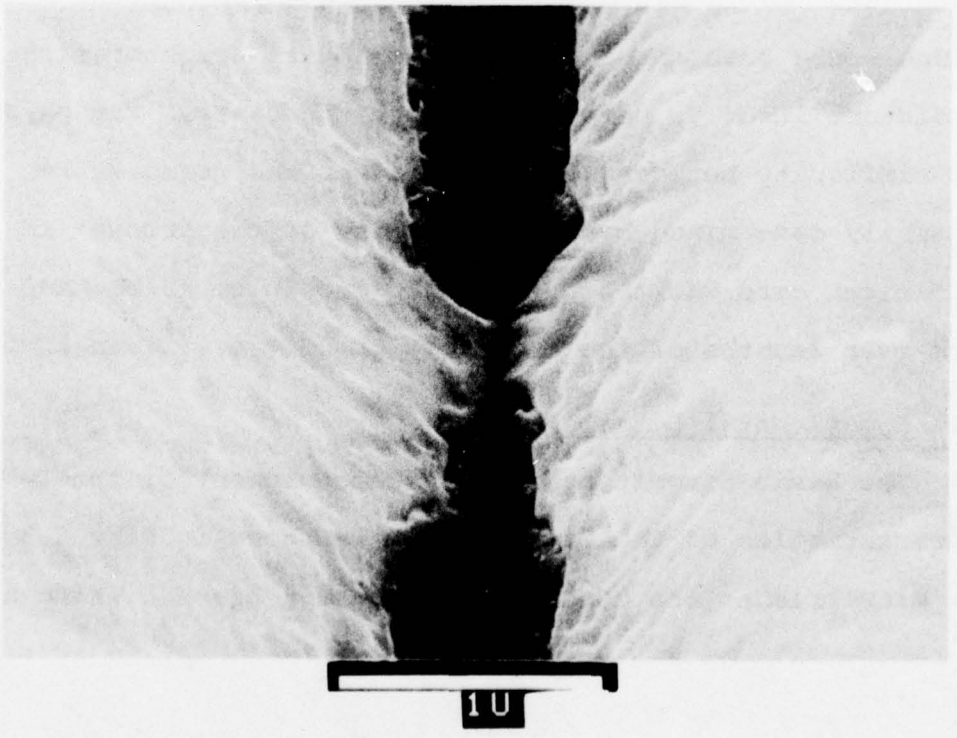
1U

bridge from others on the substrate by removing the film from lines connecting the small rectangular openings on each side of the bridge to the edges of the substrate. A small short is always left near the leads to prevent accidental burnout. This short is only removed once the leads are soldered (with an unplugged and grounded soldering iron) to the cryostat and all electronics are turned on. If this procedure is followed, burnout is rare as long as all the equipment is left on. Once the bridge is cooled down to helium temperatures, the bridge becomes less susceptible to burnout even if the electronics are turned off.

The same techniques outlined above have been used in the fabrication of arrays of microbridges in series. In this case we found it necessary to keep the thickness of the banks less than 1 μm or the fabrication of the second microbridge would push enough material onto its neighbor either to distort it or to completely short the banks. The physical similarity between adjacent bridges was found to be primarily determined by the uniformity of the groove; if sufficient care was taken, a single groove could be made uniform over lengths of the order of 100-200 μm.

2.2 Experimental Details

The basic circuit used in the measurement of the I-V characteristics of the microbridges is shown in Fig. 2.3 (a). The microbridges are essentially "voltage biased" using a

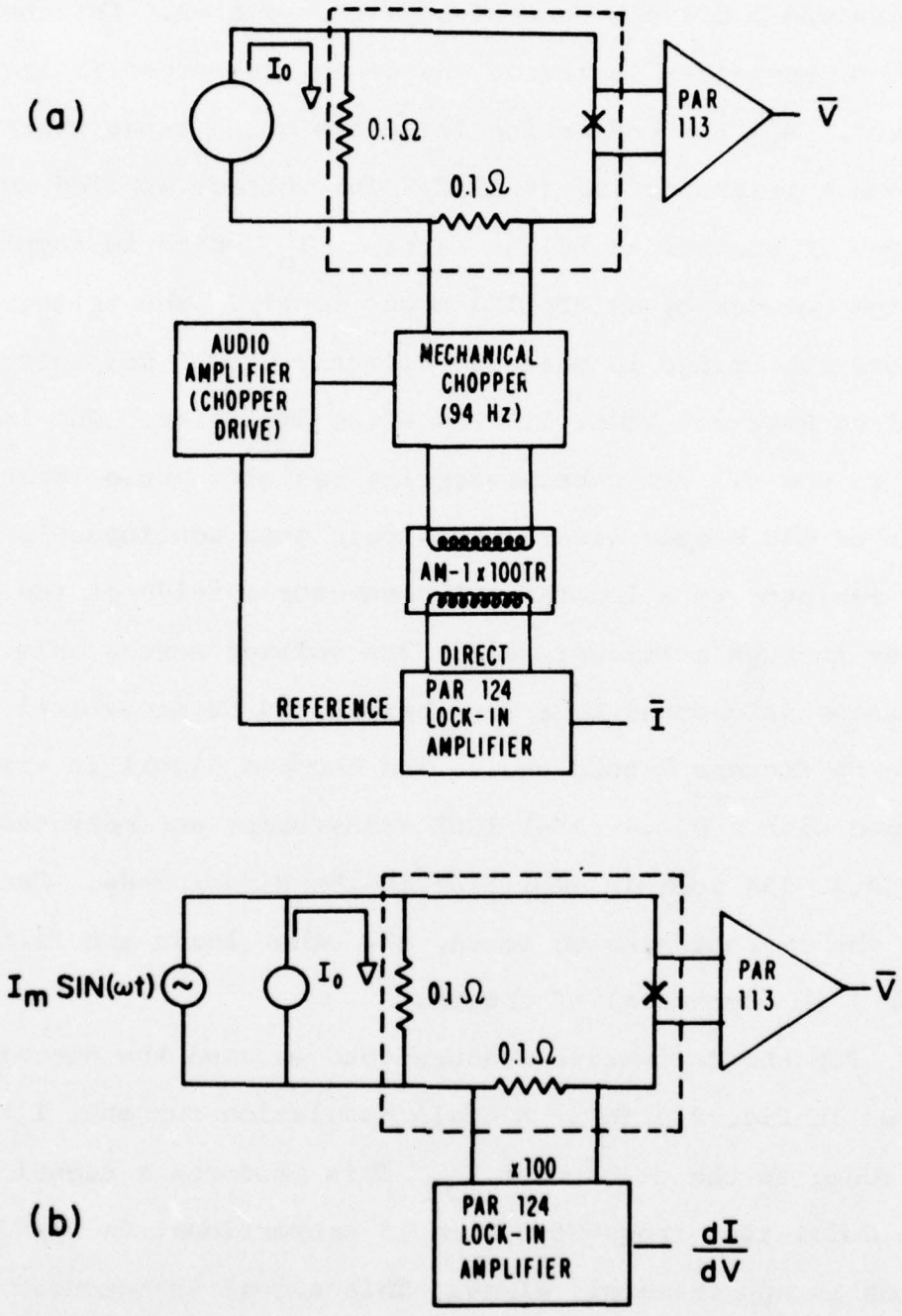

Fig. 2.3 Circuits used in measuring a) I-V characteristics b) dI/dV versus V.

0.1 ohm resistor shunting the series combination of the bridge and a 0.1 ohm current-sensing resistor. This network of resistors is inside the dewar, submerged in liquid helium. All the connecting leads are Nb_3Sn tapes which become superconducting at 17 K. The voltage applied to the bridge is controlled by the current, I_o, which is supplied to the network by an HP61774 power supply. The voltage across the bridge is measured directly with a Princeton Applied Research Model 113 Low Noise Amplifier. The leads across the 0.1 ohm current-sensing resistor are a twisted pair of #38 copper wires. This pair goes continuously from the resistor to a low-thermal connector outside of the dewar through a Stycast seal. The voltage across this resistor is chopped by a low-thermal, 94 Hz mechanical chopper made by Stevens Arnold Inc. The chopped signal is transformed with a P.A.R. AM-1 100X transformer and measured with a P.A.R. 124 lock-in amplifier in the direct mode. Except for the current-sensing leads, all other leads are filtered with 1 mH commercial rf chokes.

For the derivative measurements we used the circuit shown in Fig. 2.3 (b). A small modulation current, $I_m \sin(\omega t)$, is added to the dc current I_o. This produces a signal at the modulation frequency which is proportional to $\Delta I/\Delta I_o$ which is approximately dI/dV. This signal is measured with a P.A.R. 124 lock-in amplifier in the X100 transformer mode.

While we have described our measuring circuit as a

voltage-biased circuit, this is not strictly true. In our earlier experiments, the resistance of our biasing resistors was 0.01 ohm. This was sufficiently below the impedance of our microbridges to make the measuring system very close to a voltage-biased one, once the critical current was exceeded. Later, in order to improve the sensitivity of the system, the resistors were replaced by 0.1 ohm resistors which is of the order of the typical impedance of our microbridges. Thus, the biasing is not strictly voltage biased and is dependent on the impedance of each particular bridge.

Most of our experiments on tin microbridges were performed with the samples directly exposed to the helium bath. The samples are mounted on a copper block and their temperature is monitored by both a calibrated Ge thermometer and the vapor pressure of the helium bath. The bridges are mounted so that they stick into the narrow side of an X-band waveguide a distance $\lambda_g/4$ from its closed end. The orientation of the bridges is such that they are parallel to the E field, but little change was observed if the orientation was perpendicular to the E-field. While this coupling arrangement is quite crude it allowed us to explore the ac response of our samples in detail as long as enough microwave power was available. For some of our lead microbridge experiments the tip of the cryostat was surrounded by a brass vacuum can and the temperature regulated electronically. The entire dewar was surrounded by Mu-metal shields to reduce the earth's

magnetic field. The experiments were performed in a Ray-Proof RF shielded room, but little change was noticed when the door to the room was not closed.

The far-infrared experiments were performed in an unshielded dewar with an optical window in front of the microbridge. The cryostat used in these experiments allowed the rotation of the sample for improved coupling to the far-infrared radiation.

Three separate microwave sources were used in the course of our experiments. Initially we used a Laboratory for Electronics Ultrastable X-band oscillator with a maximum output power of the order of 20 mW. Sometimes, depending on the sample, this was not sufficient to drive the microbridge completely normal, so we changed to a fixed frequency (10.525 GHz) Plessey Semiconductor Gunn diode oscillator with a maximum output power of 300 mW. In the final stages of our work we used a Varian Associates 32 GHz Gunn diode with an output power of 60 mW. The 32 GHz radiation was brought to the sample through the X-band waveguide so that the exact mode at the sample was not known.

CHAPTER THREE

STATIC PROPERTIES OF VARIABLE-THICKNESS SUPERCONDUCTING MICROBRIDGES: CRITICAL CURRENTS AND $I_{co}R_N$ PRODUCTS

While the original theoretical predictions of B. D. Josephson[13] were made for an oxide barrier separating two superconducting films, experimental investigations have shown that, in some general sense, Josephson-like behavior can be observed in any system in which two superconductors are weakly connected. This weakness can be introduced by geometrically constricting a superconducting film, as in the microbridges of interest here, by overlaying a superconducting film with a normal metal,[14] by optical, phonon or quasiparticle injection,[15] by ion implantation[16] or even by locally reducing the order parameter with a small magnetic field.[17] While all of these systems exhibit some form of Josephson behaviour, their properties can differ markedly from ideal behaviour either because they are large compared to the coherence length or because they do not have three-dimensional cooling geometries as do variable-thickness microbridges.

In this chapter, we characterize and discuss the basic properties of our variable-thickness microbridges in the context of a simple Ginzburg-Landau model of Josephson behaviour applicable to short weak links. The observed critical currents near T_c are compared to the predictions of

this model, and it is found, for both low and high resistance microbridges, that the temperature dependence of the critical currents agree qualitatively but not quantitatively with the predictions of this model. At low temperatures the critical currents are found to be comparable to those expected from microscopic theory. Finally, some aspects of the enhancement of the critical current in the presence of microwaves are discussed.

3.1 The Critical Current

3.1.1 Regime Close to T_c

In the zero voltage state one deals with the equilibrium, time-independent state and, at least near T_c, it is possible to use the two-fluid picture of the Ginzburg-Landau theory. The superconductor is then represented by a complex order parameter $\Psi(\vec{r}) = |\Psi_o|e^{i\varphi}$, where φ is a phase factor which is a function of both position and time. The free energy density of a superconducting system is then represented by a power series expansion in $|\Psi|^2$ and the gradient $|\nabla\Psi|^2$. The problem is then reduced to minimizing the free energy in a manner consistent with the boundary conditions of the system under consideration. The first application of this concept to the properties of small weak links was made by Aslamazov and Larkin.[18] They took advantage of the fact that if the weak link is small compared to the temperature-dependent

coherence length $\xi(T)$, then the gradient term will dominate the free energy density inside the weak link. This implies that Ψ satisfies Laplace's equation $\nabla^2\Psi = 0$ with appropriate boundary conditions. In the case of the variable-thickness or point-contact geometries, the boundary conditions are that the order parameter equals that of the bulk superconductor at either side of the weak link, $\Psi_o e^{i\varphi_1}$ and $\Psi_o e^{i\varphi_2}$ where $\varphi_{1,2}$ are the phases at each side of the weak link. Aslamazov and Larkin considered a particular solution to Laplace's equation $f(\vec{r})$ which tends asymptotically to unity on one side of the weak link and towards zero on the other. The order parameter is then given by

$$\Psi(\vec{r}) = \Psi_o \left\{ f(\vec{r})\, e^{i\varphi_1} + \left[1 - f(\vec{r})\right] e^{i\varphi_2} \right\} \qquad (3.1)$$

where Ψ_o is the equilibrium value of the order parameter deep in the superconductors and the phases $\varphi_{1,2}$ are independent of coordinates. The supercurrent density is given by

$$\vec{J}_s = \frac{e^* \hbar}{2m^* i} (\Psi^* \vec{\nabla} \Psi - \Psi \vec{\nabla} \Psi^*) = \frac{e^* \hbar}{m^*} |\Psi_o|^2 \vec{\nabla} f \sin \varphi_o \quad (3.2)$$

where φ_o is the total phase difference across the weak link, and $\vec{\nabla} f$ is averaged over the cross-section at the middle of the bridge. This equation is equivalent to the Josephson[18] current-phase relation derived from microscopic theory for a superconductor-oxide-superconductor tunneling structure with

$$I_{co} = \frac{A\, e^* \hbar}{m^*} |\Psi_o|^2 \nabla f \quad (3.3)$$

where I_{co} is the critical current of the weak link and A is the cross-sectional area of the weak link.

Thus for sufficiently small weak links one expects an ideal sinusoidal current-phase relation. Such behaviour has been observed in niobium point contacts, small two-dimensional microbridges and variable-thickness microbridges.[19,20,21] While we have neglected linear terms in the free energy density under the assumption that the length of the link L is smaller than the temperature-dependent coherence lenght $\xi(T)$, more detailed calculations by Likharev and Yakobson[22] have shown that the current-phase relation will be essentially sinusoidal up to a critical length

$L_c \sim 3.5\ \xi(T)$. As the length L of the link becomes larger than $\xi(T)$, the current-phase relation becomes skewed until it becomes reentrant; and eventually the solution to the Ginzburg-Landau equation for the order parameter corresponds to that of a long bulk filament. One of the advantages of the variable-thickness geometry becomes apparent from this, because the thick banks have a much smaller current density than the bridge, restricting all nonlinearities to the bridge region. Thus, if one has two bridges with a well defined length L, one with banks with the same thickness as the bridge and another with thicker banks, the variable-thickness bridge will behave more like an ideal Josephson element than will the two-dimensional bridge. Furthermore, the ideal behaviour will be preserved over a wider temperature range as $\xi(T)$ becomes smaller.

In order to calculate certain properties of our bridges such as the critical current or their approximate size, an appropriate geometry should be considered. Aslamazov-Larkin consider a hyperbolic neck of radius a and apex angle θ as shown in Fig. 3.1 (a). As long as the mean free path $\ell \ll a$, the normal resistance of the link is given by

$$R_n = \frac{\rho}{2a}\ \mathrm{ctn}(\theta/2) \qquad (3.4)$$

where ρ is the normal state resistivity. It is convenient for calculations to replace this geometry by the more artificial one shown in Fig. 3.1 (b), defined by two intersecting

Figure 3.1. Schematic of a) hyperbolic neck geometry;
b) collinear cone geometry

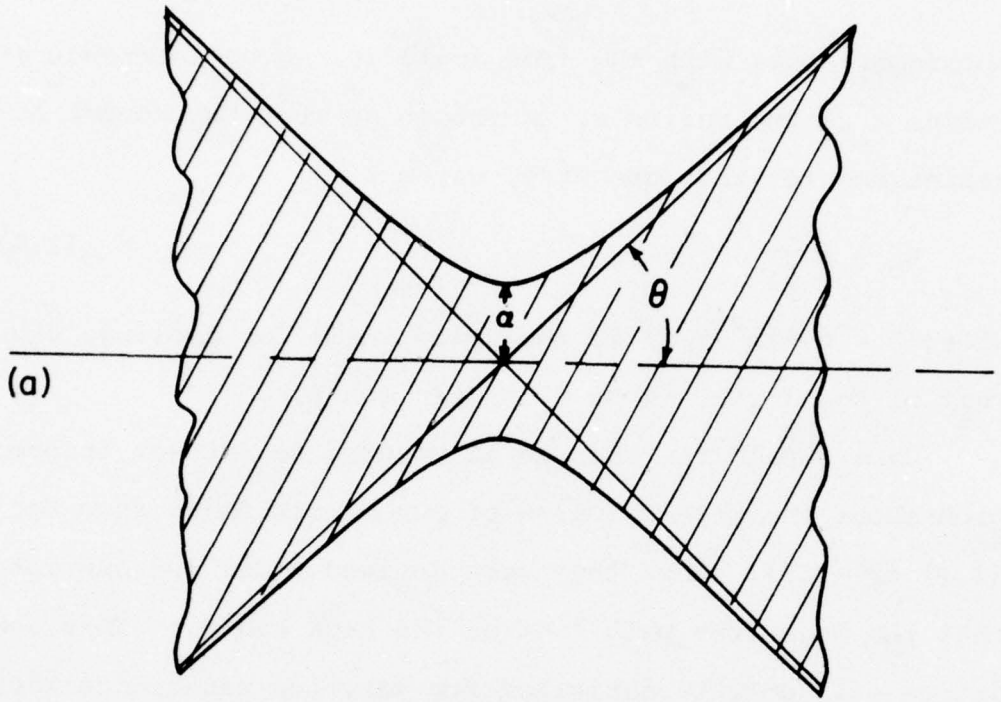
(a)
α
θ

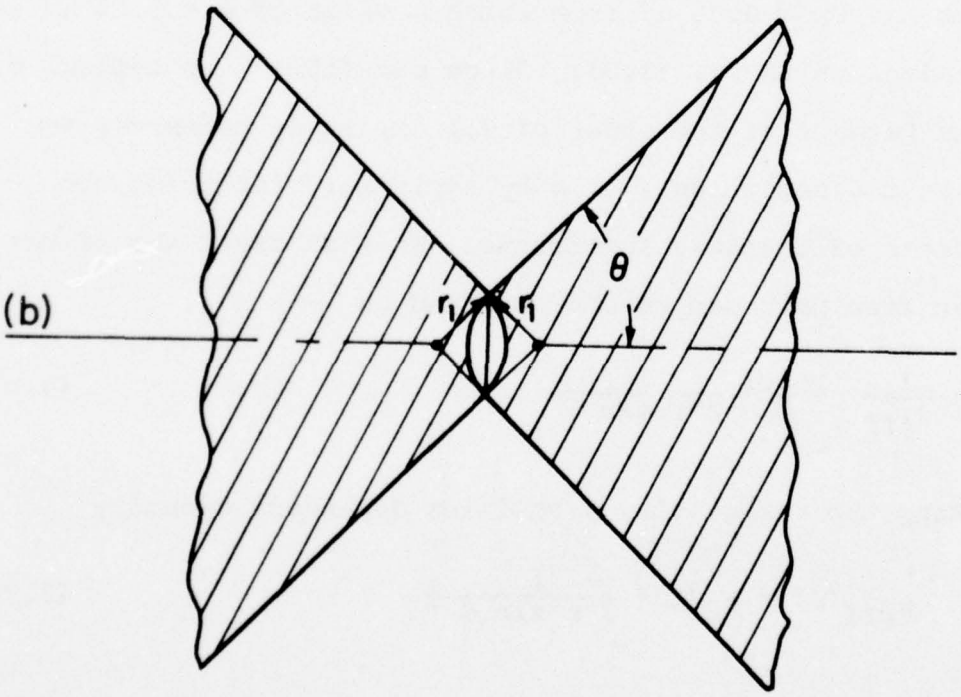
(b)
r_1
r_1
θ

collinear cones with the same angle 2θ, which intersect at a radius r_1. The radius r_1 is chosen so that the normal state resistance for this geometry, given by

$$R_n = \frac{2\rho}{\Omega\, r_1} \tag{3.5}$$

where $\Omega = 4\pi\sin^2(\theta/2)$ is the solid angle for cooling, equals that of Eq. (3.4). Then $r_1 = 2a/\pi \sin\theta$.

Care should be taken in attempting to extract information about the physical size of our microbridges from Eq. (3.4) or (3.5), since they were derived under the assumption that the mean free path $\ell \ll a$, the neck radius. This condition will only be satisfied for very low resistance microbridges. The lowest resistance microbridge studied in this work had $R_N = 0.06\ \Omega$; from which a value of $a = 0.14\ \mu m$ was obtained using Eq. (3.5). Since our films have typical mean free paths ℓ of the order of $0.1\ \mu m$, it is necessary to relax the condition $\ell \ll a$ by explicitly including the effects of boundary scattering. In that case, the effective mean free path can be approximated as

$$\frac{1}{\ell_{eff}} = \frac{1}{\ell} + \frac{1}{2\, r\, \sin\theta} \tag{3.6}$$

making the resistivity a position dependent quantity

$$\rho_{eff}(r) = \rho_o\left(1 + \frac{\ell}{2\, r\, \sin\theta}\right) \tag{3.7}$$

The normal state resistance of the weak link will then be given by

$$R_N = \frac{2\rho_o}{\pi r_1}\left(1 + \frac{\pi \ell}{8a}\right) \qquad (3.8)$$

Using Eq. (3.8), the calculation of the neck radius a for the example of $R_N = 0.06$ ohm yields $a = 0.18\ \mu m$. Thus, even for our lowest resistance microbridges, the corrections due to boundary scattering are significant. These corrections will be quite large for our high resistance microbridges or high resistance point contacts. The collinear cone geometry should be a very good approximation to the geometry of our variable-thickness microbridge as evidenced by the SEM pictures shown in Chapter Two. In some cases discussed in Chapter Five, it might be necessary to take into account a small finite length of the bridge neck between the cones, but this can be neglected in calculating resistances or critical currents.

In Table 3.1, some of the basic properties of our tin microbridges are presented. (A more complete table of all the properties of our tin and lead microbridges is included in Appendix A.) The bridges are arranged in Table 3.1 in order of increasing resistance. From SEM pictures of the microbridges it was determined that they do not vary significantly in length or width at the narrowest point of the neck. Unfortunately, the thickness of the bridge depends on the groove depth which can vary with pressure or the shape of the particular diamond point used.

Table 3.1

Characteristic Properties of Some Tin

Variable-Thickness Microbridges

#	Normal State Resistance R_N (Ohms)	$R_N \frac{dI_{co}}{dT}$ (mV/K)	Exponent of I_{co} $I_{co} \propto (T-T_c)^{\alpha}$	$I_{co}R_N$(2.1K) (mV)
19	0.06	0.76	0.94	0.88
21	0.07	0.77	1.25	1.10
13	0.09	0.68	0.87	1.16
14	0.20	1.16	1.00	1.38
4	0.24	1.37	1.07	2.71
11	0.33	0.56	0.97	1.32
9	0.36	0.56	1.07	0.90
16	0.44	0.80	0.96	1.19
8	0.44	0.75	1.09	3.30
7	0.43	1.02	1.03	1.63
10	0.85	1.27	0.87	1.62
12	1.14	1.05	1.05	1.49
17	1.25	0.69	-	1.25
20	1.76	0.42	0.91	1.44

The range of resistances in Table 3.1 is representative of the bridges tested, which of course were influenced by the author's procedure for optically selecting bridges as well as by the survival rates of the bridges selected. In the earlier stages of this work, low resistance bridges were used because of their larger survival rate. As the burnout problem was brought under control, the smallest possible bridge on each substrate was tested. All of the films from which the bridges were made had mean free paths of order 0.1-0.14 μm, so that differences in resistance from bridge to bridge are mostly due to size. Table 3.1 illustrates the difficulty in making microbridges of clean tin with resistances larger than 1 ohm, as we usually discarded those bridges with low resistances at room temperature and these were already a selection of the smallest possible microbridges.

In some cases the bridges were longer than 0.5 μm. This occurred when the bank on the side of the bridge was lifted off the substrate by the diamond knife leaving some tin in the groove under the lifted film and thus creating a longer microbridge. We believe this causes the high resistance observed in some bridges such as #10, 12 and 20. Thus, of the bridges with no anomalous properties, bridge #17 has the highest resistance; using Eq. (3.8) this corresponds to a neck radius of 0.02 μm.

Using the results derived for the collinear cone geometry

it is then possible to calculate the magnitude and temperature dependence of the critical current Eq. (3.3). If one assumes the electrical potential satisfies Laplace's equation then $V(r) = V_1 + Vf(r)$ where V is the total potential drop, $V_2 - V_1$. Then since $I = \pi a^2 \sigma V \nabla f = V/R_N$, $R_N = 1/(\pi a^2 \sigma \nabla f)$ and (3.3) reduces to

$$I_{co} R_N = \frac{e^* \hbar}{m^*} \frac{|\Psi_o|^2}{\sigma} \tag{3.9}$$

In the dirty limit ($\ell \ll \xi_o$) this reduces to

$$I_{co} R_N = \frac{\pi \Delta^2 (T)}{4eT_c} = (0.635 \text{ mV/K}) \times (T_c - T) \tag{3.10}$$

where $\Delta(T)$ is the energy gap and $\Delta(0) = 1.76\ T_c$, where temperature is measured in energy units. Eq. (3.10) agrees near T_c with the expression for the critical current obtained for tunnel junctions by Ambegaokar and Baratoff:[23]

$$I_{co} R_N = \frac{\pi \Delta(T)}{2e} \tanh[\Delta(T)/2T] \tag{3.11}$$

In column 2 of Table 3.1 the experimental results for $R_N dI_{co}/dT$ near T_c are shown. Note that these values are usually higher than would be expected from Eq. (3.10) and may exceed the expected value by as much as a factor of four. This is a common discrepancy found in two-dimensional tin and indium microbridges[24] as well as in variable-thickness microbridges.[25] The origin of this discrepancy is

not presently understood. It is apparently not due simply to size effect corrections to the resistivity, since these would be most important in high resistance weak links. It is also not due to uncertainty in determining the appropriate experimental resistance values, because the theoretical R_N is the full normal resistance of the entire weak link, surely an upper bound.

The more detailed temperature dependence of the critical current for two of our tin microbridges is shown in Fig. 3.2. The values of $(dI_{co}/dT)R_N$ shown in Table 3.1 are determined from the linear region between $T/T_c = 0.8\text{-}0.98$. The value of the exponent obtained from a least squares fit over this temperature range is shown in column 3 of Table 3.1. These values are in very good agreement with what is expected for Josephson behaviour near T_c. For temperatures below $T/T_c \sim 0.8$ the critical current begins to grow less rapidly as predicted by Eq. (3.11)

Near T_c ($T/T_c \gtrsim 0.98$) the situation is quite different. Two different types of behaviour can be observed depending on the sample, as shown in the inset in Fig. 3.2. The more common behaviour is that of the lower curve which has a small nonlinear tail very close to T_c, where T_c is identified as that temperature at which a supercurrent is first observed. We believe this behaviour is caused by the bridge region having an intrinsic transition temperature T_{ci} below that of the bank material T_{cb}. This is supported by careful

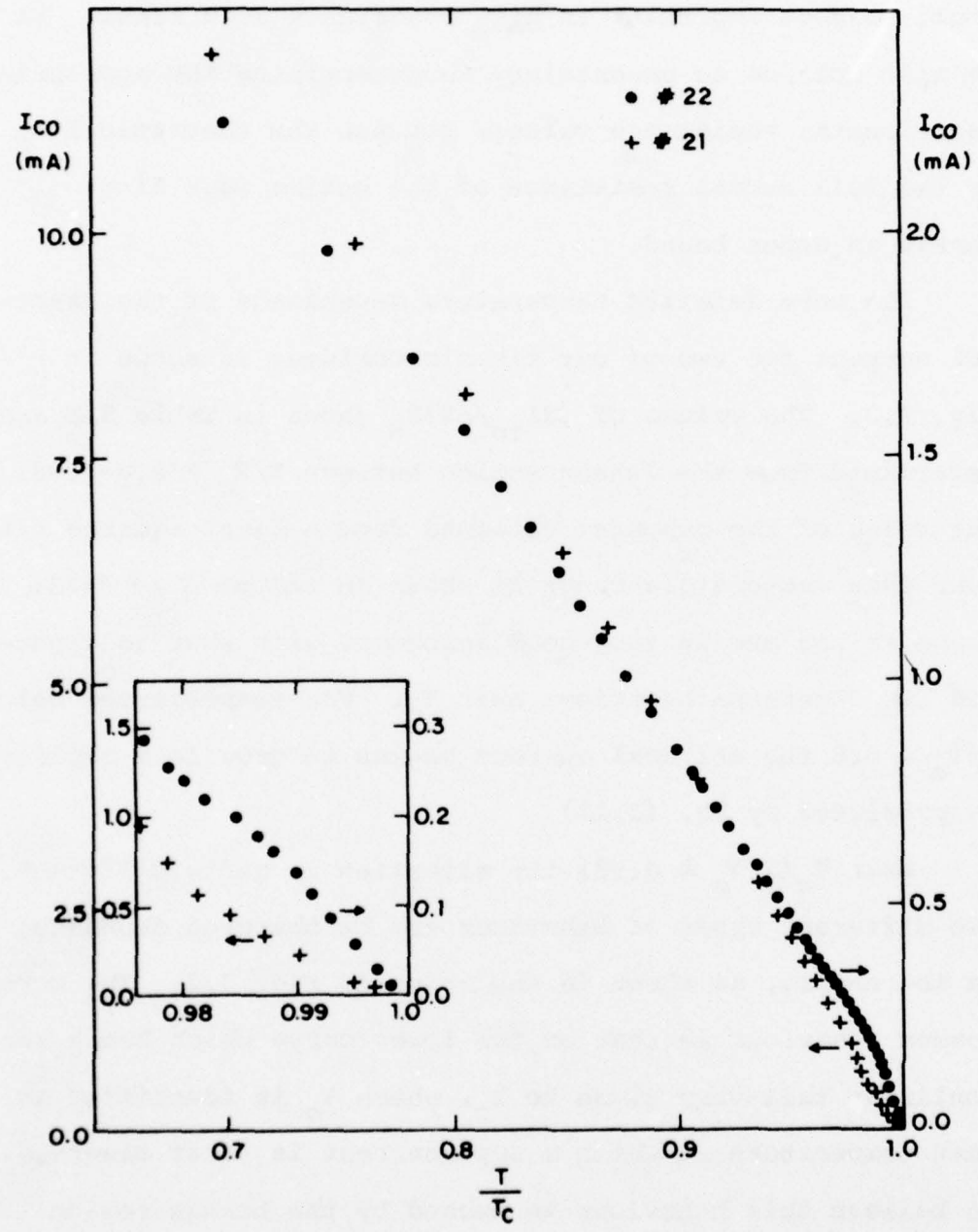

Fig. 3.2 Critical currents near T_c for two variable-thickness microbridges (# 21 and 22). Inset shows the critical currents very close to T_c.

measurements of the resistive transition of our samples, in which a resistive change of order 0.08 ohms occurs first as the bridge is cooled down. This resistive change corresponds to that expected from the contribution of the films between the superconducting leads and the microbridge. The differences between the transition temperature of the banks T_{cb} and the observed T_c vary from sample to sample and can be as large as 20 mK. Using the results obtained by Likharev and Yakobson[23] for the critical currents of SNS junctions we calculate, for $L/\xi(0) \sim 5$, that the observed T_c will be approximately $(T_{ci} - T_{cb})/2$ due to the proximity effect, so that the intrinsic transition temperatures of the bank and bridge materials differ by as much as 40 mK. Such differences are not at all surprising. The transition temperature of our tin films ($T_c \sim 3.8$ K) is always higher than that of bulk tin ($T_c = 3.722$ K) due to stresses. In view of the fabrication technique used in making the bridges, it is expected that the whole region around the bridge will be under very nonuniform stress conditions. This leads to the observed behaviour which is typically seen in tin and indium microbridges[24,25] and in our lead microbridges.

In some cases, the observed behaviour corresponds to the upper curve in the inset of Fig. 3.2. We interpret this as resulting from the bridge material having a higher intrinsic T_c than the banks. This is less common in tin microbridges but is usually observed in aluminum microbridges.[25]

In Fig. 3.3 the temperature dependence of I_{co} for a lead variable-thickness microbridge is shown. Lead microbridges have received little attention because it was assumed that the short coherence length [$\xi(0) \sim 0.08\ \mu m$] of lead would make them behave more like bulk filaments. However, the temperature dependence of the critical current is essentially the same as that shown earlier for tin microbridges. The linear "Josephson-like" behaviour is observed over the same temperature range $T/T_c \sim 0.8 - 0.98$. This linear temperature dependence of I_{co} is to be contrasted with earlier experimental results on tin and indium microbridges[26,4] in two-dimensional geometries which had critical currents which were somewhere between Josephson $(T-T_c)^1$ and bulk-like $(T-T_c)^{1.5}$ behaviour. This advantage of the variable-thickness geometry has also been confirmed recently by Wong et al,[27] who observe linear Josephson-like behaviour in fairly long ($\sim 1\ \mu m$) variable-thickness microbridges of niobium (which also has a very short coherence length). Recent calculations by Daalms et al[28] show that a small two-dimensional hyperbolic neck should have $I_{co}\ \alpha (T-T_c)^{1.25}$ and for a three-dimensional neck they obtain that I_{co} will vary linearly as outlined above or as in calculations which assume a short, one-dimensional bridge.[29-31]

While the overall behaviour of the critical current for both our tin and lead microbridges is qualitatively Josephson-like, some serious quantitative discrepancies in

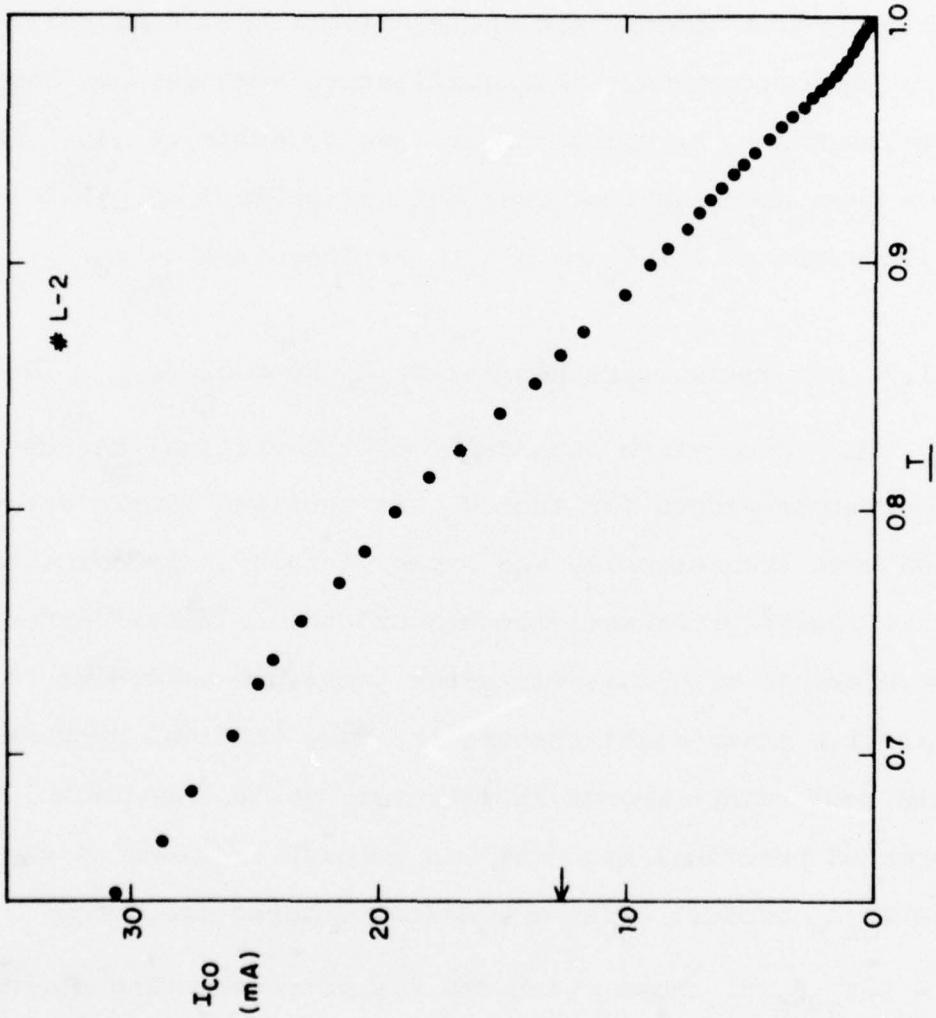

Fig. 3.3 Critical currents for a lead variable-thickness microbridge.

the $I_{co}R_N$ product near T_c remain. In Eq. (3.9), the conductivity should be a position-dependent quantity when the mean free path is of the order of the neck radius a. However, $|\Psi_o|^2$ is also proportional to ℓ when ℓ is less than the coherence length, and these effects should cancel to a first approximation. This qualitative argument has recently been confirmed by calculations made by Kulik et al.[32] which show that the behaviour does not differ from Eq. (3.10) near T_c, for either $\ell > \xi_o$ or $\ell < \xi_o$ as long as $a << \xi_o$.

3.1.2 Low Temperature Regime: $I_{co}R_N$ Products

The temperature dependence of the critical current of short microbridges far from T_c has received little attention both theoretically and experimentally. Experimentally it is always problematic to measure the critical current in the presence of hysteresis since premature switching to the resistive state might obscure the true critical current. This temperature regime is, however, quite important in terms of practical applications at high frequencies since the $I_{co}R_N$ product defines a characteristic frequency $\omega = 2eI_{co}R_N/\hbar$, above which the resistive shunting dominates the Josephson element, resulting in poorer performance. It is usual to compare experimental results at low temperatures to Eq. (3.11), because of its agreement with the A-L result near T_c. This then yields an upper limit for the $I_{co}R_N$ at

low temperatures:

$$I_{co}R_N = \frac{\pi \Delta(T=0)}{2e} = 0.24\ T_c(mV) \qquad (3.12)$$

While this form agrees well with experimental $I_{co}R_N$ products in tunnel junctions and high resistance point contacts,[33] the same is not true of microbridges and low resistance point contacts.[33,34] In Fig. 3.4 we show the $I_{co}R_N$ products at 2.1 K for our tin variable-thickness microbridges. All of our experimental results are above those expected from Eq. (3.11), which is shown as a solid line in Fig. 3.4. These discrepancies appear to be largest for our low resistance microbridges. This same trend is also observed by Yanson[34] in tin microbridges fabricated by electrical breakdown of metal-dielectric-metal structures. Calculations by Kulik et al.[35] and Mitsai[36] from microscopic theory in the limits $\ell << \xi_o$ and $a > \ell$ give a value of $I_{co}R_N$ at $T = 0$ which is 1.32 times larger than that given by Eq. (3.12). More recent calculations by Kulik and Omelyanchuk[32] in the limit $a << \xi_o$ and $a << \ell$ (for either $\ell > \xi_o$ or $\ell < \xi_o$), which correspond to limits closer to the experimental ones, yield a low temperature value of $I_{co}R_N$ which is twice as large of Eq. (3.12). As seen from Fig. 3.4, our results agree better with this prediction although some of the experimental results are still somewhat higher than the highest expected value. While these predictions are in closer

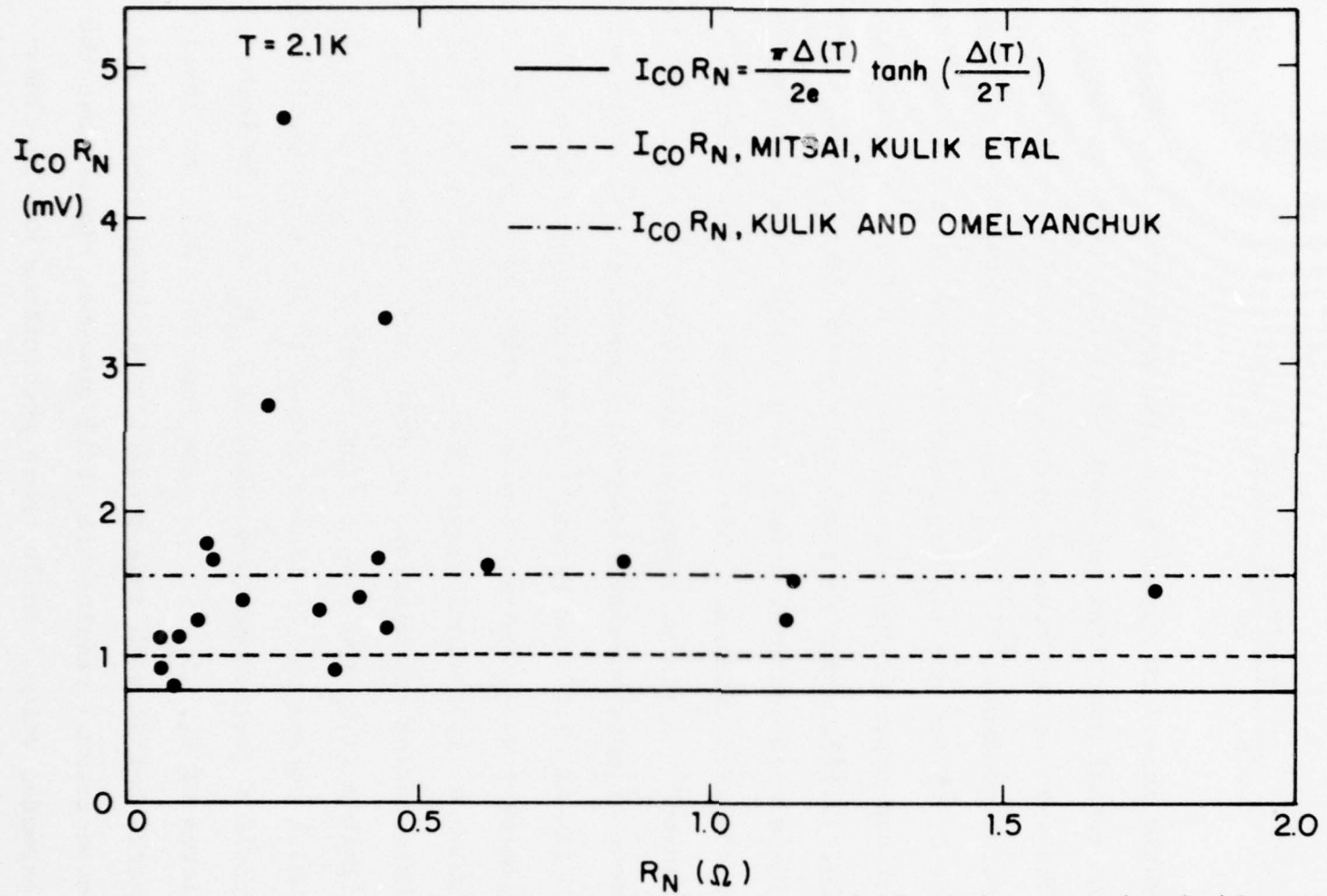

Fig. 3.4 $I_{co}R_N$ products versus R_N for tin variable-thickness microbridges.

agreement with our experimental results, the question remains of why this last prediction should be valid in microbridges and not in high resistance contacts which have the same ranges of neck radius a compared to ξ_o and ℓ, but nevertheless show $I_{co}R_N$ products which are below or in agreement with Eq. (3.11). It should be pointed out that the highest $I_{co}R_N$ values at low temperatures do not occur in those bridges with the highest $I_{co}R_N$ values near T_c as shown in Table 3.1.

It is clear that while recent theoretical predictions agree better with experimental results at low temperatures than the Ambegaokar and Baratoff result, further attention to this problem is required for conditions $\ell \sim \xi_o \sim a$ and in geometries closer to those of experiments.

3.2 The Wyatt-Dayem Effect

One of the most interesting effects observed in most types of Josephson junctions is the enhancement of the critical current I_{co} induced by microwave radiation. This effect was first noted in rather large ($W \sim 3$ μm, $L \sim 3$ μm) two-dimensional microbridges by Wyatt et al.[37] and Dayem et al.[38] though it had previously been observed by Shapiro[39] in tunnel junctions. While this effect has now been observed in most junction geometries,[40-42] and in the presence of phonon radiation,[43] no complete description of the effect for all geometries and systems is available. It is now generally accepted that this effect originates at least in part from an enhancement

of the gap resulting from the microwave excitation of quasi-particles to higher energies. This explanation was first proposed by Eliashberg.[44] However, his calculations were made for a thin superconducting film without any current flowing through it and they do not necessarily apply to our variable-thickness microbridges.

Experimental results on the Wyatt-Dayem effect in small weak links have shown a wide variation of temperature, power and frequency dependence. The results in our microbridges are no exception, as they differ from all previously published results for either the two-dimensional or variable-thickness geometry. All of our microbridges show an enhancement of I_{co} at both 10 and 32 GHz. At low microwave powers I_{co} increases slowly with power, reaches a maximum and then gradually decreases in a manner consistent with a decrease of I_{co} given by the zero-order Bessel function of the normalized microwave voltage. The magnitude of the enhancement varies from bridge to bridge from 4-43% and appears to depend on the weak link resistance. (In Appendix A, the maximum enhancement observed in all samples is included in the table of properties of all bridges; however, this is the largest enhancement observed, rather than an absolute maximum, as in many bridges the Wyatt-Dayem effect was not studied in detail.)

Our observation of the Wyatt-Dayem effect in our bridges agrees with the anticorrelation found by some workers between

good Josephson behaviour and microwave enhancement of the critical current. Jillie et al.[45] found, that among two-dimensional microbridges, bridges with the smallest enhancement exhibited the best Josephson properties. Klapwijk and Mooij[46] did not observe the enhancement in their high performance tin and aluminum variable-thickness microbridges. In our case, the enhancement is largest in low impedance microbridges which, as shown in Chapter Five, have their Josephson properties most severely affected by heating. Thus good diffusion of the quasiparticles appears to inhibit the Wyatt-Dayem effect.

The more detailed temperature dependence of the maximum enhancement observed in our microbridges is shown in Fig. 3.5 for both 10 and 32 GHz. These results are similar to those observed in most of our microbridges. At both frequencies, the enhancement is not observed very close to T_c. As the temperature is lowered, it appears first for 10 GHz and later for 32 GHz. As the temperature is reduced further the enhancement at 32 GHz becomes larger than that at 10 GHz. The enhancement at both frequencies reaches a maximum at $T/T_c \approx 0.97$ and decreases and disappears at lower temperatures, with the enhancement at 10 GHz going to zero first. However, some other experiments in weak links quite similar to ours have yielded significantly different results. Latyshev and Nad[46] observed the appearance of a critical current above T_c at both 10 and 23 GHz in cross-scratched tin

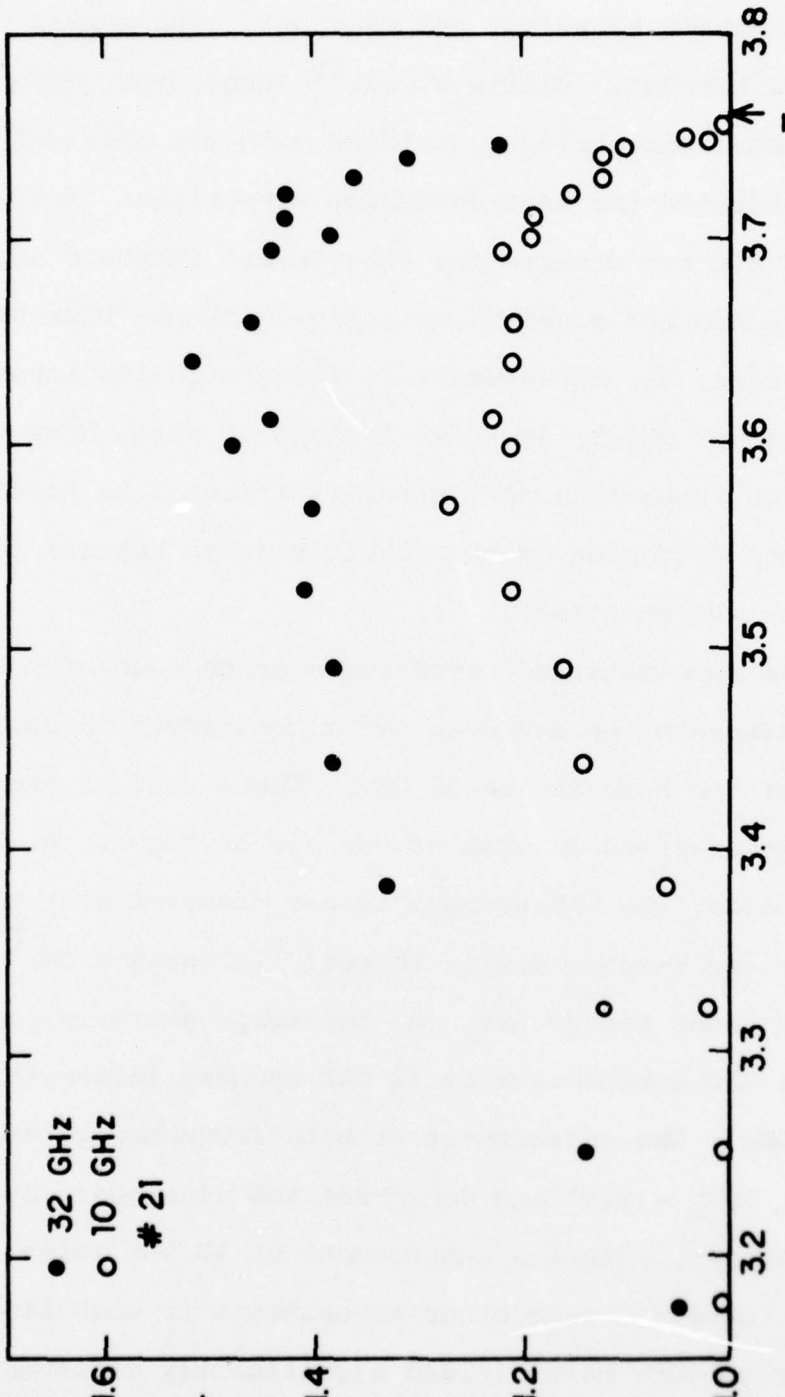

Fig. 3.5 Enhancement of the critical currents at 10 and 32 GHz for bridge #21.

microbridges, although not at higher frequencies. Levinsen[47] observed the enhancement in cross-scratched tin microbridges only below T_c at both 10 and 32 GHz but with a temperature dependence quite different than ours. At 10 GHz the enhancement began very close to T_c, reached a maximum at $T/T_c = 0.997$ and then rapidly decreased to zero. At 32 GHz the enhancement was observed first below $T/T_c = 0.99$, reached a maximum at 0.98 and remained many orders of magnitude larger than enhancement at 10 GHz at least down to $T/T_c = 0.95$. At present we do not know what accounts for these discrepancies.

While none of the experimental results can be said to be inconsistent with Eliasnberg's idea as to the origin of the effect, the experimental details differ from theoretical predictions. The model predicts the enhancement will occur for frequencies of order $\omega > 1/\tau_2$ where τ_2 is the electron-phonon inelastic-scattering time. This is certainly true in our tin microbridges ($\tau_2 \sim 10^{-10}$ sec.) and is consistent with the absence of the enhancement in our lead ($\tau_2 \sim 10^{-11}$ sec.) variable-thickness microbridges and with the onset of the effect at 200 MHz in long aluminum ($\tau_2 \sim 10^{-8}$ sec.) microstrips.[48] However, we do not observe the increase of the critical temperature predicted by theory at the frequencies and temperatures of our experiment. Such an increase is always seen in long Al and Sn strips[48] and in some short microbridge experiments.[37,46]

While it might be possible that a proper theoretical treatment of the problem including dc and rf currents in a constricted geometry would agree with most of the experimental results, it appears unlikely that it will resolve the inconsistencies between experiments. This is best illustrated by Table 3.2 where we show the combinations of material and geometry for which the effect has been observed at different frequencies. Note in the table, that the two systems one expects to be similar, the variable-thickness bridge and the point contact, show exactly opposite results.

It would appear from the above results that any further understanding of the problem will require theoretical analysis of more realistic configurations in closer agreement with the experimental conditions. Experimental differences could be identified by varying the details of the experiment such as the geometry of the bridges or the substrates used. It would also be interesting to study materials with very fast τ_2's at much higher frequencies

Table 3.2

Comparison of the Wyatt-Dayem Effect Observed in Different Materials and Geometries

Long Microbridges	
Aluminum:	Enhancement up to 300%. Enhancements from 200 MHz to 10 GHz. Increase of T_c observed.[48]
Tin:	Small (a few %) enhancements of I_{co} at 10 GHz.[4]
Two-Dimensional Short Microbridges	
Aluminum:	Small enhancements at 35 GHz down to $T/T_c = 0.86$. No increase of T_c reported.[49]
Tin:	Various results reported. Large enhancements observed in some cases. Increase of T_c seen at some frequencies. Enhancements below T_c seen from 1-76 GHz.[37,38,46,47]
Variable-Thickness Microbridges	
Aluminum:	No enhancement at 35 GHz.[50]
Tin:	Up to 50% enhancements at 10 and 32 GHz. No increase of T_c observed (this work) but no enhancements observed by others.[50]
Lead:	No enhancement observed at 10 and 32 GHz (this work).
Point Contacts	
Aluminum:	5-10% enhancements from 1 to 10 GHz.[41]
Tin:	No enhancements observed.[41]
Indium:	No enhancements observed.[41]
Niobium:	Small enhancements reported.[51]

Table 3.2 (continued)

Tunnel Junctions

Aluminum:	Small enhancements of I_{co} reported.[39]
	Direct enhancement of the energy gap by as much as 100%.
	Increase of T_c reported.[42]

CHAPTER FOUR

NONEQUILIBRIUM ENHANCED SUPERCURRENTS AT NONZERO VOLTAGES

4.1 Introduction

Once the critical current of a weak link is exceeded, a voltage develops across its length and the superconductor is in a time-dependent, dissipative state in which non-equilibrium effects are very important. This dynamic state arises from the superconductor responding to the voltage in such a way that phase coherence is maintained across the weak link. Then, as shown by Aslamazov and Larkin,[18] the order parameter in the center of the weak link will oscillate between the value of the order parameter at the banks, to zero and then back to the bank value in a Josephson period τ_J. This oscillating order parameter or energy gap will determine the energy of the quasiparticles and if τ_J is fast compared to the relaxation time of the quasiparticles τ_2, the quasiparticle occupation numbers will lag behind the energy changes, leading to changes in the superconducting properties of the weak link. At higher voltages (and thus frequencies) the order parameter will be limited by τ_{GL} and will not be able to relax instantaneously and further non-equilibrium corrections to the superconducting properties of the weak link will occur. At still higher voltages, Joule heating[4] will be of importance and will eventually dominate all nonequilibrium effects.

In this chapter we discuss the low voltage regime of the I-V characteristics of our tin variable-thickness microbridges, where heating is not of importance, and where a temperature dependent foot-like feature is observed. We find this feature to be consistent with the idea of an enhancement of the order parameter, and thus the supercurrent flowing through the weak link, due to the long relaxation time of the quasiparticles. In section 4.2 we describe in detail the phenomena observed experimentally. In section 4.3 we present first a qualitative discussion of the origin of this effect, before discussing in detail the more involved models of Aslamasov and Larkin[8] and of Golub.[7] The predictions of these models are compared to the experimental results in section 4.4 and good agreement is found with many aspects of the experimental results on our tin microbridges.

4.2 The Experimental Phenomena

The experimental phenomena to be explained have been observed in two-dimensional and variable-thickness microbridges of tin and indium made in various laboratories.[28,52-54] In Fig. 4.1, we show the overall I-V characteristics of a tin microbridge near T_c. At high voltages there is a substantial amount of curvature due to heating.[4] At lower voltages one observes the characteristic features of gap and subharmonic gap structures which will be discussed in Chapter Five. Finally, at the lowest voltages (0-50 μV)

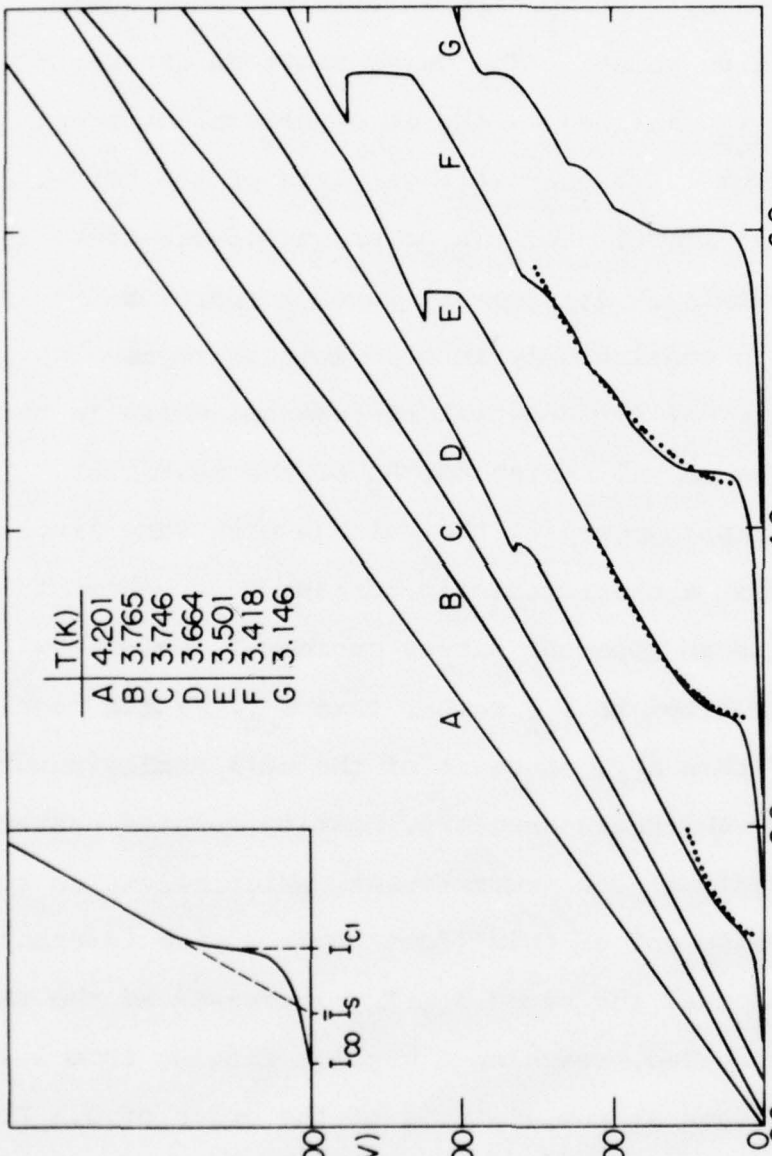

Fig. 4.1 I-V characteristics as a function of temperature for bridge #3. The inset defines the equilibrium critical current $I_{c\infty}$, the excess supercurrent $\bar{I}_s$, and the maximum enhanced supercurrent I_{c1}. The dotted curves show the shape of the I-V characteristic above I_{c1}, predicted by Aslamazov and Larkin.

there is a characteristic "foot", shown in detail in Fig. 4.2. Near T_c, the change to the resistive state above I_{co} is simply marked by a steep rise in voltage and a curve without inflection points. The curve shows an apparent excess current $\overline{I}_s$, defined as the zero-voltage intercept extrapolated from the higher voltage parts of the curve. Near T_c, $\overline{I}_s$ is a fraction of the order of 0.6-0.8 times the critical current I_{co}. At somewhat lower temperatures this feature develops continuously into an initial region (up to 5 μV) of constant differential resistance, which is much smaller than the normal resistance R_N of the weak link, followed by a rapid growth of the voltage with very little current change at a characteristic current I_{c1}. Above this region, there is an apparent excess current $\overline{I}_s$ which now appears to be related to I_{c1} rather than I_{co}, as its magnitude is larger than I_{co}. Because of the well cooled nature of our variable-thickness geometry, heating-related hysteresis[4] appears only at low temperatures, which allows us to follow the development of this "foot" over a wide temperature range. We find that the ratio I_{c1}/I_{ci} increases as the temperature is decreased, reaching a maximum ranging from 1.2-2 in our microbridges at temperatures of the order of 3.2 K. At still lower temperatures this ratio decreases, an effect that can in the most part be attributed to heating. The magnitude and temperature dependence of the differential resistance at low voltages, of the ratio I_{c1}/I_{co}, and of the apparent

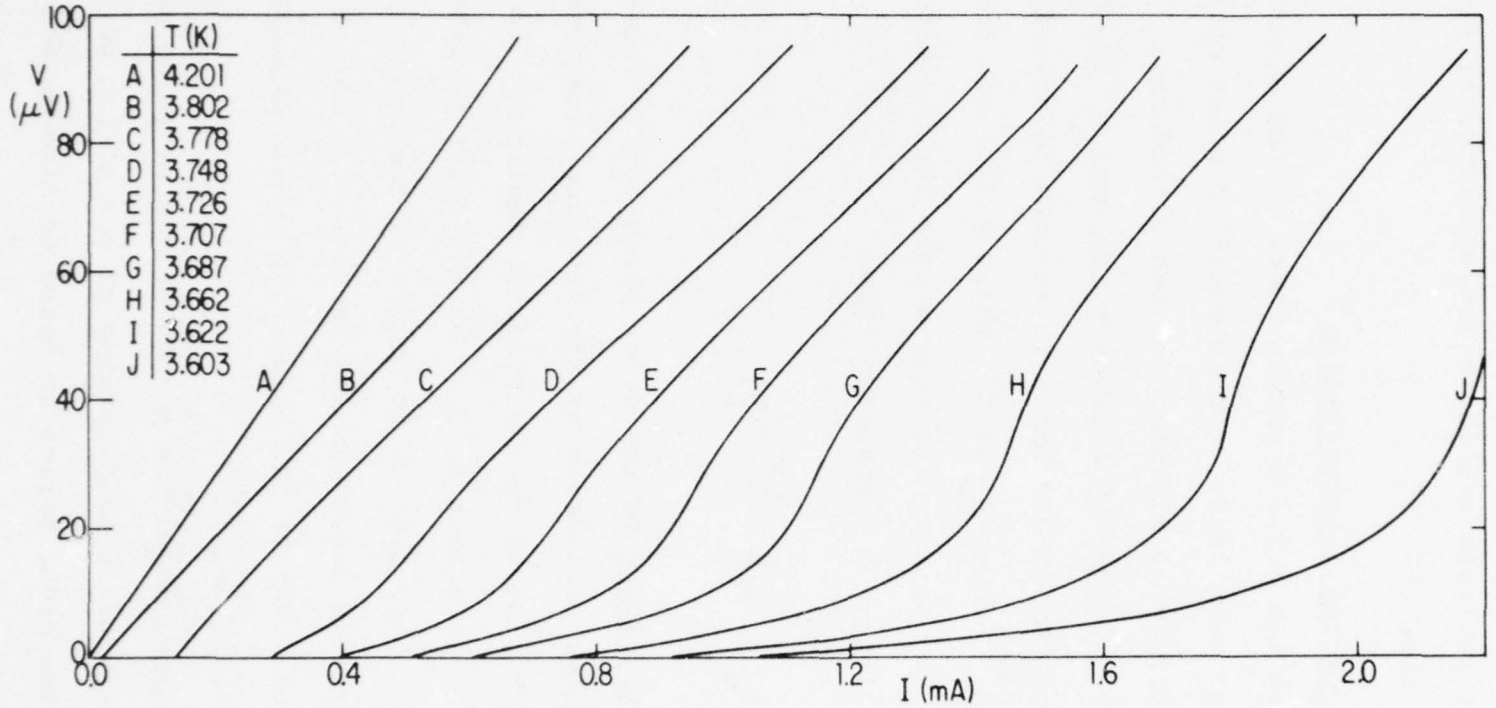

Fig. 4.2 Low voltage part of the I-V characteristic of Fig. 4.1 showing the development of the foot as a function of temperature.

excess supercurrent are the major experimental facts to be accounted for.

4.3 Theoretical Interpretation

In section 3.1.1 a simple model of the equilibrium behavior of weak links such as metallic point contacts and variable-thickness microbridges was introduced. In the form first proposed by Aslamasov and Larkin, the complex order parameter in the banks is assumed to have the values Ψ_o and $\Psi_o e^{i\varphi_o}$ where φ_o is the phase difference between the two sides and to vary linearly across the one-dimensional bridge of length L connecting them:

$$\Psi = \Psi_o \left[1 - \frac{x}{L} + e^{i\varphi_o} \frac{x}{L}\right] . \qquad (4.1)$$

Thus the magnitude of the order parameter in the very center of the bridge oscillates at the Josephson frequency between a maximum Ψ_o, equal to the value in the banks, to a minimum of zero and then back to Ψ_o. As the order parameter goes to zero, a phase slip of 2π occurs at the center of the bridge, but no physical discontinuity occurs as in the relaxation oscillation model or the phase slip models applicable to long microbridges.[55-57]

The above model has served as the starting point for several previous considerations of the effect of the relaxation of the order parameter based on time-dependent Ginzburg-

Landau (TDGL) theory and ad hoc extensions of it. Likharev and Yakobson[58] and Kramer and Baratoff[59] have numerically solved the TDGL equations for current-biased microbridges of different lengths. Relaxation effects become important for times comparable to the Ginzburg-Landau time $\tau_{GL} = \pi\hbar/8(T_c-T)$, which becomes significant primarily at high voltages. Likharev and Yakobson emphasized that end effects near the banks cause an "insufficient voltage", or apparent "excess current" of magnitude $0.75\ I_{co}$ at high voltages, and found the appearance of an additional phase-dependent conductance which had little effect on the I-V curves. Jensen and Lindelof[52] subsequently noted that the phase-dependent conductance would have a much greater effect on the I-V characteristics if the relaxation time were taken to be two orders of magnitude longer; it then leads to features in the I-V characteristics which are qualitatively similar to the foot of interest here. However, the use of such long times was given no physical justification, and Kramer and Baratoff have noted that it leads to inconsistencies within the analytic approximations that Jensen and Lindelof use. Furthermore, the use of TDGL is only strictly justified in the gapless regime which is not appropriate for these bridges at least near equilibrium at low current densities. Deaver et al.[60,61] have noted similar effects on the I-V characteristics resulting from time lags in a simple phenomenological nonequilibrium model.

Recent theories which go beyond the simple TDGL description take explicit account of the relationship between the nonequilibrium occupation of quasiparticle states and changes of the superconducting order parameter. We will first suggest qualitatively how such a relationship can lead to an enhancement of the supercurrent and then we will review the more specific calculations by Golub and by Aslamasov and Larkin on which this picture is based.

4.3.1 Qualitative Picture

To start, let us assume that the simple variation of the order parameter Eq. (4.1) also describes the space and time variations of the energy gap, whose magnitude determines the energy of each excitation through the relation $E_k = (\epsilon_k^2 + \Delta^2)^{\frac{1}{2}}$, where ϵ_k is the energy relative to the Fermi energy E_F of an excitation in momentum state k in the absence of the pairing interaction. The occupation of states with a given energy will relax toward the equilibrium value given by the Fermi function $f_o(E) = [1 + \exp(\beta E)]^{-1}$ by two processes, inelastic scattering (primarily by phonons) to and from states of other energy, and spatial diffusion at constant energy to and from adjacent regions with different occupations. Diffusion over the distance L will occur over a characteristic time $\tau_D = L^2/\pi D$, where D is the diffusion coefficient; for dimensions of order one micron, τ_D is comparable to $\tau_{GL} = \xi^2/D$, i.e., of order 10^{-12} seconds for tin.

Thus at energies which exceed the order parameter in the banks Δ_o, the diffusive exchange of particles with the banks will fix the occupation of these states at $f_o(E)$. Here we are neglecting the effects of Joule heating which would tend to increase the occupation of these states. Such effects are minimized in the variable-thickness geometry (which allows diffusion in three dimensions away from the bridge), and are insignificant, close to T_c, at the low voltage levels of interest here.

When the magnitude of the energy gap in the bridge is depressed below Δ_o, then E_k can be below Δ_o, and except for possible level broadening, these states can not exchange particles with the banks as shown in Fig. 4.3(a). In this case, the only mechanism for relaxing the occupation of those states with energies below Δ_o involves inelastic phonon scattering, which is characterized by a relatively long time τ_E which for tin is of order 10^{-9}- 10^{-10} seconds. Thus we should expect different regimes of behaviour depending on whether the Josephson period is long or short compared to τ_E.

At very low voltages where the Josephson period τ_J is much longer than τ_E, the relaxation will occur quickly on the scale of τ_J and the corrections to the equilibrium model will be small. This is shown qualitatively in Fig. 4.3(b)-(d). As the Josephson period decreases with increasing voltage, the rate of change of the order parameter will

Figure 4.3. a) Spatial variation of the gap in the middle of the Josephson cycle showing the quasi-particle states that can not diffuse into the banks.

b) Temporal variation of the gap in equilibrium (solid line) and in the presence of a lag (dashed line).

c) Temporal variation of excitation energy E_k for $\varepsilon_k = \Delta_o/2$.

d) Temporal variation of the quasi-particles occupation numbers for different values of the Josephson period relative to τ_E.

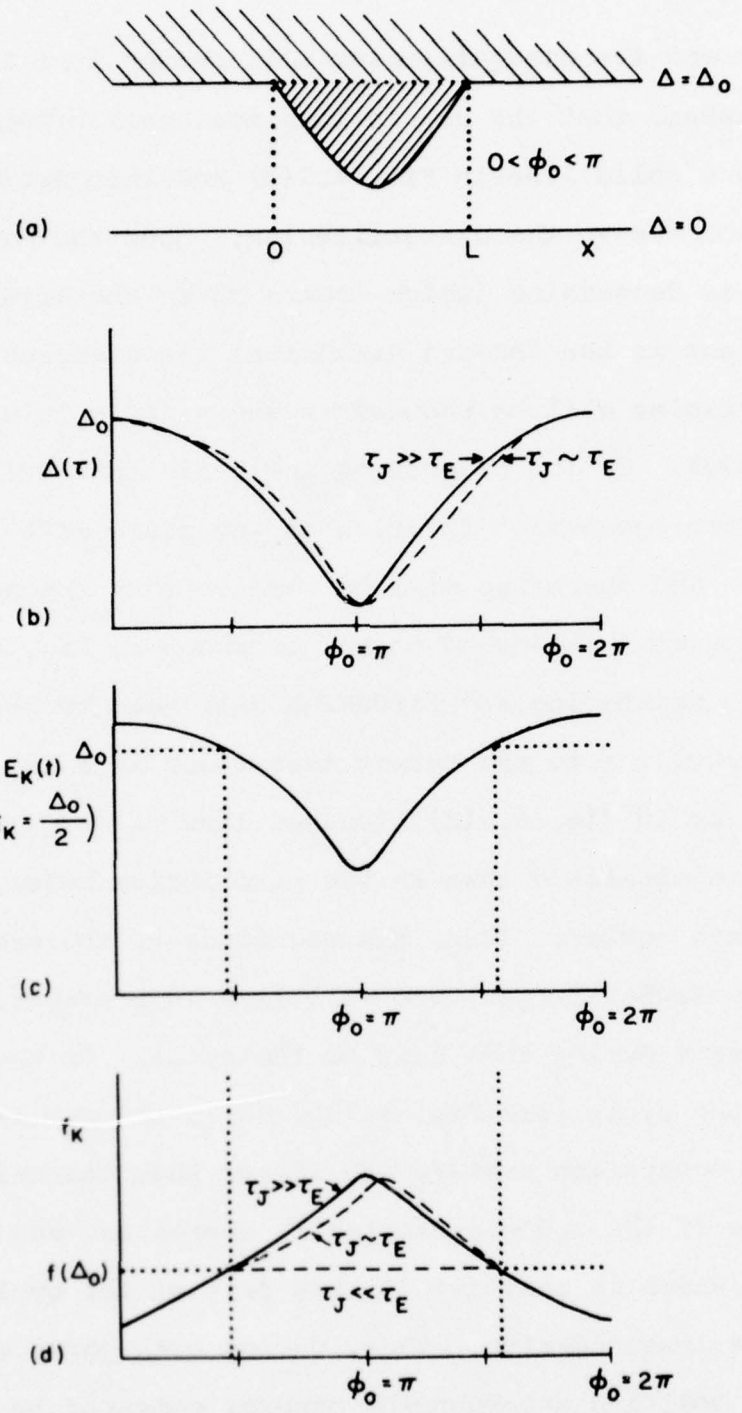
Δ = Δ0
0 < φ0 < π
(a)
Δ = 0
0
L
X
Δ0
Δ(τ)
τJ >> τE
τJ ~ τE
(b)
φ0 = π
φ0 = 2π
EK(t)
(εK = Δ0/2)
Δ0
(c)
φ0 = π
φ0 = 2π
rK
τJ >> τE
τJ ~ τE
f(Δ0)
τJ << τE
(d)
φ0 = π
φ0 = 2π

increase and the disequilibrium will become more important. Let us assume that the gap follows the equilibrium behaviour shown by a solid line in Fig. 4.3(b) and then estimate the correction due to the disequilibrium. When the magnitude of the gap is decreasing (which occurs while the bridge is carrying current in the forward direction) the energies of the quasiparticles will be reduced as shown for $\epsilon_k = \Delta_o/2$ in Fig. 4.3(c). In the absence of inelastic scattering and diffusion, the occupation fraction of any state will remain unchanged and therefore will be smaller than the equilibrium occupation at the reduced energy as shown in Fig. 4.3(d). Inelastic scattering and diffusion will tend to restore equilibrium, but to the extent that there is a lag in this process, as in Fig. 4.3(d), (dashed line $\tau_2 \sim \tau_J$), there will be fewer excitations than in the equilibrium model, as if the bridge were cooler. Thus, the magnitude of the order parameter will be somewhat larger, and will lead to a larger forward supercurrent during this half of the cycle. On the return part of the cycle [see Fig. 4.3(b)-(d)], the gap is increasing, the occupation numbers are larger than thermal, the magnitude of the order parameter is decreased, and the supercurrent (which is negative in this part of the cycle) is therefore less negative. Thus, during both parts of the cycle an extra positive supercurrent occurs, compared to the equilibrium model, and its magnitude should be proportional to the rate of change of the gap, and hence the voltage. Since

a current-biased junction at low voltages already carries a current $\sim I_{co}$ in the equilibrium model (because most of the time is spent near the maximum of the forward supercurrent part of the cycle), this additional supercurrent proportional to the voltage will result in a characteristic which starts from I_{co} and rises with a slope smaller than the normal resistance of the link, up to voltages of order $h/2e\tau_E$ (a few μV for tin). This describes the observed foot at low voltages, except one would still expect an initial vertical rise of the voltage at I_{co} similar to the RSJ model.

As the voltage begins to exceed $h/2e\tau_E$, the quasiparticle occupations cease to follow closely the equilibrium values and there should be a deficiency of quasiparticles in those states below Δ_o throughout the entire Josephson cycle. This suggests that the enhancement of the magnitude of the order parameter will reach a limiting value (corresponding to no relaxation at all), and the supercurrent will be enhanced in both the forward and reverse part of the cycle. Thus there should be a transition to a regime with the usual behaviour of a weak link (imperfectly understood though that may be) but with an enhanced critical current parameter I_{c1}. This is the region on each I-V curve which appears to have a critical current I_{c1} and a value of the apparent excess supercurrent $\bar{I}_s$ which is a fraction of I_{c1} rather than I_{co}.

The key to a more quantitative treatment of the situation described above is the derivation of generalized

Ginzburg-Landau equations for the order parameter which contain terms depending explicitly on the quasiparticle distribution function, together with Boltzman equations for the quasiparticle distribution function. This approach is adopted both by Aslamasov and Larkin and by Golub, but they make rather different physical and mathematical approximations. As a result, Golub's theory is more appropriate to describe the time variation within the Josephson cycle at low voltages, while that of Aslamazov and Larkin is more appropriate to describe the time-averaged limiting behaviour near I_{c1}.

4.3.2 Golub's Theory ($\tau_J > \tau_E$)

Golub describes the derivation of a modified form of the Ginzburg-Landau equation appropriate to the short weak link geometry, and a perturbation scheme for solving it at low voltages. The final equation has the form

$$\left[u_T\left(\frac{\partial}{\partial t} + i\mu\right) + u_L \frac{1}{|\Psi|}\frac{\partial|\Psi|}{\partial t}\right]\Psi = \xi^2 \frac{\partial^2\Psi}{\partial x^2} + (1 - |\Psi|^2)\Psi \qquad (4.2)$$

where the order parameter $\Psi = \Delta e^{i\varphi}/\Delta_o$ is normalized to its magnitude in the banks, and the times are normalized to the current relaxation time $\tau_o = \tau_{GL}/u_o$ where $u_o = \pi^4/14\zeta(3) = 5.79$ in the dirty limit. The usual TDGL equation would correspond to the values $u_T = u_o$ and $u_L = 0$. Instead, Golub

shows that u_T is very small and the new term is the most important one for typical materials. As we shall see, the smallness of u_T is related to the fact that the quasiparticle diffusion length rather than the coherence length governs the variation of quasiparticle electrochemical potentials, and the more important u_L term arises from the slow relaxation of disequilibrium by the mechanisms we discussed above.

Golub's equation is derived within the particular microscopic picture described by Schmid and Schön[62] (which Golub related to the work of Larkin and Ovchinnikov[63]). In this picture, the distribution function $f(E)$ of quasi-electron states as a function of energy E (with the convention that states inside the Fermi surface have negative energies) is given by the equilibrium Fermi function $f_o(E)$, plus odd and even correction terms associated with the longitudinal and transverse modes, respectively. The longitudinal correction f_L adds equal numbers of electron-like and hole-like excitations respectively above and below the Fermi surface, and is related to changes in the magnitude of the order parameter. The transverse correction f_T is associated with changes of the gauge invariant electrochemical potential difference $\mu - u_p = \Phi = \frac{1}{2}\left(2e\phi + \frac{\partial \varphi}{\partial t}\right)$, where φ is the phase of the order parameter and ϕ is the scalar potential; it adds quasi-electrons both above and below the Fermi surface corresponding to a net charge.

In computations the distribution function f(E) is weighted by appropriate functions $N_1(E)$, $N_2(E)$, and $R_2(E)$ shown in Fig. 4.4 for three different values of $\tau_E\Delta$. $N_1(E)$ is the normalized density of states, rounded off by phonon broadening which leads to the existence of a small but non-zero density of states between $-\Delta$ and Δ. $R_2(E)$ looks similar to the density of states, but it is an odd function of E and falls as Δ/E far from the Fermi surface. For large $\tau_E\Delta$, $R_2(E) \sim \Delta/(E^2 - \Delta^2)^{\frac{1}{2}}$ which is the usual weighting factor for the quasi-particle occupations in the BCS self-consistent gap equation; moreover, this form is precisely $N_1(E) \frac{\partial E}{\partial \Delta}$ where $E = (\epsilon^2 + \Delta^2)^{\frac{1}{2}}$. The physical significance of $N_2(E)$, which is important only in the region of "unphysical" states between $-\Delta$ and Δ, is less clear, but it appears to pick out states for which the transverse imbalance equilibrates rapidly with the superconducting condensate.

The steady-state Boltzmann equation for f_T balances inelastic electron-phonon scattering, spatial diffusion, and a transverse-mode quasi-electron sink rate $2\Delta N_2 f_T$. In situations where the spatial variation of f_T is slow, the equation has the approximate solution

$$f_T = \left|\frac{\partial f}{\partial E}\right| \frac{N_1(E)}{N_1(E) + 2\tau_E\Delta N_2(E)} \Phi \qquad (4.3)$$

which is like the distribution function for a normal metal, except for the missing energy range between $-\Delta$ and Δ where

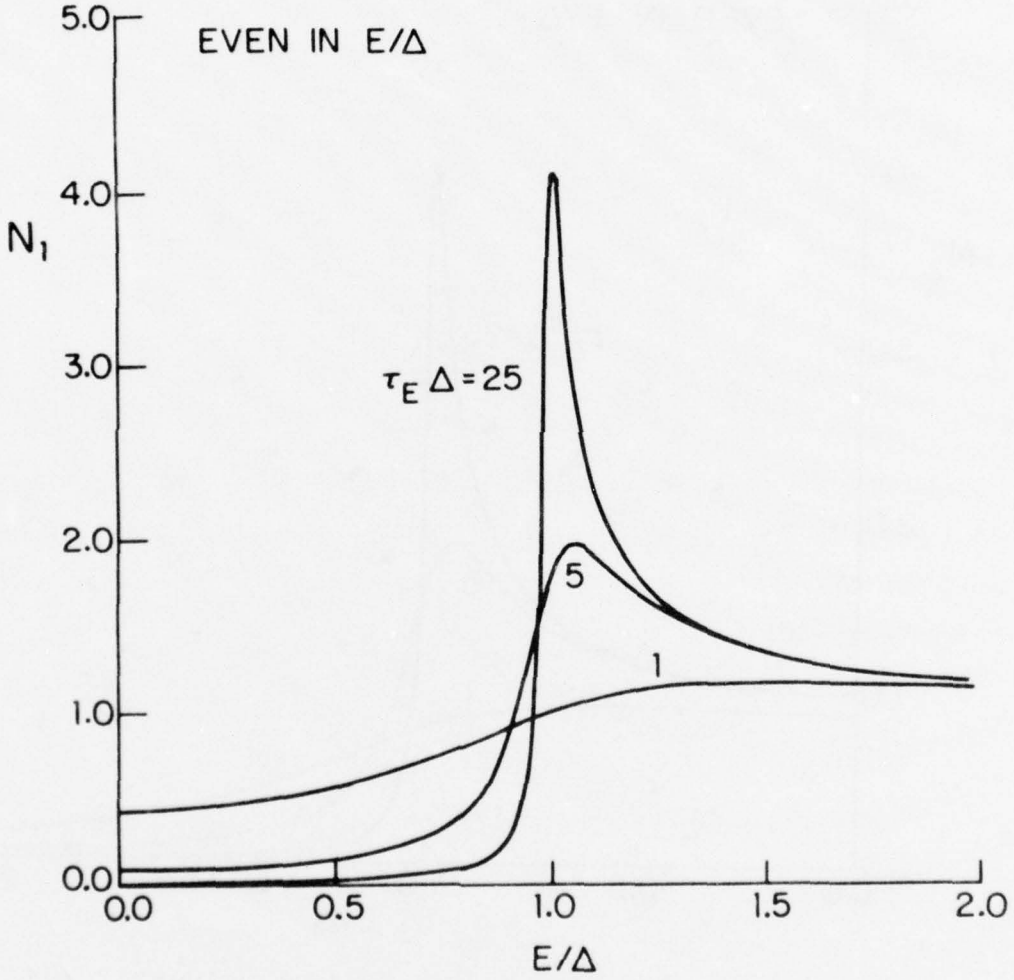

Fig. 4.4 (a) The function N_1 for various values of $\tau_E \Delta$.

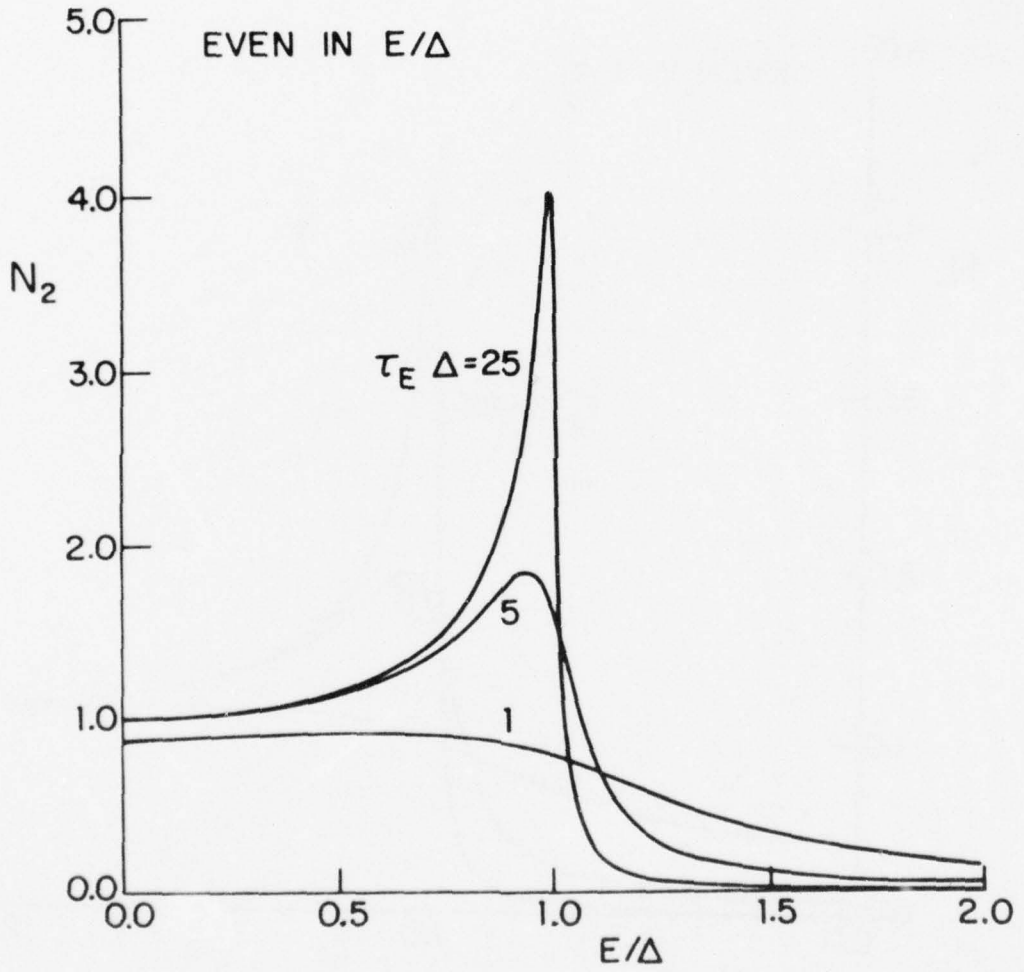

Fig. 4.4 (b) The function N_2 for various values of $\tau_E\Delta$.

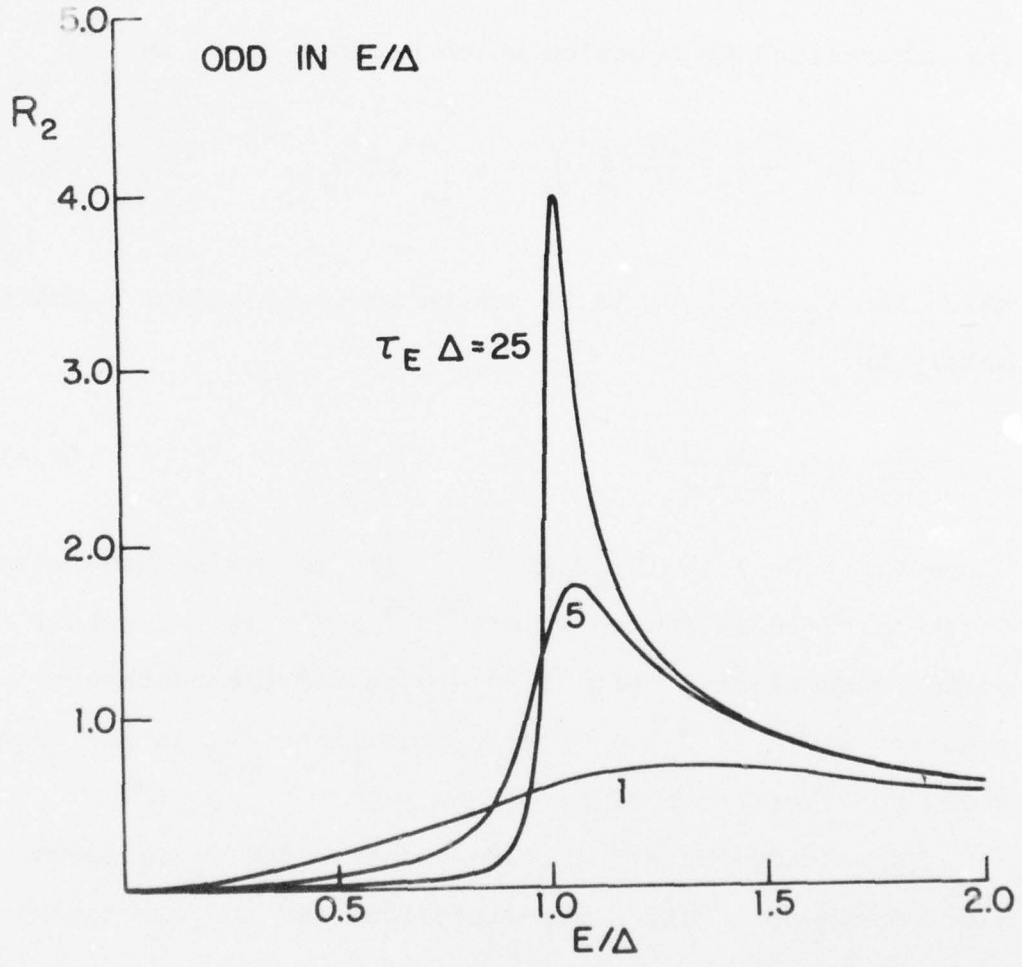

Fig 4.4 (c) The function R_2 for various values of $\tau_E \Delta$.

the sink rate is large. This solution also approximately satisfies the condition of electron-neutrality

$$\Phi = \int_{-\infty}^{\infty} dE\ N_1(E) f_T \ . \tag{4.4}$$

The generalized GL equation which depends on f_T is

$$\frac{\pi D}{8T_c}\left(\Delta^2 \frac{\partial^2 \varphi}{\partial x^2} + \frac{\partial \varphi}{\partial x}\frac{\partial \Delta^2}{\partial x}\right) = \Delta \int_{-\infty}^{\infty} dE\ N_2 f_T \tag{4.5}$$

which for f_T given by (4.3) can be shown to reduce approximately to

$$\text{div}\ \vec{J}_S = \frac{1}{\lambda_Q^2}\frac{\sigma}{e}\Phi \tag{4.6}$$

where $\lambda_Q = (D\tau_Q)^{\frac{1}{2}} = (D\tau_E T_c/\Delta)^{\frac{1}{2}} >> \xi(T)$ is the branch-mixing quasi-particle diffusion length[64,65] and σ is the normal state conductivity. With $\vec{J}_n = -\frac{\sigma}{e}\vec{\nabla}\Phi$ and the continuity equation $\text{div}(\vec{J}_s + \vec{J}_n) = 0$, this establishes λ_Q as the length scale for variations of Φ.

The steady-state Boltzmann equation for f_L balances electron-phonon scattering, diffusion, and the generation of disequilibrium at a rate $R_2\left|\frac{\partial f_o}{\partial E}\right| \frac{\partial \Delta}{\partial t}$ which for large $\tau_E\Delta$ reduces to $N_1\left|\frac{\partial f_o}{\partial E}\right| \frac{\partial E}{\partial \Delta}\frac{\partial \Delta}{\partial t}$. This justifies our interpretation of the origin of the disequilibrium as arising from the changes of the quasiparticle energies as the gap changes. Golub assumes that this disequilibrium relaxes by spatial

diffusion alone (although the effect of phonon scattering does enter through the broadened density of states), which leads to the solution

$$f_L = \frac{L^2}{12D} \left|\frac{\partial f_o}{\partial E}\right| \frac{R_2}{N_1^2 - R_2^2} \frac{\partial \Delta}{\partial t} \qquad (4.7)$$

where L is the length of the weak link. Thus f_L, shown in Fig. 4.5 is a function localized between $-\Delta$ and Δ, where the coefficient $(N_1^2 - R_2^2)$ of the diffusion term in the Boltzmann equation is small. The insets of Fig. 4.5 show, in exaggerated form, the shape of the total quasi-electron occupation $f(E) = f_o + f_L$ (with $f_T = 0$). Increased quasi-electron occupation at negative energies corresponds to fewer hole-like excitations below the Fermi surface. Thus we see that a decreasing gap decreases the number of electron-like and hole-like excitations, as suggested qualitatively above, and an increasing gap increases the number of excitations, compared to the equilibrium model. The resulting corrections to the gap are obtained directly from the generalized Ginzburg-Landau equation (neglecting unimportant static terms)

$$\frac{\pi D}{8T_c}\left(\frac{\partial^2}{\partial x^2} - \left(\frac{\partial \varphi}{\partial x}\right)^2\right)\Delta = \frac{\pi}{8T_c}\frac{\partial \Delta}{\partial t} + \int_{-\infty}^{\infty} dE\, R_2 f_L \qquad (4.8)$$

The two real equations (4.5) and (4.8) can be combined into a single complex equation of the form (4.2) where the u_T and u_L terms arise from the integrals of f_T and f_L, using

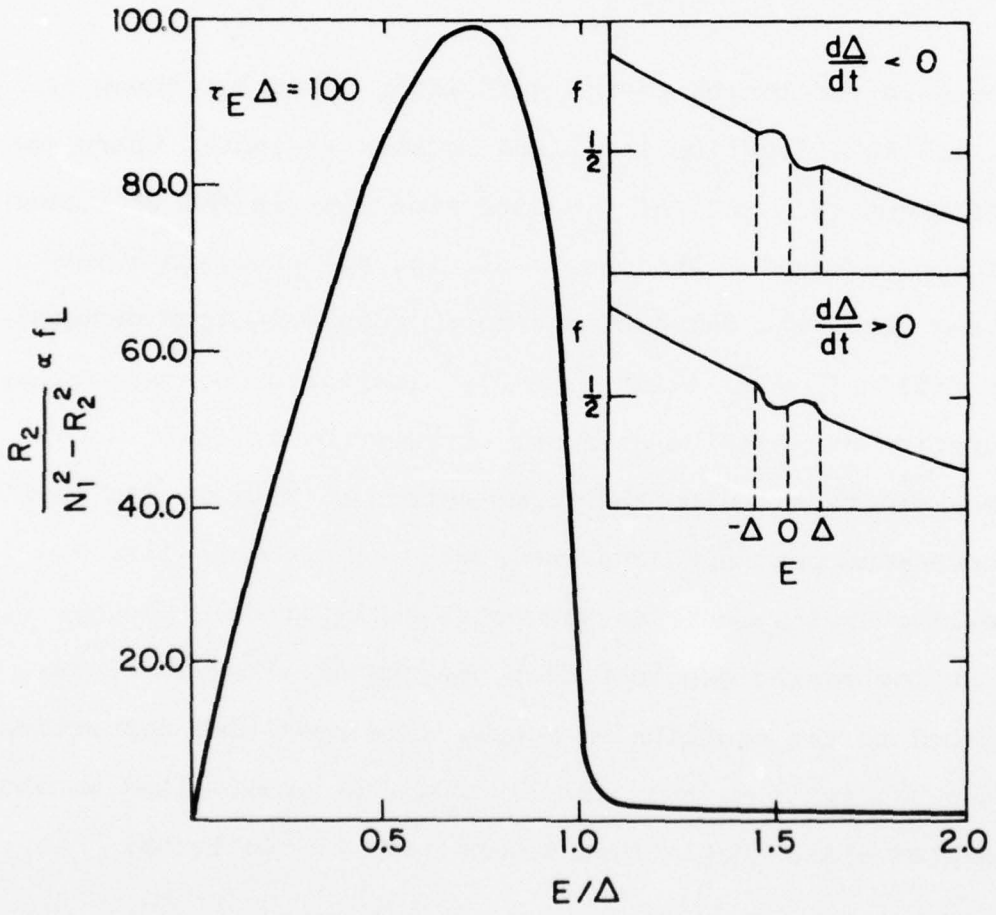

Fig. 4.5 Shape of the longitudinal correction f_L to the equilibrium distribution function f_0 as a function of E/Δ. The inset shows the overall distribution function with the nonequilibrium correction exaggerated for the cases $d\Delta/dt<0$ and $d\Delta/dt>0$.

the forms (4.3) and (4.7). At the level of approximation which leads to Eq. (4.6) $u_T \equiv \beta u_o$ is simply τ_{GL}/τ_Q and is small because the quasi-particle diffusion length $\lambda_Q = (D\tau_Q)^{\frac{1}{2}}$ is much longer than the coherence length $\xi = (D\tau_{GL})^{\frac{1}{2}}$ so that the quasi-particle current and hence the supercurrent must be nearly uniform on the length scale of the bridge. The other term u_L is given by $u_L = (1 + \gamma - \beta)u_o$ where $\gamma = I_\gamma (T_c/\Delta)(L^2/D)\tau_{GL}^{-1}$ and

$$I_\gamma = \frac{4}{3\pi^2} \int_{-\infty}^{\infty} d(E/\Delta) R_2^2 (N_1^2 - R_2^2)^{-1} \tag{4.9}$$

The variation of I_γ with $\tau_E\Delta$ is shown in Fig. 4.6. For large $\tau_E\Delta$, I_γ is relatively independent of τ_E, and the diffusion time L^2/D plays a major role.

Even for $u_T = 0$ it is difficult to obtain an exact solution to Eq. (4.2) but Golub has obtained a perturbation solution which is valid at low voltages. He assumes that the solution to (4.2) is of the form $\Psi = \Psi_o + \Psi_1$ where Ψ_o is given by Eq. (4.1) and Ψ_1 is a small nonequilibrium correction. Then one only needs to solve

$$\xi^2 \frac{d^2\Psi_1}{dx^2} = - u_L \frac{x}{L} \frac{\Psi_o}{|\Psi_o|^2} \frac{d\varphi_o}{dt} \sin \varphi_o \tag{4.10}$$

with boundary conditions $\Psi_1(0) = \Psi_1(L) = 0$. In Fig. 4.7(a) we show the real versus the imaginary part of the order parameter at equal time intervals for $\Psi_o (u_T = u_L = 0)$

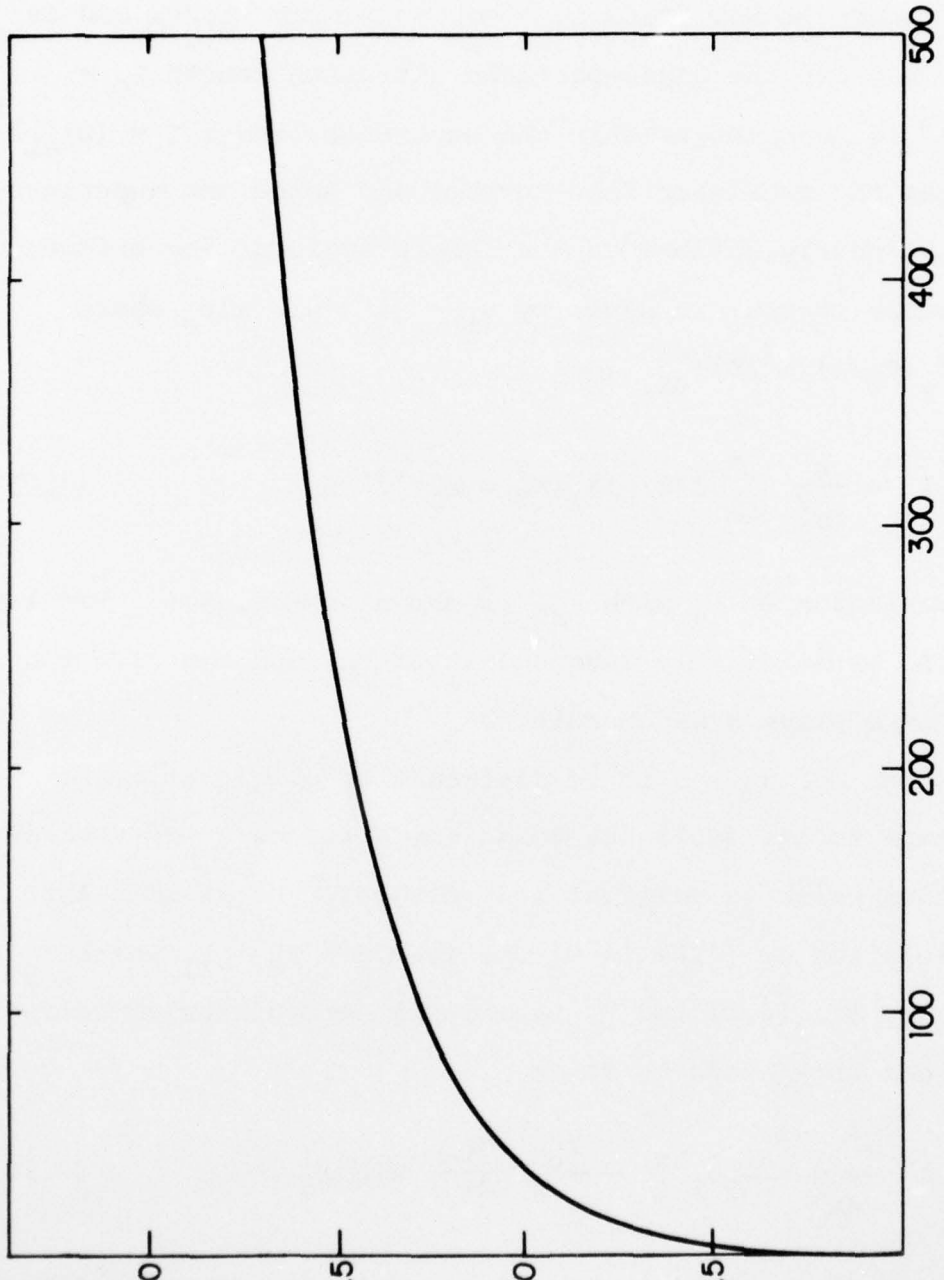

Fig. 4.6 Variation of I_γ with $\tau_E \Delta$.

Figure 4.7. Plot of the complex parameter at equal time intervals; each line corresponds to the values of the order parameter along the length of the bridge. a) Equilibrium case $u_T = u_L = 0$; b) Nonequilibrium case for $u_T = 0$, $d\bar{\varphi}_o/dt$ $u_L = 5$, where t is measured in units of t_o, the current relaxation time.

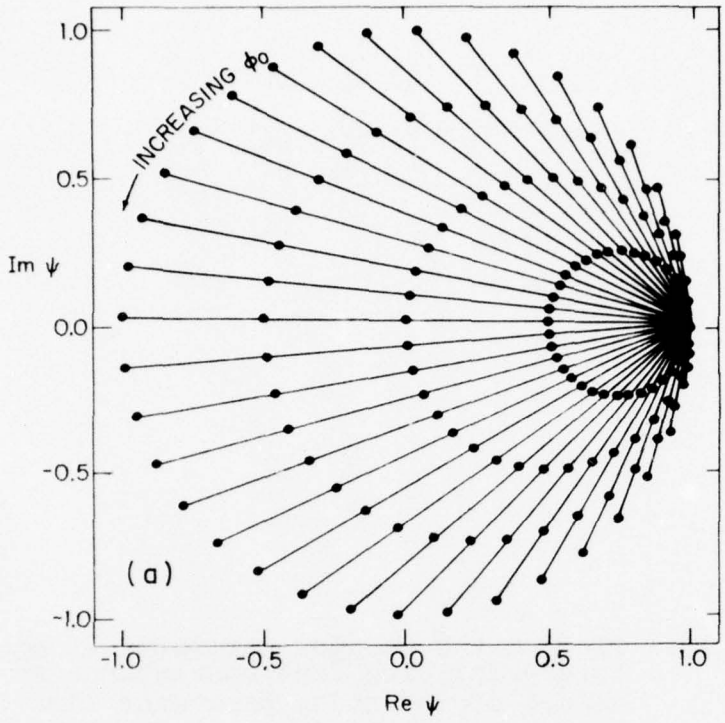
INCREASING ϕ_0
Im ψ
Re ψ
1.0
0.5
0.0
-0.5
-1.0
-1.0
-0.5
0.0
0.5
1.0
(a)

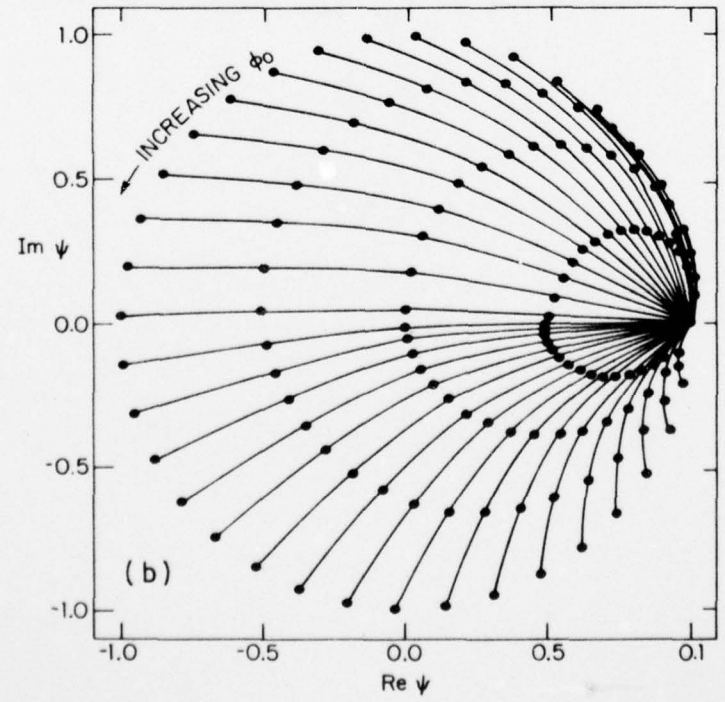
INCREASING ϕ_0
Im ψ
Re ψ
1.0
0.5
0.0
-0.5
-1.0
-1.0
-0.5
0.0
0.5
0.1
(b)

assuming that $\Psi_o(L) = e^{i\varphi_o}$, $\Psi_o(0) = 1$ and $\frac{d\varphi_o}{dt}$ = constant (voltage-bias). Each line corresponds to a projection of the spatial variation of the order parameter onto the complex plane with the ends of each line corresponding to the values at the ends of the bridge. In this case the supercurrent $I_s = I_{co} \sin\varphi_o$ is forward during the first half of the cycle and reversed during the second half.

The magnitude of the order parameter as a function of time and position in the bridge for the same conditions is shown in Fig. 4.8(a). Each curve in Fig. 4.8 corresponds to those in Fig. 4.7, but now the solid lines correspond to the first part of the cycle and the dashed lines to the second half of the cycle. In Fig. 4.7(b) and 4.8(b) we show similar plots but now $u_T = 0$ and $(d\varphi_o/dt)u_L = 5$ so that $\Psi = \Psi_o + \Psi_1$. Now, because of the disequilibrium, during the first part of the cycle the order parameter (which is decreasing in magnitude) is larger in the middle of the bridge than the $u_L = 0$ (equilibrium) value. At the middle of the cycle there is little difference from the equilibrium case because the magnitude of Ψ is stationary at $\varphi_o = \pi$. But in the second half of the cycle the order parameter in the middle of the bridge (which is now increasing in value) again lags and is now smaller than the equilibrium value. Thus, as discussed qualitatively earlier, the magnitude of the supercurrent is increased during the forward part of the cycle and

Figure 4.8. Plot of the magnitude of the order parameter as a function of space and time. The solid lines correspond to the first half of the cycle with the order parameter decreasing and the dashed lines to the second half of the cycle when the order parameter increases. There is a one-to-one correspondence between these curves and those shown in Fig. 4.7. a) $u_T = u_L = 0$; b) $u_T = 0$, $(d\varphi_o/dt)\, u_L = 5$.

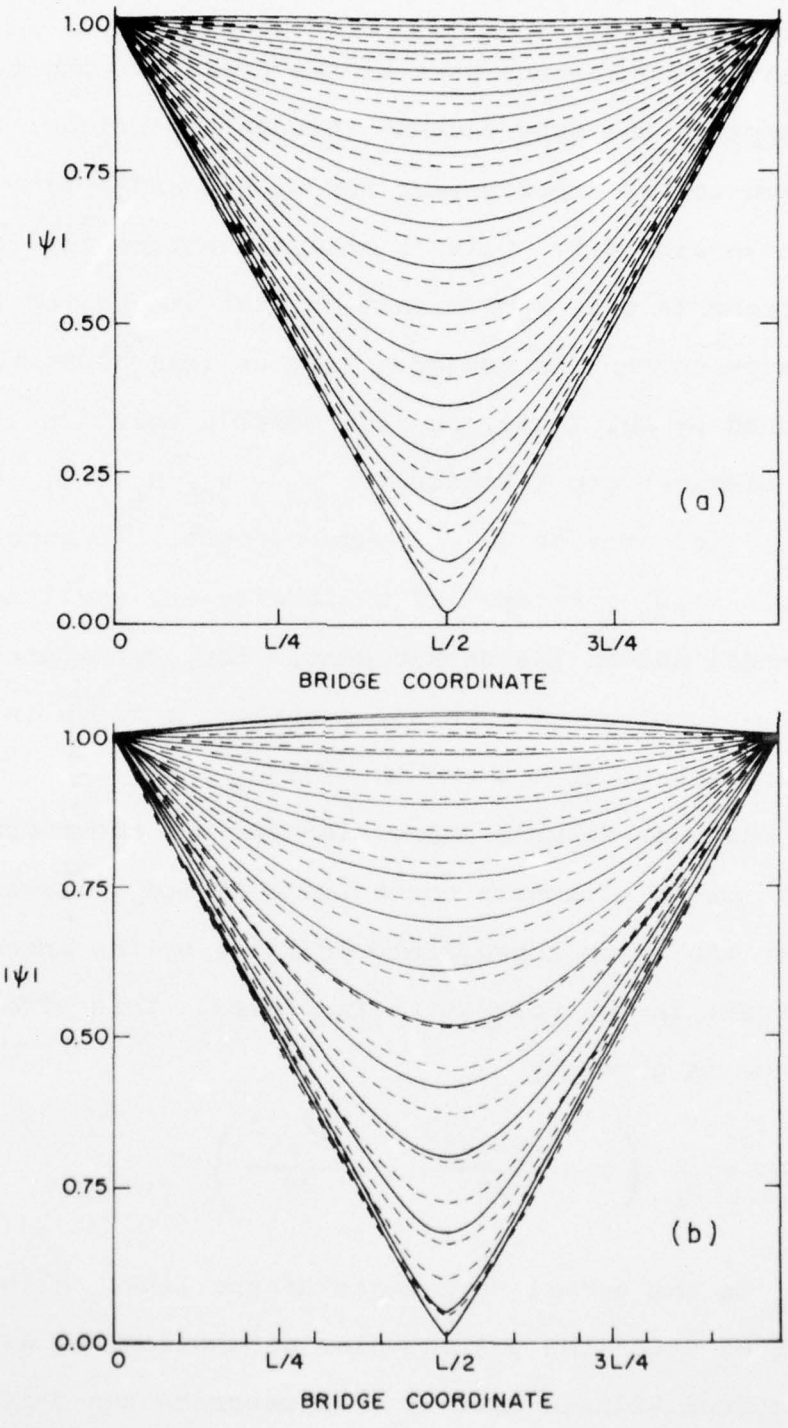
1.00
0.75
|ψ|
0.50
0.25
0.00
0
L/4
L/2
3L/4
BRIDGE COORDINATE
(a)
1.00
0.75
|ψ|
0.50
0.75
0.00
0
L/4
L/2
3L/4
BRIDGE COORDINATE
(b)

decreased in the reverse part of the cycle leading to a net enhancement of the supercurrent through the bridge. The correction to the supercurrent for $u_T = 0$ and $\left(\frac{d\varphi_o}{dt}\right)u_L = 5$ is shown in Fig. 4.9. Golub's analytic expression for the supercurrent is only approximate in that at a given time the actual supercurrent is not spatially uniform along the bridge as required by Eq. (4.8), so that Golub's solution (like that of Likharev and Yakobson for $u_T = u_o$, $u_L = 0$) is based on the spatial average of the supercurrent. In general, the deviations of J_s from spatial uniformity are small compared to the magnitude of the enhancement. For completeness the phase as a function of time and position is shown in Fig. 4.10, for $u_T = 0$, $u_L = 0$ and $(d\varphi_o/dt)u_L = 5$.

If one uses Golub's expression for the supercurrent, one then obtains an effective conductance at low voltages which is due to the extra conductance provided by the increasing supercurrent as the voltage is increased. This effective resistance is given by

$$\frac{1}{R_{EFF}} = \frac{1}{R_N}\left(1 + \frac{u_T L^2/\xi^2}{15} + \frac{u_L L^2/\xi^2}{24}\right) \qquad (4.11)$$

where R_N is the normal resistance of the link. Although this was derived under the voltage-bias assumption, we assume that in the current-biased case it will describe the differential resistance of the foot above I_{co}. As will be shown later, for the materials and temperatures of interest here $\gamma >> \beta$

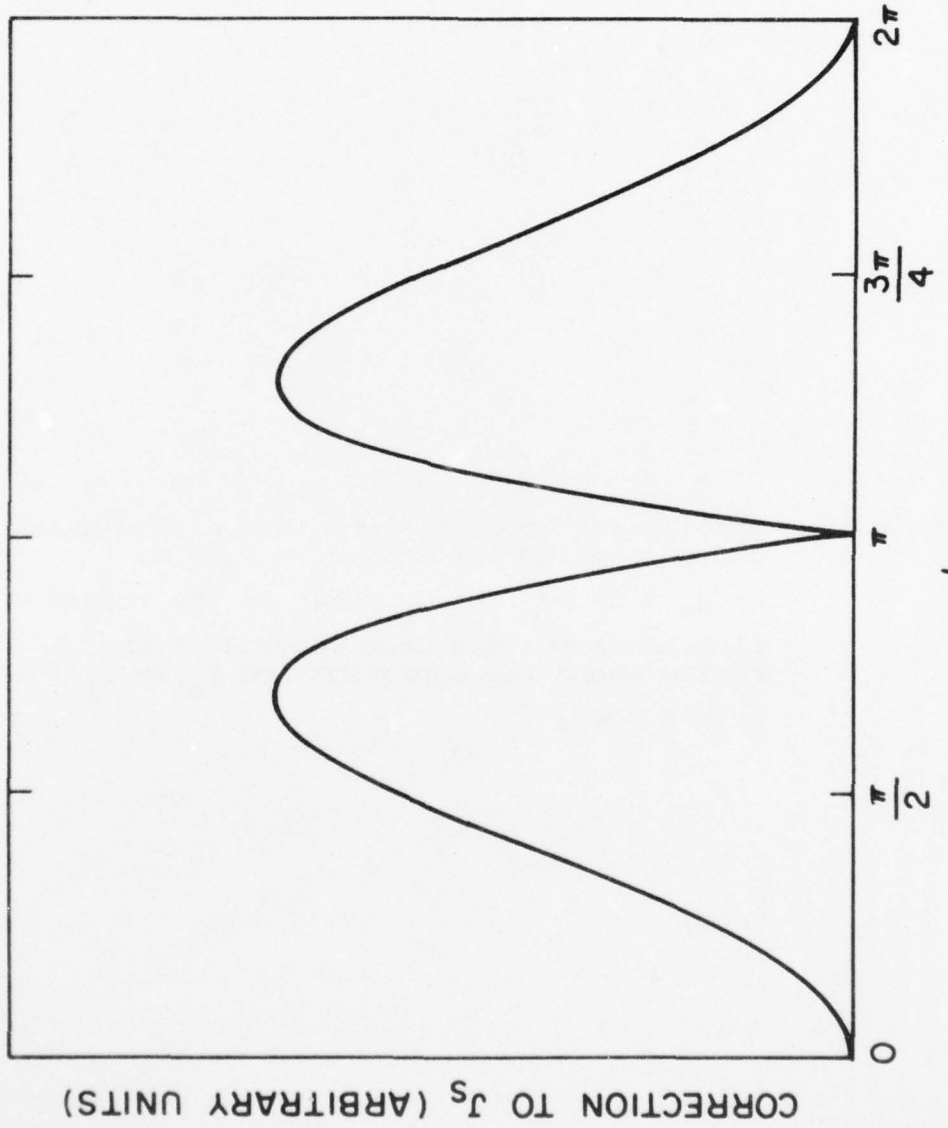

Fig. 4.9 Correction to the supercurrent at low voltages.

Figure 4.10. Spatial and temporal variation of the phase for a) equilibrium case $u_L = u_T = 0$; b) $u_T = 0$, $(d\bar{\varphi}_o/dt)\ u_L = 5$. In the second plot one curve has been removed in the regime where the approximation $\Psi_o >> \Psi_1$ breaks down.

AD-A049 779 HARVARD UNIV CAMBRIDGE MA DIV OF APPLIED SCIENCES F/G 9/5
NONEQUILIBRIUM PROPERTIES OF VARIABLE-THICKNESS SUPERCONDUCTING--ETC(U)
JAN 78 M OCTAVIO N00014-77-C-0085
UNCLASSIFIED TR-13 NL

2 OF 3
AD A049779

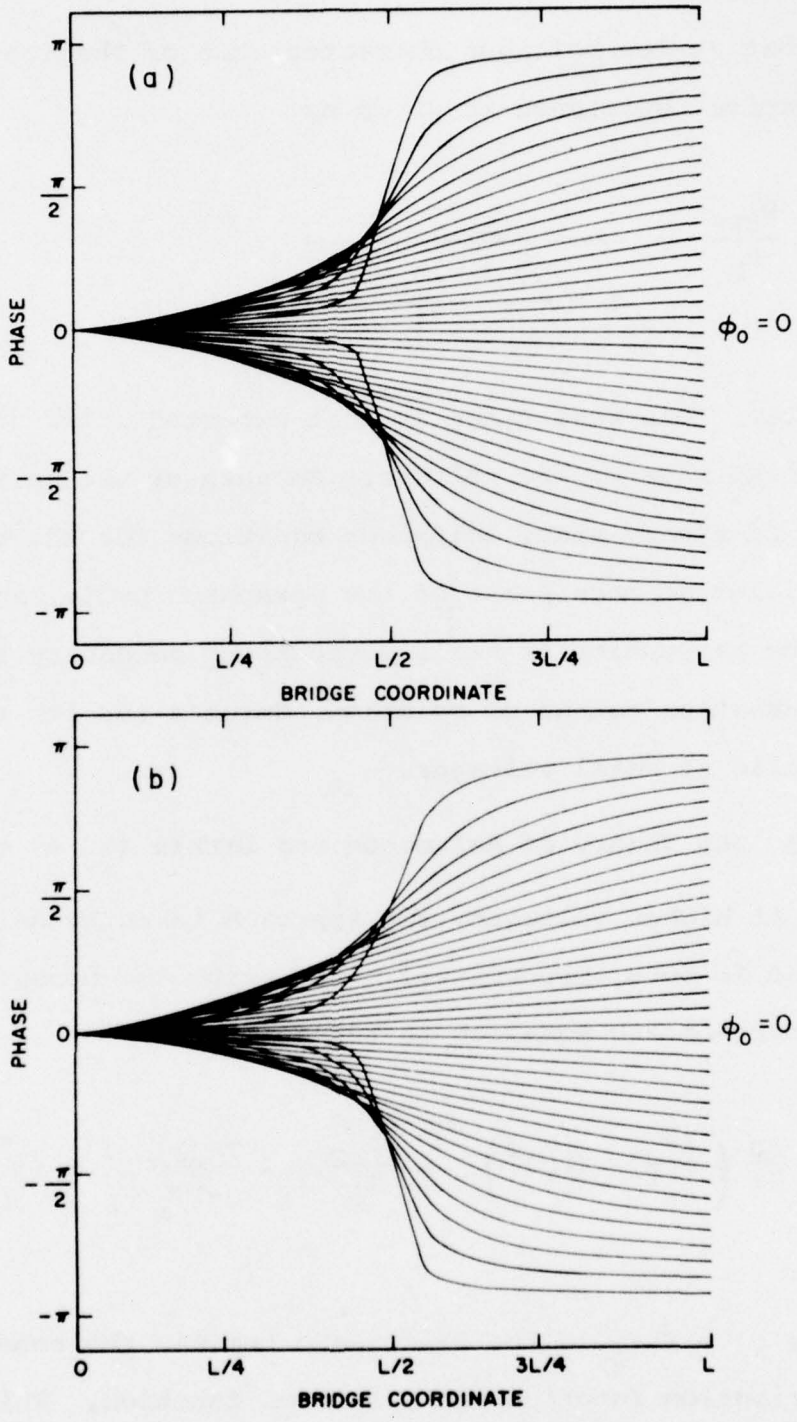
(a)
PHASE
π
π/2
0
-π/2
-π
0
L/4
L/2
3L/4
L
BRIDGE COORDINATE
$\phi_0 = 0$
(b)
PHASE
π
π/2
0
-π/2
-π
0
L/4
L/2
3L/4
L
BRIDGE COORDINATE
$\phi_0 = 0$

so that at low voltages characteristic of the foot the effective resistance is given by

$$\frac{R_{EFF}}{R_N} = \frac{1}{1 + \frac{(1+\gamma)u_o L^2/\xi^2}{24}} \tag{4.12}$$

However, this resistance is that expected after an initial RSJ-like rise of the voltage. Because of the initial assumption of steady state Boltzmann equations for the quasiparticles at each point of the Josephson cycle, and because of the assumption of small corrections necessary for the perturbation method of solution, Golub's results should only be valid at small voltages.

4.3.3 The Theory of Aslamasov and Larkin ($\tau_J \ll \tau_E$)

At higher voltages, the approach taken by Aslamasov and Larkin is more appropriate. They write the nonequilibrium Ginzburg-Landau equation in the form

$$\frac{\pi D}{8T}\left(\frac{\partial^2}{\partial x^2} - (\nabla\varphi)^2\right)\Delta - \frac{T-T_c}{T_c}\Delta - \frac{7\zeta(3)}{8\pi^2 T_c^2}\Delta^3 + \Delta\int_\Delta^\infty \frac{f'(E)dE}{(E^2-\Delta^2)^{1/2}} = 0 \tag{4.13}$$

where $f' = f - f_o$ is the difference between the nonequilibrium distribution function and the Fermi function. This assumes that the occupation of electron-like and hole-like excitations is equal, i.e., that the transverse mode is irrelevant

to the problem. Note that with neglect of certain terms, this equation is completely equivalent to Eq. (4.8). In particular $\Delta(E^2 - \Delta^2)^{-\frac{1}{2}}$ is just the limiting form of $R_2(E)$ for $\tau_E\Delta \to \infty$.

The real difference between the two approaches lies in the calculation of the nonequilibrium distribution function of the quasi-particles. Golub retains an explicit time dependence of the order parameter and integrates over energy, so that the magnitude (and sign) of the correction to the equilibrium distribution function of the quasi-particles depend explicitly on the time evolution of the gap. Aslamasov and Larkin, on the other hand, calculate the distribution function using an approach in which the quasi-particle distribution in the weak link is averaged over space and time very early in the calculation, and only the energy dependence is explicitly retained. This leads to rather different physical and mathematical approximations, and is justified only when the Josephson period is much smaller than the relaxation times. At low voltages where the linear foot is observed, the inelastic scattering time τ_E (of the order of 10^{-9} to 10^{-10} seconds for tin) is comparable to the Josephson period. Thus, the low voltage predictions of Aslamazov and Larkin should not be applicable. At higher voltages they calculate a time averaged distribution function for the excitations of the form

$$f(E) = \frac{1}{2}\left\{1 - \frac{\Delta_o}{2T}\left[1-(1- E/\Delta_o)^{5/4}\right]\right\} \qquad (4.14)$$

for $E < \Delta_o$. At energies above Δ_o, they assume that the distribution is thermal, because of the rapid diffusion. This function corresponds to a smaller than equilibrium occupation number for those excitations with energies less than Δ_o, just as was the case for Golub's theory during the most important (forward current) part of the cycle. Using Eq. (4.14) for f, they obtain that the last term in Eq. (4.13), which they denote $\Phi(\Delta)$, is given by

$$\Phi(\Delta) = \frac{\sqrt{2}}{3}\frac{\Delta_o^2}{T_c}\left(1- \frac{\Delta}{\Delta_o}\right)^{3/2} \qquad (4.15)$$

When this and the gradient terms are assumed to be the most important ones, the order parameter variations are characterized by a length scale $\eta = \xi(T)\left(\frac{T_c - T}{T_c}\right)^{1/4}$. If the length of the bridge L is $>> \eta$ they obtain that the supercurrent is enhanced and its maximum is given by

$$\frac{I_{c1}}{I_{co}} = K\frac{L}{\eta} \qquad (4.16)$$

where K is a numerical coefficient not calculated but of order one. This result, unfortunately, is derived under the rather stringent assumptions that $\xi >> L >> \eta$, which can be

satisfied only extremely near to T_c, since ξ and η differ only by a factor of three even at 0.99 T_c; nevertheless, it may be useful enough for comparison with experimental results. For currents larger than I_{c1}, Aslamazov and Larkin calculate the shape of the I-V curve based on certain assumptions about the current-biased nature of the weak link near the forward current portion of the Josephson cycle. The result they obtain is that the I-V relation should be given by

$$V = I_{co}R_N(I/I_{c1} - 1)^{\frac{1}{2}} \qquad (4.17)$$

Since this depends on the pulse-like nature of the response of the current-biased junction, it is presumably valid only for currents which do not greatly exceed I_{c1}.

4.4 Discussion of Experimental Results

Together, the Golub and Aslamazov and Larkin models, provide a semi-quantitatively satisfactory explanation for the I-V curves that we observe.

In Fig. 4.11 we show Golub's prediction Eq. (4.11) of the normalized resistance of the foot region as a function of temperature for several values of the bridge length parameter and two values of the inelastic-scattering time τ_E. In generating these theoretical curves, we have assumed an average value of Δ throughout the cycle of 0.8 Δ_o, a value $\tau_E = 8 \times 10^{-10}$ and 2×10^{-10} seconds, and a coherence length

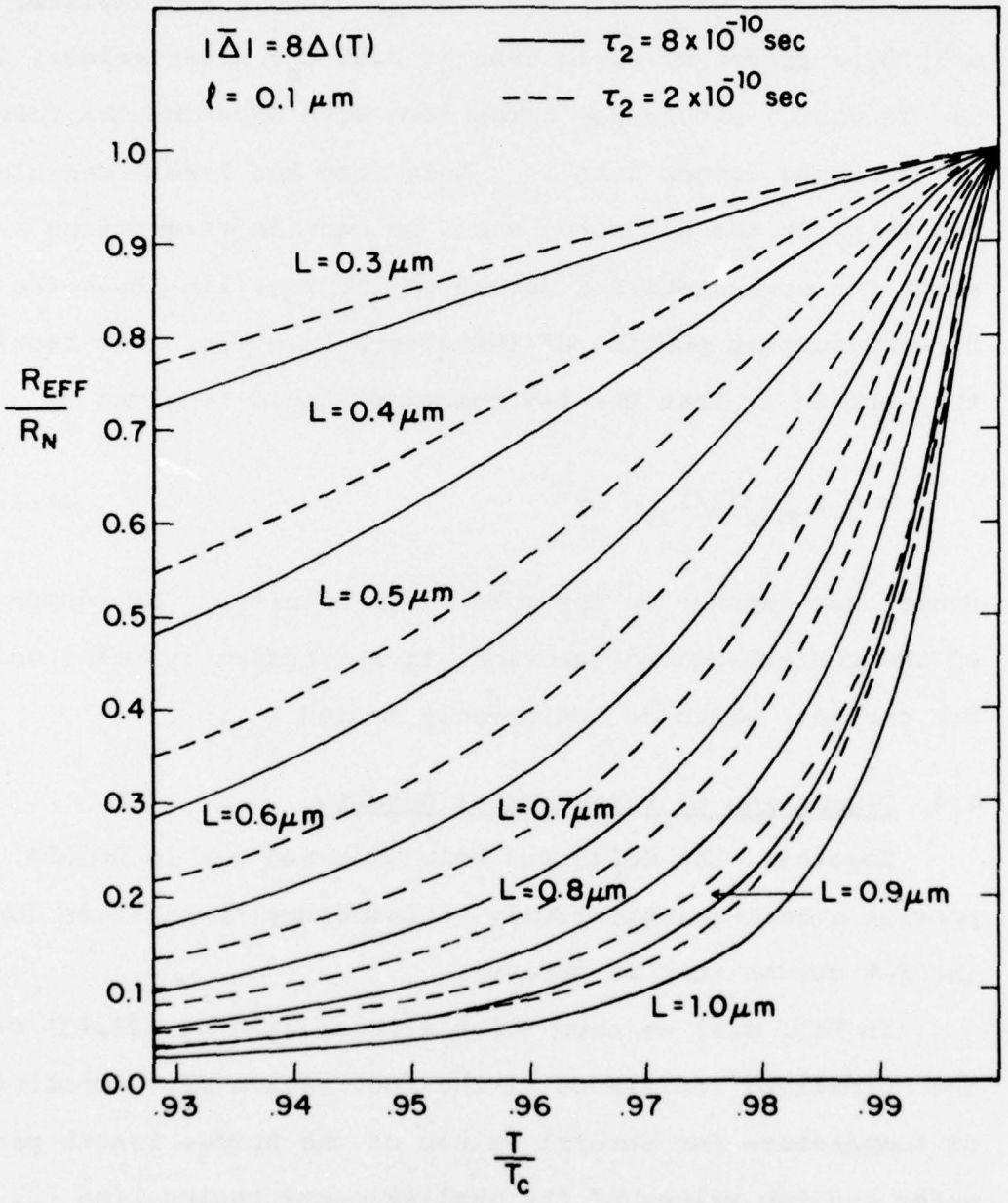

Fig. 4.11 Predictions of the model of Golub for the normalized resistance of the foot as a function of temperature for different values of the bridge length. The solid lines correspond to $\tau_E = 8 \times 10^{-10}$ seconds and the dashed lines to 2×10^{-10} seconds.

$\xi(0) = 0.13$ μm appropriate to our moderately clean films (mean free path 0.1 μm). The calculations are relatively insensitive to the value of τ_E because for temperatures less than 0.99 T_c, $\tau_E\Delta$ is at least 100, so that I_γ does not depend strongly on it. For bridge lengths 0.5-0.8 μm and temperatures of 0.9-0.98 T_c, the parameter γ in Eq. (4.12) is typically 10-20, while $u_o \approx 5.79$ so that the corrections to R_N can be substantial.

In Fig. 4.12 we show a plot of the normalized resistance of the foot region for six different bridges of similar geometries but varying resistances compared to the theoretical curves for L = 0.7-0.9 μm and $\tau_E = 8 \times 10^{-10}$ seconds corresponding to that determined experimentally by Skocpol et al.[57] Although SEM pictures (shown in Chapter Two) of our samples show that the distance between the edges of the banks is usually 0.2 μm smaller than that, the appropriate length for comparison with the theory is not well defined and may well be different than that distance. Near T_c, the experimental effective resistances are somewhat higher than predicted by theory. This may occur because the temperature dependence of the theory is not quite right, or it may result from the difference in T_c, discussed in Chapter Three, between the bridge and the banks, so that additional contributions of the proximity effect affect the results. For T_c we have used the temperature at which the linear temperature dependence of the critical current extrapolates to zero, which

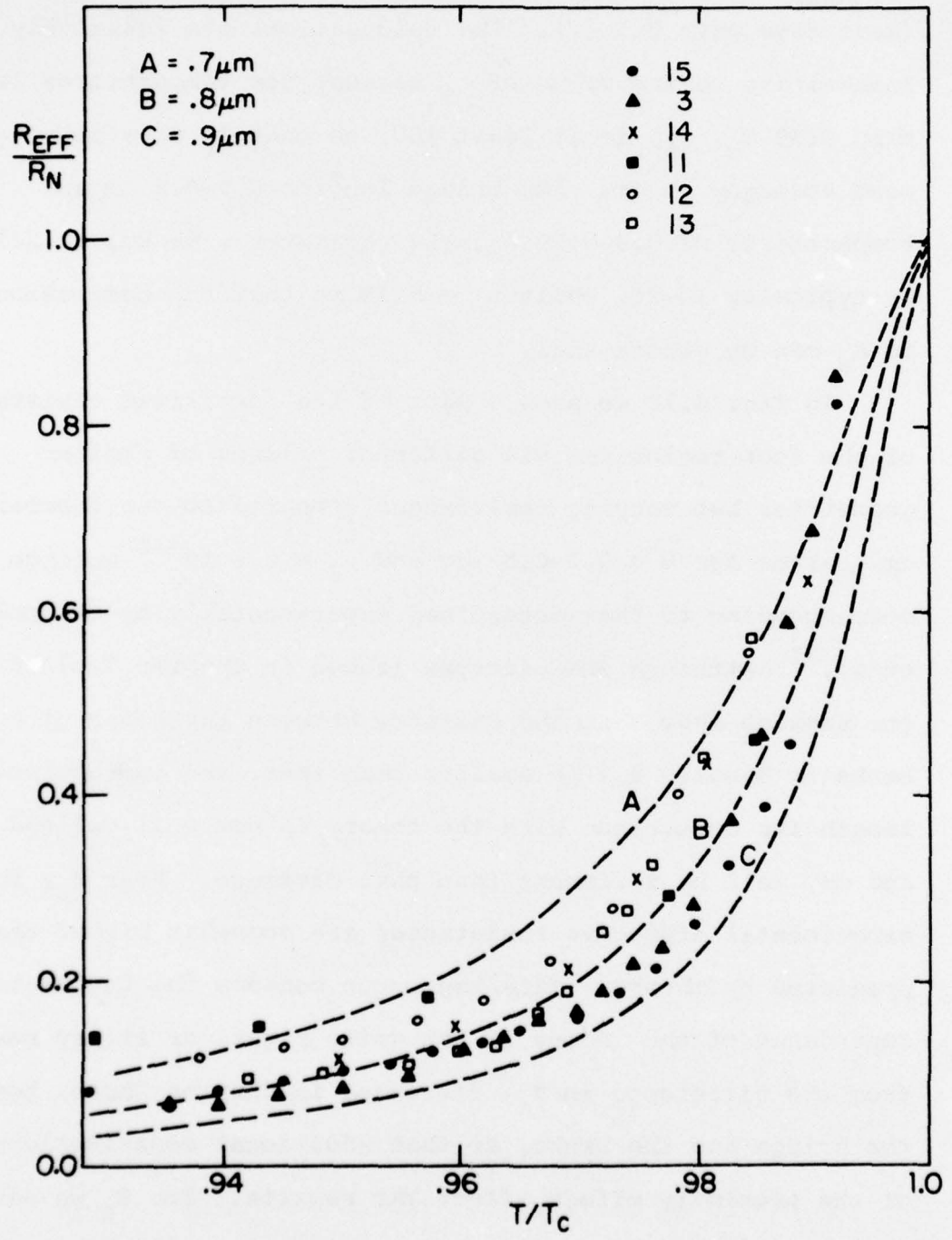

Fig. 4.12 The normalized resistance of the foot versus temperature. The data points are for six bridges and the dashed curves are Golub's predictions for various L values.

may differ by 10-20 millidegrees from the temperature at which the critical current actually appears to go to zero and by 10-20 millidegrees from the temperature at which the additional resistance of the entire banks is observed.

One feature of the prediction which is difficult to verify but appears somewhat suspect is the strong L^4 length dependence (arising from the L^2/D in γ together with the additional L^2/ξ^2 arising from the calculation of the enhanced order parameter). Our fabrication method is unable to make bridges with substantially shorter geometrical lengths, and attempts to make longer bridges by moving the knife sideways have been inconclusive because the first cut appears to always leave a noticeably deeper cut than the scraped elongation. Such bridges have normalized differential resistance values comparable to those of unelongated bridges. We have also varied the mean free path of our films, and found that the normalized differential resistance of moderately dirty films also does not differ decisively from the range observed in our moderately clean films. In very dirty films hysteresis was present very close to T_c and the foot could not be observed over a wide enough temperature range. Since the theoretical assumption of a well-defined length with rigid banks is obviously an idealization, the extent to which quantitative agreement with the normalized differential resistance and its length dependence should be expected is not clear.

Golub's approach does much better than the expression given by Aslamazov and Larkin for the slope of the foot, calculated assuming $\tau_E >> \tau_J$. The latter is several orders of magnitude smaller than the data. Since τ_J is comparable to τ_E throughout the foot region in our bridges, that expression should not be expected to apply, although the extent of the disagreement is somewhat surprising and may indicate some difficulty in that particular calculation by A-L.

At voltages above this initial region, the Aslamazov and Larkin solution is more appropriate. According to their model the super-current is enhanced up to a current I_{c1} which is of order $(L/\eta)\ I_{co}$. In Fig. 4.13, we plot the ratio I_{c1}/I_{co} as a function of temperature for the same six samples used in Fig. 4.12. Near T_c, the ratio grows very rapidly in a manner consistent with the temperature dependence $\frac{I_{c1}}{I_{co}} \propto (1 - T/T_c)^{\frac{1}{4}}$. At lower temperatures the ratio seems to saturate and remain constant rather than continuing to grow as predicted by theory. At much lower temperatures, heating effects start playing an important role and this ratio decreases until the two currents are the same. This is shown in Fig. 4.14 where the currents I_{c1} and I_{co} are shown for one bridge over the whole temperature range where a foot can be observed. The dashed lines in Fig. 4.13 correspond to Eq. (4.16). The appropriate values for KL vary from 0.5 μm to 0.65 μm. For K=0.8 the range and systematic variation of the

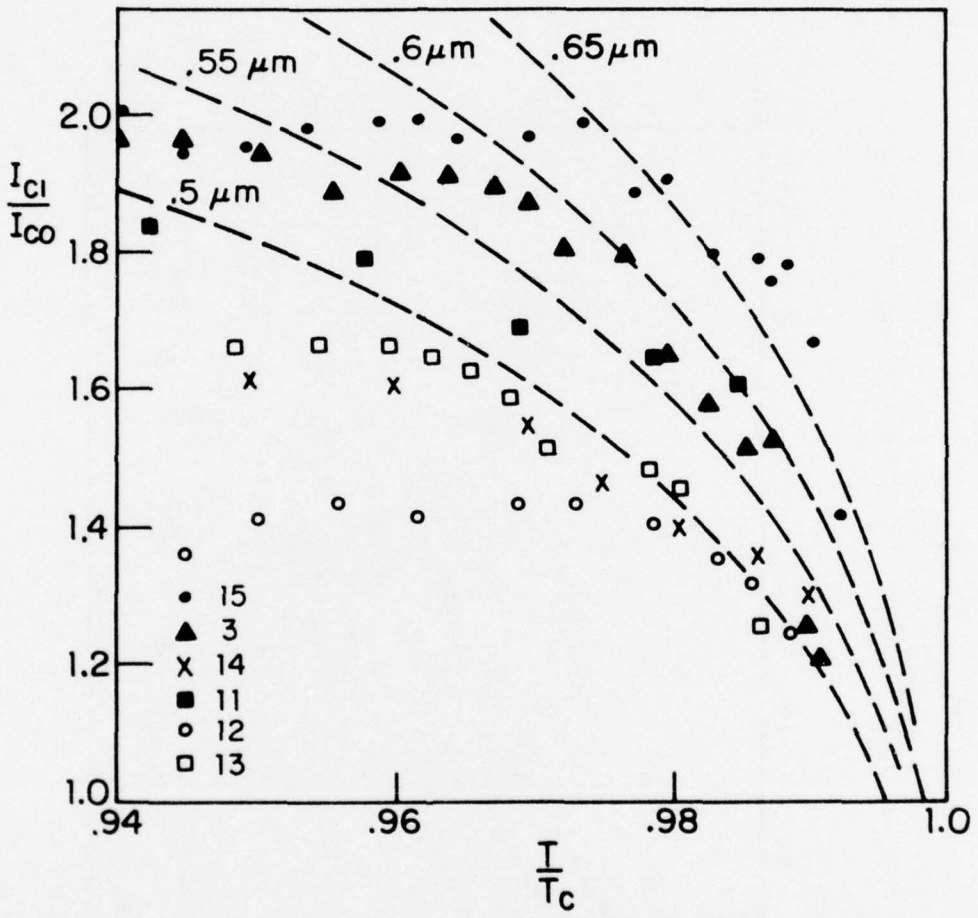

Fig. 4.13 The ratio of the enhanced supercurrent I_{c1} to the equilibrium critical current I_{co} as a function of temperature for the same bridges as in Fig. 4.12. The dashed curves correspond to the Aslamazov and Larkin prediction for different values of KL where K = 1.

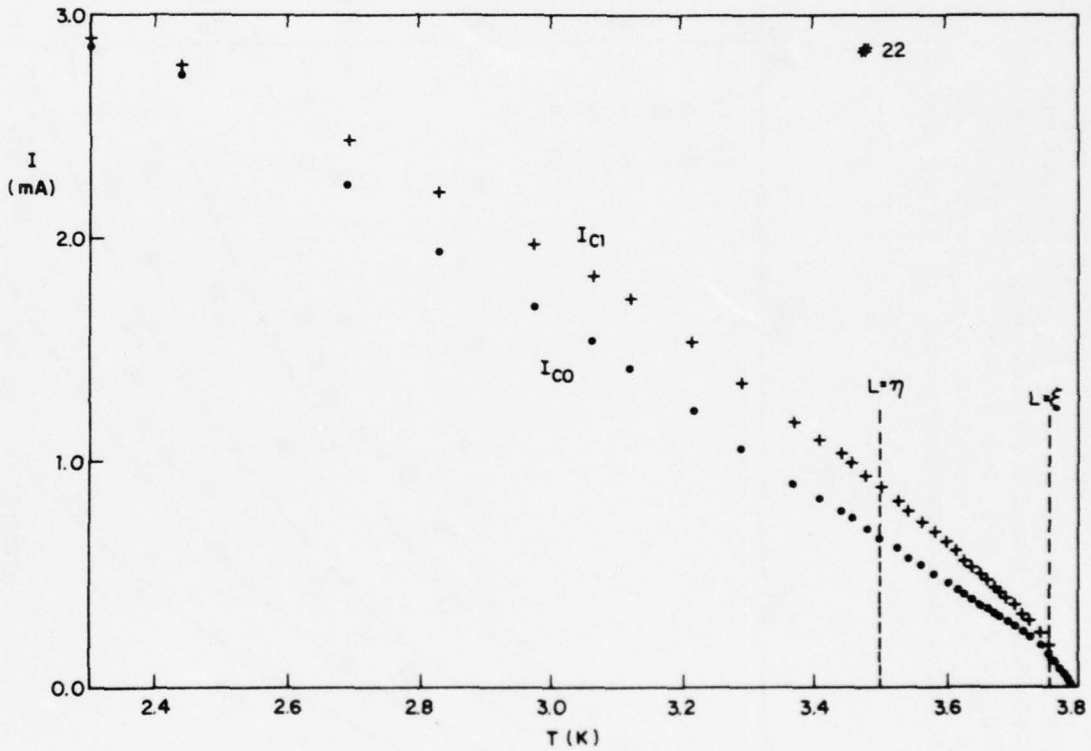

Fig. 4.14 Plot of the currents I_{co} and I_{c1} for bridge #22, showing the saturation of the growth of I_{c1} at temperatures far from T_c. The dashed lines indicate the regime of the Aslamazov and Larkin theory.

effective length from sample to sample is in agreement with the values determined in Fig. 4.12. The saturation observed at low temperatures for this ratio is not contained in the theory. As previously mentioned, the theory was derived under the conditions $\eta << L << \xi(T)$; both of these conditions are only marginally satisfied in the range shown in Fig. 4.13. At most the length of the bridges is two times the nonequilibrium length η, and at low temperatures, the coherence length becomes shorter than the length of the bridge. In Fig. 4.14 the regime $\eta < L < \xi(T)$ is indicated by the dashed lines. The order of magnitude of the effect does agree well with that predicted by the A-L theory.

For a limited range of currents above I_{c1}, AL's prediction Eq. (4.17) for the shape of the I-V characteristics can be fit reasonably well, although the test is far from stringent. Fig. 4.1 includes three theoretical curves of this form fit with the value of R_N and adjusting I_{c1} and I_{co} to an appropriate value for each curve.

For still higher voltages the theoretical situation is not at all clear. This is the region of apparent excess current $\overline{I}_s$ which is a feature of both the phase-slip model[55-57] and the TDGL theory.[58,59] Both predict that $\overline{I}_s$ should be a definite fraction of I_c. Presumably in the nonequilibrium situation described here the relevant critical current is I_{c1}, the effective critical current for the actual operating

conditions. In Fig. 4.15, we plot I_{co}, I_{cl}, and $\bar{I}_s$ for a typical bridge. Near T_c, $\bar{I}_s$ is about 0.6 I_{co} while at lower temperatures, it is about 0.7 I_{cl}. The qualitative change-over to the dependence on I_{cl} is clear-cut, and within this interpretation tends to support I_{cl} as the effective critical current under the operating conditions. Note that I_{co}, not I_{cl}, has the linear temperature dependence extrapolating to T_c expected for the zero dissipation critical current. The behaviour described is typical of all the microbridges and in Table 4.1, we include the values of $\bar{I}_s$ at low temperatures as well as the maximum value of I_{cl}/I_{co} observed in each bridge. Note that the value of $\bar{I}_s/I_{cl}$ does not vary much from bridge to bridge. The same is not true of I_{cl}/I_{co} as bridges with equivalent resistances do show substantial differences from a low of 1.2 to a high of 2.0.

Some comments should be made about the material dependence of the effects discussed. The characteristic feature of interest has been observed only in microbridges made of tin and indium. Since these materials are very similar the theory should describe both equally well. On the other hand the I-V characteristics of short aluminum microbridges of lengths similar to ours do not show similar effects.[28] We have calculated the effective resistance of the low voltage region for aluminum microbridges of similar lengths and find that the change from the normal resistance would be

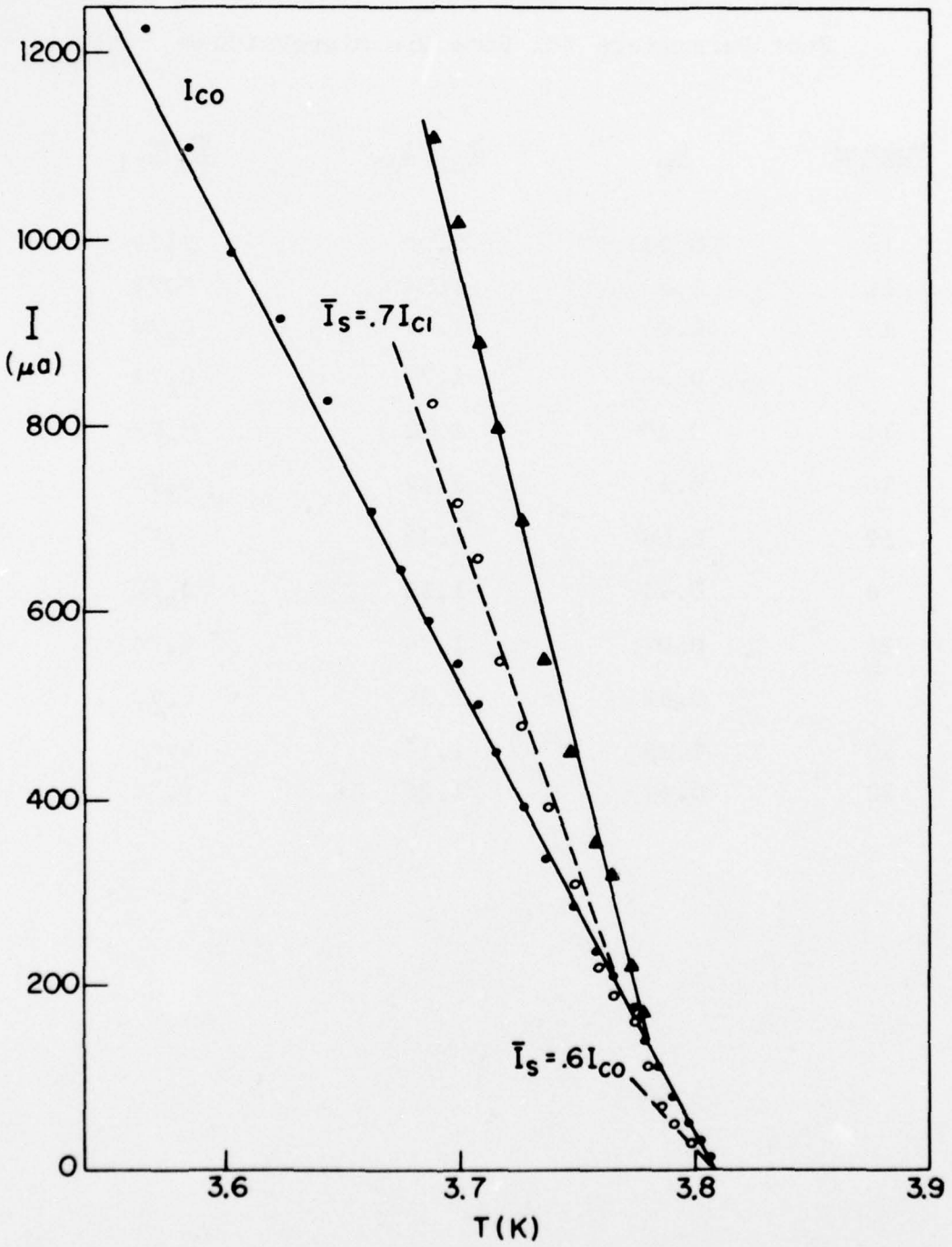

Fig. 4.15 Plots of the equilibrium critical current I_{co}, the excess supercurrent $\bar{I}_s$, the enhanced supercurrent I_{cl} as a function of temperature for bridge #3.

Table 4.1

Foot Parameters for Some Tin Microbridges

Number	R_N	I_{cl}/I_{co}	$\bar{I}_s/I_{cl}$
15	0.06	2.00	0.77
11	0.33	1.84	0.72
13	0.09	1.67	0.78
9	0.36	1.70	0.72
14	0.20	1.62	0.79
18	0.13	1.62	0.72
19	0.06	1.48	0.75
8	0.44	1.38	0.70
21	0.07	1.34	0.74
7	0.43	1.28	0.78
10	0.85	1.19	0.65
22	0.62	1.20	0.74

much smaller than that predicted for tin. This is due to the very long coherence length of aluminum which will tend to oppose changes in the order parameter different than the equilibrium case. In order to observe the supercurrent enhancement in aluminum, one would require microbridges with L/ξ ratios comparable to those of our tin microbridges. However, because of the longer inelastic scattering time of aluminum[66] the enhancement would appear at very low voltages where it might not be practical to observe it.

In the case of lead, which has a shorter scattering time, the transverse term might become comparable to the longitudinal one, but it is not presently feasible to fabricate bridges satisfying the condition $L < \xi(T)$ because of the shorter coherence length in lead. The I-V characteristics of a lead microbridge comparable in size to our tin microbridges is shown in Fig. 4.16. The I-V characteristics are quite different than those of tin. Near T_c, the curves show a change to the resistive state above I_{co} marked by a steep rise and a curve without inflection points, very similar to that observed in tin. However, as the temperature is lowered the characteristics are quite different. The features of the gap and subharmonic gap structure are not visible on the I-V, though a feature at the gap is seen if dI/dV is measured. At low voltages, where one would expect the foot to be observed (τ_2 is of order 10^{-11} seconds, so nonequilibrium effects should become important at voltages

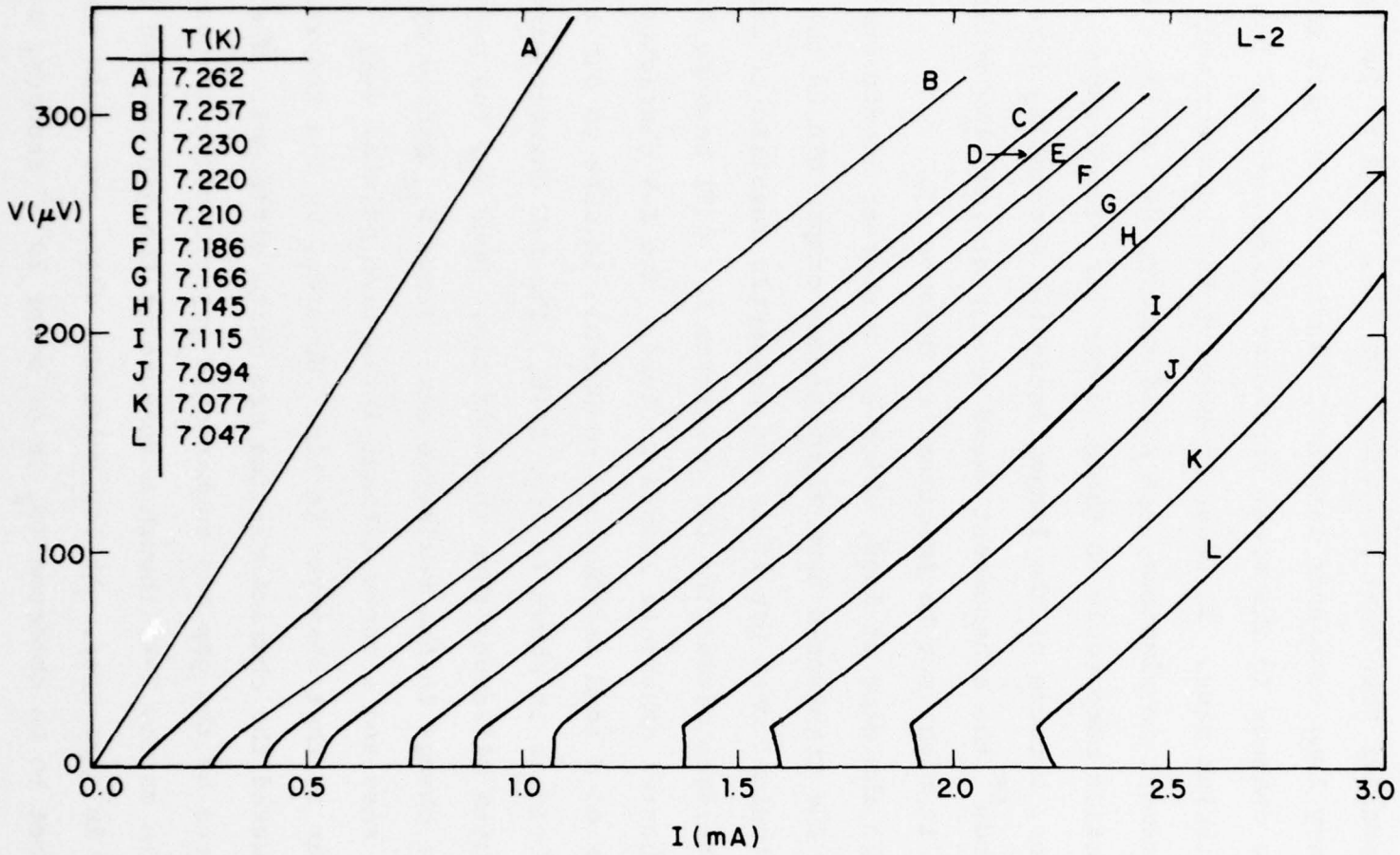

Fig. 4.16 I-V characteristics of a lead microbridge close to the critical temperature.

of order 50 μV), instead of a foot one observes a sharp rise up to a voltage of about 20 μV, followed by a region with an excess supercurrent $\overline{I}_s$ of order 0.8. The region below 20 μV becomes hysteretic very rapidly, and at lower temperatures the hysteresis becomes wider. These characteristics are not understood at present and it is clear that further work with high T_c materials will be required before a coherent understanding of the properties of these microbridges can be achieved. It might be that the I-V characteristics observed are due to flux-flow. While we believe our tin microbridges are too narrow to contain a single vortex, the same is not true of our lead bridges. However, these I-V characteristics are different than those predicted by Likharev[67] for flux-flow through a microbridge.

CHAPTER FIVE

HIGH-FREQUENCY PROPERTIES OF VARIABLE-THICKNESS MICROBRIDGES

The extreme sensitivity of Josephson devices to electromagnetic radiation suggests the possible application of these devices as detectors in the microwave and far-infrared regions of the spectrum. Among Josephson devices, thin film microbridges are especially attractive for practical applications because of their compatibility with thin-film technology for the fabrication of complex circuits as well as their small capacitance. However, the performance at high frequencies in two-dimensional thin-film microbridges is considerably inferior to that of point contact devices. Skocpol et al[4] had shown, when this work was initiated, that heating effects impose a limit on the voltage (and thus frequency) at which Josephson effects could be observed. In that analysis, the superiority of the point contact was suggested to be due to its three-dimensional geometry which more efficiently removes the heat generated in the weak link region. Therefore, the variable-thickness geometry should provide a system whose performance is closer to that of point contacts, since it should remove the heat, if not as efficiently as the point contact, at least more efficiently than in two-dimensional uniform thickness microbridges. In this chapter we describe the response of our variable-thickness

microbridges to microwave radiation. It is shown that the dramatic improvements in performance observed are due to their reduced self-heating. Furthermore, it is found that heating modifies the ac response of these devices, as well as determining their maximum frequency of operation. Heating effects are found to be sufficiently reduced in the variable-thickness geometry that they represent a promising configuration for microwave and far-infrared applications.

In Section 5.1 the experimental ac Josephson properties of our microbridges are presented. At low temperatures we observe ac Josephson steps to voltages as high as 3.7 mV in our best samples. This corresponds to frequencies of 2 THz and is a dramatic improvement over other thin film microbridges. Our experimental results led to a detailed heating model for high-frequency three-dimensional Josephson devices, which is presented in Section 5.2. The model predicts an exponential decrease of the critical current $I_{co} \approx e^{-P/P_o}$ where P is the power dissipated in the weak link region and P_o is a characteristic power level which is temperature and material dependent. We find these predictions of the model to be in excellent agreement with our experimental observations in tin and lead variable-thickness microbridges, as well as with those reported by other workers using different materials. At low voltages and near T_c the predictions of the model are found to be in good quali-

tative agreement with the observed cut-off of the oscillatory Bessel function power dependence of the ac steps as well as with the temperature dependence of their amplitude. This is discussed in section 5.2.5. From the model it is also possible to establish optimum design criteria for variable-thickness microbridges to be useful at high frequencies. This is discussed in section 5.2.6, where some preliminary results on the application of these criteria are presented. Finally, experimental evidence is presented in section 5.3 which clearly demonstrates the connection between performance, hysteresis, and heating. Here gap and subharmonic gap structure is used as a local thermometer of the temperature rise induced in the weak link by dissipation. The values of the gap obtained from the subharmonic gap structure extrapolated to zero dissipation are found to be in excellent agreement with the BCS theory.

5.1 The ac Josephson Effect and Variable-Thickness Microbridges

For the purposes of describing the ac response of our microbridges, it is useful to introduce the resistively-shunted junction (RSJ) model in which the total current flowing through the device is assumed to flow through an ideal Josephson element $I_{co} \sin \varphi_o$ shunted by a normal resistance R_N and a capacitance C:

$$I = I_{co} \sin \varphi_o + \frac{V}{R_N} + C \frac{dV}{dt} \qquad (5.1)$$

where φ_o is the total phase difference across the weak link. The phase difference grows in time with voltage according to the Josephson relation

$$\frac{d\varphi_o}{dt} = \frac{2eV}{\hbar} \tag{5.2}$$

Using Eq. (5.1) in (5.2) yields an oscillatory supercurrent component flowing through the weak link. While it is possible to detect directly the radiation emitted by the junction at $\omega_o = 2eV/\hbar$,[68,69] it is simpler to mix the internal oscillation of the junction with an external radiation field. Then the total voltage induced across the weak link will be $V = V_{dc} + V_{rf}\cos(\omega_{rf} t)$ (assuming an ideal voltage bias). When this is combined with Eq. (5.2), it yields a supercurrent component of the form

$$I_s = I_{co} \sum_{n=-\infty}^{\infty} J_n\left(\frac{2eV_{rf}}{\hbar\omega_{rf}}\right) \sin\left(\varphi_o + \left(\frac{2eV_{dc}}{\hbar} + n\,\omega_{rf}\right) t\right) \tag{5.3}$$

where φ_o is an arbitrary phase factor, and J_n is the Bessel function of order n. Equation (5.3) implies that whenever the Josephson oscillation frequency equals a harmonic of the frequency of the applied radiation, a dc beat will be observed in the I-V characteristics. The amplitude of this dc current beat is given by

$$I_n = I_{co} J_n \left(\frac{2eV_{rf}}{\hbar\omega_{rf}} \right) \qquad (5.4)$$

In practice, however, the junction is usually current-biased so that the observed behaviour differs from Eq. (5.4), and the ac-induced steps in the I-V characteristics have amplitudes proportional to distorted Bessel-functions as first determined by Russer.[70] The boundary between these two different behaviours is determined by the $I_{co}R_N$ product which allows the definition of a normalized frequency $\Omega = \frac{\hbar\omega_{rf}}{2eI_{co}R_N}$. For $\Omega > 1$ the resistive shunting will dominate and the step amplitudes will be given quite accurately by Eq. (5.4). For $\Omega < 1$ most of the ac current will flow through the Josephson element and the step amplitudes will correspond to distorted Bessel functions. In a similar manner Eq. (5.1) defines a characteristic frequency $1/R_NC$ above which the capacitive element dominates. However, this should be of little practical importance in variable-thickness microbridges because of their low capacitance estimated to be of the order 10^{-3}-10^{-2} pF.

The behaviour described by this model is readily observed in our variable-thickness microbridges. In Fig. 5.1 the response to 32 GHz microwave radiation of one of our tin microbridges is shown. At small microwave powers a step appears at 66 μV corresponding to the first harmonic of the

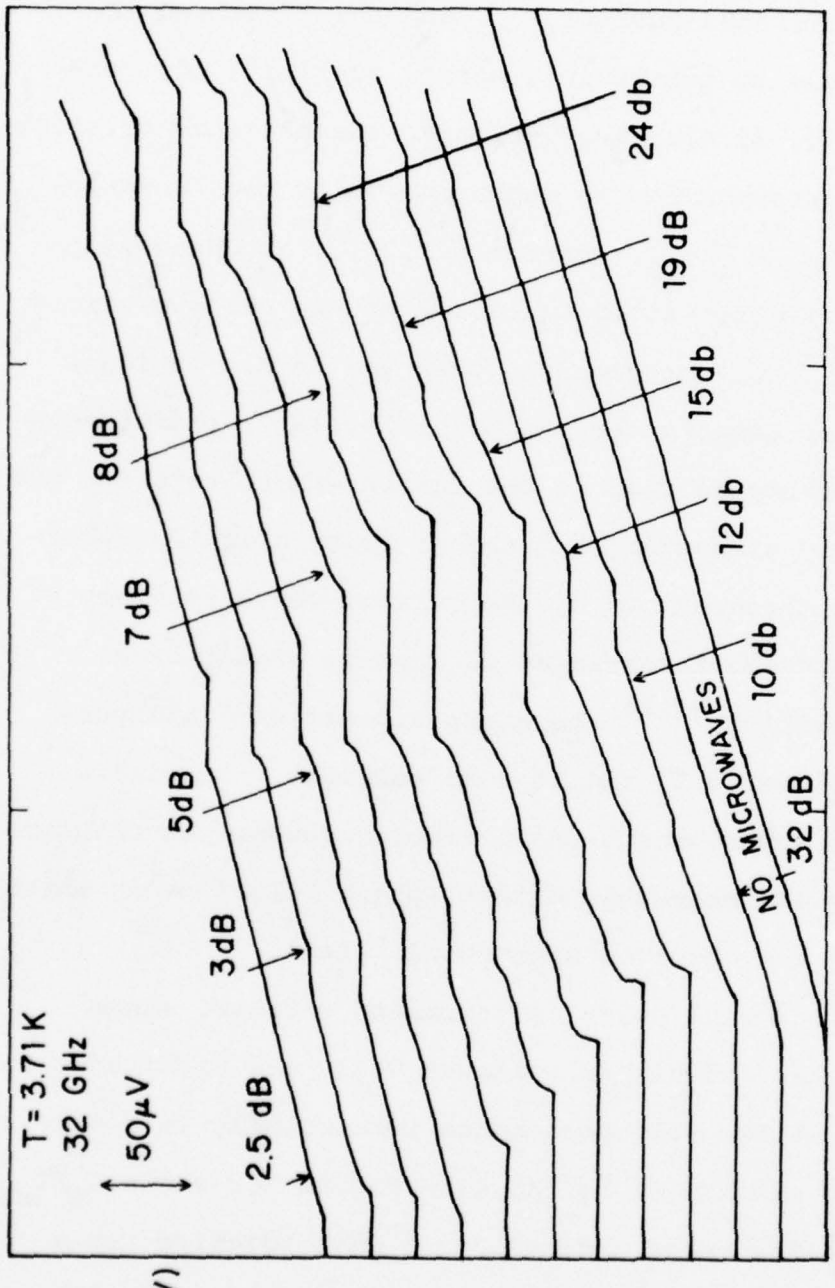

Fig. 5.1 Response of bridge #3 to 32 GHz radiation. The Josephson voltage corresponds to 66 μV.

applied radiation. As the microwave power is increased further, the critical current I_{co}, and the first and the second step seem to behave in a manner qualitatively consistent with Eq. (5.4). However, note the presence of steps at voltages corresponding to subharmonics of the fundamental frequency $\omega_o = \frac{n}{m} \omega_{rf}$, where m = 1,2,... . These steps are not predicted by either Eq. (5.4) or the current-biased RSJ model,[70,71] but are commonly observed in microbridges at a variety of temperature and power levels. Their observation is probably related to the current-phase relation not being perfectly sinusoidal but rather being slightly anharmonic. While measurements of the current-phase relation of variable-thickness microbridges do show an almost ideal sinusoidal relation,[20,21] these experiments were all performed very close to T_c and at zero voltages. At finite voltages, the supercurrent enhancement discussed in Chapter Four leads to an anharmonic current-phase relationship which would explain the observed subharmonic steps.

As the microwave power is increased further, steps appear at higher and higher voltages while the amplitudes of the ac steps at low voltages change periodically in a way qualitatively similar to Eq. (5.4). Figure 5.2 shows I_n/I_{co} for the first ten steps induced by 10 GHz radiation for a typical microbridge. While qualitatively this is similar to a Bessel function dependence, no amount of fitting of

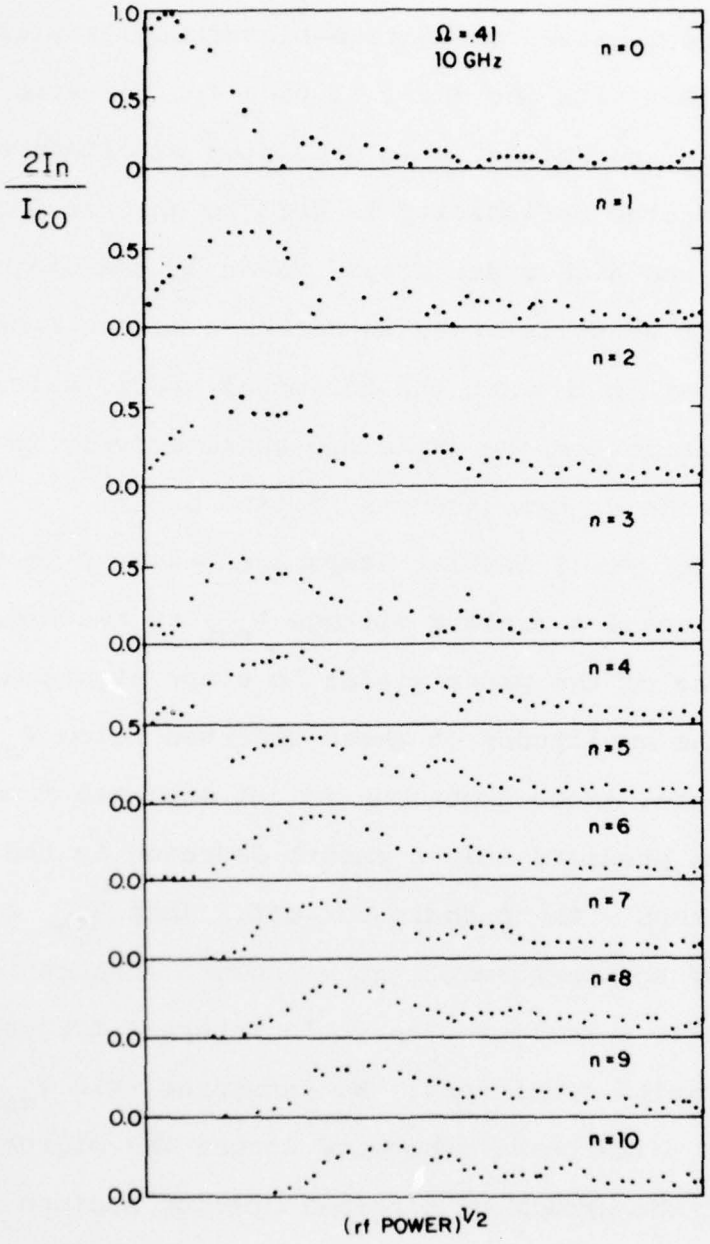

Fig. 5.2 Full step widths normalized to the critical current I_{co} for the first 10 steps at 10 GHz.

either the current-biased or voltage-biased models yields detailed agreement with the data. Typically, the step heights observed are smaller than predicted by either of these models and the periodicity is hard to observe for high powers or the high order steps. Near T_c the width of the low-order ac steps is found to decrease as one approaches T_c in disagreement with what the RSJ model predicts for $\Omega > 1$. These discrepancies can be explained qualitatively in terms of heating effects as discussed in Section 5.2.5.

At very high power levels, steps are observed to very high voltages, until a maximum voltage V_{max} is reached. Any further increase of the power yields no steps at higher voltages and the amplitudes of those observed below V_{max} begin to decrease. Such behaviour is not expected from Eq. (5.4) which predicts only a smooth decrease in the amplitudes of the steps with no sharp cut-off. This V_{max} is a useful index of the performance at microwave frequencies, as it corresponds to a maximum observable internal frequency under the operating conditions. We interpret this V_{max} as the voltage at which phase coherence across the microbridge is lost due to the growth of a normal hotspot because of the increased power dissipation. This interpretation will be appropriate only as long as the frequency of the applied radiation is well below the gap frequency at the operating temperature. At higher fundamental frequencies, effects

due to the Riedel peak and subsequent roll-off in the intrinsic frequency dependence of the supercurrent might also be of importance.[71,73] At microwave frequencies and away from T_c these roll-off and peak effects can be neglected in our microbridges because $\hbar\omega \ll 2\Delta$ so that V_{max} should only be limited by heating effects.

The interpretation of V_{max} as reflecting a heating limit in superconducting microbridges has been confirmed experimentally. Improvements of V_{max} as a result of using the variable-thickness geometry have been reported by Klapwijk and Mooij[74] and Klapwijk and Veenstra.[49] Using a mechanical scribing machine they produced aluminum variable-thickness microbridges with $V_{max} = 0.75$ mV at $T/T_c = 0.93$. This represented a considerable improvement over their uniform thickness microbridges where the ac steps were not observed even at low voltages. Similarly their tin variable-thickness microbridges showed steps up to $V_{max} = 1.2$ mV at very low temperatures.

Even greater improvements are observed in our microbridges. In Table 5.1 we present data from a representative selection of our microbridges. The first group in the table consists of microbridges with low impedances and fairly large critical currents. Within this group the bank thickness varies from 0.1 μm (a uniform-thickness bridge) to 3.0 μm in the variable-thickness geometry. There is a clearcut

Table 5.1

Some Characteristic Properties of
Representative Tin Microbridges

#	R (Ω)	I_{co} (2.1 k) (ma)	Banks (μm)	Width (μm)	V_{max} (mV)
1	0.15	22.0	0.1	1.5	0.30
2	0.08	10.0	1.0	0.5-1.0	0.63
3	0.13	12.5	1.0	0.5	0.98+
4	0.24	11.3	3.0	~ 1.0	1.47+
5	0.27	17.3	3.0	~ 1.0	1.37+
6	0.40	3.5	0.1	0.5	0.70
7	0.43	3.8	1.0	~ 0.5	1.67
8	0.44	7.5	1.0	< 0.5	1.33+
9	0.36	2.5	1.0	< 0.5	2.27
10	0.85	1.9	1.0	< 0.5	2.64
11	0.33	4.0	1.7	< 0.5	3.70+

+ Indicates that observation corresponded to maximum power available but the limit for the bridge had not been reached.

improvement in V_{max} for the thickest banks, of almost a factor of five. The second group is more representative of the bridges made in the later stages of our work during which the fabrication technique and the burnout problem were better controlled. All of the bridges in this second group have higher resistances, smaller critical currents and narrower widths ($w \lesssim 0.5$ μm). Once again an improvement of almost a factor of five from the uniform-thickness bridge with 0.1 μm thick banks to the variable-thickness bridge with thickest bank and highest resistance is observed. Within each group a considerable difference in performance between high and low resistance microbridges is observed. This is easily understood since the observation of ac steps at V_{max} requires that the bias voltage and the microwave voltage be of order V_{max} so that the power dissipated in the weak link scales as V_{max}^2/R_N giving more dissipation in the low impedance bridges.

In Table 5.2 we show the values of V_{max} for our lead variable-thickness microbridges, all of which had the same bank thickness $d = 1.5$ μm. The voltage limits found are not too different from those in tin; although the highest value of V_{max} in lead is below that in tin, the number of lead samples studied was much smaller. Note however, that except for the microbridge with $R_N = 10$ ohms, which showed no ac steps, the bridge with the best performance had the highest resistance.

Table 5.2

Some Characteristic Properties of Lead Microbridges

Number	R_N (Ω)	I_{co} (4.2K) (mA)	V_{max} (mV)
L-6	0.07	16.8	1.6
L-4	0.08	37.5	1.8
L-5	0.08	20.5	1.8
L-8	0.10	4.1	1.1
L-2	0.16	33.6	1.9
L-3	0.60	3.5	1.8
L-1	0.80	1.9	3.0
L-7	10.00	0.042	No steps

From the above results, one obvious possibility is to use thicker and thicker banks and smaller microbridges in order to reduce heating effects further. However, the cutting of ever smaller bridges with ever thicker banks is increasingly difficult. It was found that with a bank thickness > 1.5 μm the yield of good microbridges was significantly reduced since the edge of the diamond knife did not penetrate uniformly. Thus a bank thickness of 1.5 μm was selected as a compromise between good yield and good cooling. The problem of increasing bank thickness is not restricted to our crude fabrication technique. In more sophisticated techniques using electron-resists, the bank thickness is limited by the resist thickness (~ 1.0 μm), so that any further increase in the bank thickness requires the use of many-stage deposition.

Thus, the observed experimental behaviour is consistent with heating determining the high frequency performance of thin film microbridges in general. In the next section further implications of heating are explored within the framework of a simple heating model for the case of three-dimensional metallic cooling appropriate to the variable-thickness geometry.

5.2 The Heating Model

5.2.1 Introduction

The increased dissipation as the voltage and the rf power are increased produces a gross disequilibrium inside the small weak link. One can approximate this situation by defining a local temperature distribution inside the weak link. Earlier analysis of this problem[4] showed that in a two-dimensional system V_{max} should scale roughly as the energy gap $2\Delta/e$ and in three dimensional systems it should scale approximately as $(2\Delta/e)(\bar{\xi}/a)^{\frac{1}{2}}$ where $\bar{\xi}$ is the coherence length averaged over the temperature distribution inside the link, and a is the neck radius. The analysis presented in this section extends the previous analysis for the three-dimensional geometry by using the collinear cone geometry introduced in Chapter Three.

In the presence of a current I the total amount of power dissipated inside the weak link is given by I^2R. The power dissipation will not all occur at the center of the weak link but rather will be a function of radius r. The temperature gradient required to carry the power away from the center of the weak link is given by

$$\frac{dT}{dr} = \frac{P(r)}{\Omega K_{eff} r^2} \qquad (5.5)$$

where K_{eff} is the thermal conductivity as modified by

boundary scattering. This corresponds to a position dependent resistivity as discussed in section 3.2.1.

The power dissipated inside a radius r is given by

$$P(r) = \frac{I^2}{\Omega} \int_{r_1}^{r} \frac{\rho_{eff}}{r^2}\, dr = \frac{I^2 \rho_o}{\Omega} \left[\left(\frac{1}{r_1} - \frac{1}{r}\right) + \frac{\ell}{4\sin\theta}\left(\frac{1}{r_1^2} - \frac{1}{r^2}\right)\right] \tag{5.6}$$

where we have assumed the validity of the Wiedemann-Franz law and $\rho_{eff} = \rho_o\ (1 + \ell/2r\ \sin\theta)$ as obtained in Chapter Three. Integrating Eq. (5.5) from $r = \infty$ to r we obtain

$$T^2(r) - T_b^2 = \frac{3e^2\rho_o I^2 R_N}{2\pi^2 k^2 \Omega r}\left(1 + \frac{\rho_{eff}(r)}{\rho_o}\right)\left[1 - \frac{r_1(\rho_o + \rho_{eff}(r))}{2r(\rho_o + \rho_{eff}(r_1))}\right] \tag{5.7}$$

From Eq. (5.7) the maximum temperature in the middle of the weak link is for $\ell << r_1\sin\theta$

$$T_m = T(r_1) = \left[T_b^2 + 3\left(\frac{eV}{2\pi k}\right)^2\right]^{\frac{1}{2}} \tag{5.8}$$

This is a very general result valid for all three-dimensional geometries.[75,76] Furthermore, all material properties have dropped out.

From Eq. (5.8) one can estimate the temperature rise produced by the dc voltage and the microwave radiation in our

variable-thickness microbridges. For useful response V_{rf} should be of order V_{dc} so that the total power dissipated is $V_{rms} = (V_{dc}^2 + 0.5\ V_{rf}^2)^{\frac{1}{2}}$. For the microbridge with the best performance in Table 5.1, $V_{max} = 3.7$ mV and $T_b = 2.1$ K which yields a maximum temperature in the weak link of 15 K. Thus the departures from equilibrium are fairly large at the operating voltages of interest. From Eq. (5.8) the voltage necessary to raise the temperature in the middle of the bridge above T_c is

$$V = 0.312\ T_c\left(1 - \frac{T_b^2}{T_c^2}\right)\ (\text{mV}) \qquad (5.9)$$

At $T_b = 0$ a voltage $V \sim 1.2$ mV is required to raise the temperature of a tin bridge above T_c. This voltage will be larger in materials with high T_c and smaller at temperatures closer to T_c.

It is important to note that one effect of these large temperature rises in the weak link is to add additional noise due to the hot electrons present in the weak link. If one assumes the weak link is a series of Johnson noise sources it can be shown that the noise temperature is given approximately by[10]

$$T_n = \frac{1}{2}\ (T_b + T_m)\ . \qquad (5.10)$$

5.2.2 Reduction of I_{co} by Heating

The Aslamazov and Larkin model introduced in section 3.2.1 can be used to take heating into account for the calculation of the critical current in the presence of dissipation. In Eq. (3.1) the order parameter in the weak link was found to be of the form

$$\Psi = \Psi_o \left[f(\vec{r}) + (1 - f(\vec{r}))e^{i\varphi_o} \right] \tag{5.11}$$

In the presence of a voltage this corresponds to the oscillating order parameter shown in Chapter Four. In the presence of dissipation Ψ will still oscillate, but, because of heating, the order parameter will have a maximum which is below that given by (5.11). One can write Eq. (4.11) in a more general form to include heating

$$\Psi = \Psi_o \left[f(\vec{r}) + f(-\vec{r})\, e^{i\varphi_o} \right] \tag{5.12}$$

The total supercurrent flowing through the weak link is now

$$\vec{J}_s = \frac{e^* \hbar}{m^*} |\Psi_o|^2 \left[f(-\vec{r})\vec{\nabla} f(\vec{r}) - f(\vec{r})\vec{\nabla} f(-\vec{r}) \right] \sin\varphi_o \tag{5.13}$$

where in the absence of heating the factor in parenthesis reduces to ∇f. In the middle of the bridge this factor reduces to $2f(0)\, \nabla f(0)$. In the presence of heating $f(0)$ will be depressed below 1/2 so that $|\Psi|^2$ will be depressed

to $|2f(0)\Psi_o|^2$. Since $\nabla f(0)/f(0)$ remains approximately the same, of order $\sim (4/\pi a)\tan(\theta/2)$, in the collinear cone geometry, in the presence of heating I_{co} will be reduced in proportion to $|f(0)|^2$.

In the case of large dissipation which is of interest here, the middle of the weak link is above its transition temperature and one has to estimate the ability of the pairs to penetrate across this normal barrier. One can use the Ginzburg-Landau equation

$$-\frac{\hbar^2}{2m^*}\nabla^2\Psi + \alpha\Psi + \beta|\Psi|^2\Psi = 0 \qquad (5.14)$$

In the normal region the order parameter is very small and the nonlinear term in Eq. (5.14) can be dropped. The radial equation for (5.14) is

$$\frac{d^2(r\Psi)}{dr^2} = \frac{2m^*}{\hbar^2}\alpha(T(r))\,(r\Psi) = \frac{1}{\xi^2(r)}\,(r\Psi) \qquad (5.15)$$

where now the coherence length $\xi(T)$ is a position dependent quantity because of the large temperature gradients at either side of the weak link. Then

$$\xi^{-2}(r) = \xi^{-2}(0)\,[t(r) - 1] \qquad (5.16)$$

inside of the normal region. In order to estimate how Ψ is attenuated in this normal region we use the WKB approximation

which, from the leading term, gives an attenuation factor for r^{Ψ}

$$2f(0) = \exp(-W) \tag{5.17}$$

where

$$W = \frac{1}{\xi(0)} \int_{r_1}^{r(T_c)} [t(r) - 1]^{\frac{1}{2}} \, dr \, . \tag{5.18}$$

This integral can be written in terms of the average integrand as

$$W = \frac{r(T_c) - r_1}{\xi(0)} \left\langle [t(r) - 1]^{\frac{1}{2}} \right\rangle_{AVE.} \tag{5.19}$$

Notice that Eq. (5.19) involves simply $1/\xi$ averaged over the temperature profile in the normal region. For high powers, $r(T_c)$ is given by Eq. (5.7) and is much larger than r_1, a, ℓ and ξ_o so that all terms in (5.7) of order $\ell/r(T_c)$ and $r_1/r(T_c)$ can be neglected. Furthermore, the average in Eq. (5.19) can be replaced to a good approximation by its value in the middle of the range of r

$$W = \frac{r(T_c)}{\xi(0)} \left\{ t[\tfrac{1}{2} r(T_c)] - 1 \right\}^{\frac{1}{2}} \tag{5.20}$$

From Eq. (5.7)

$$T^2(r) - T_b^2 = \frac{3 e^2 \rho_o P}{\pi^2 k \Omega r} \tag{5.21}$$

from which the value of $r(T_c)$ is

$$r(T_c) = \frac{3\, e^2 \rho_o}{\pi^2 k^2\, \Omega} \quad \frac{P}{T_c^2 (1 - t_b^2)} \tag{5.22}$$

Since $t[\frac{1}{2}\, r(T_c)] = (2 - t_b^2)^{\frac{1}{2}}$, so that $\{t[\frac{1}{2}\, r(T_c)] - 1\}^{\frac{1}{2}} = [\frac{1}{2}(1 - t_b^2)]^{\frac{1}{2}}$, then

$$W = \frac{1}{[2(1 - t_b^2)]^{\frac{1}{2}}}\ \frac{3}{\pi^2}\ \frac{e^2}{k^2}\ \frac{\rho_o P}{T_c^2\, \xi(0)\Omega} \tag{5.23}$$

Since I_{co} is expected to decrease as $|2f(0)|^2 = \exp(-2W)$, then the effect of heating will be to decrease the critical current as

$$I_{co}(P) = I_{co}(P = 0)\, \exp(-P/P_o) \tag{5.24}$$

where

$$P_o(T) = \frac{1}{\sqrt{2}}\, (1 - t_b^2)^{\frac{1}{2}}\, K(T_c) T_c\, \xi(0)\Omega \tag{5.25}$$

$P_o(T)$ is a <u>temperature-dependent</u> characteristic power level which is geometry and material dependent. While this form was obtained for high power levels it can be shown[10] that the form for the decrease of the critical current at low power levels is essentially the same. The temperature dependence in Eq. (5.25) reflects the higher power required to raise the temperature of the weak link above T_c as the

temperature is reduced below T_c. The material dependence, which scales as $T_c^2 \xi(0)/\rho_o$, reflects the ability of the material to remove the heat as well as its ability to maintain phase coherence through its coherence length. Materials with high resistivity tend to have short coherence lengths. This can be balanced by a higher T_c so that at the same bath temperature more power will be required for a higher T_c bridge to be driven normal. At <u>low temperatures</u> assuming a residual resistance ratio of 10, $T_c^2 \xi(0)/\rho_o$ is approximately the same for Al, In, Sn, and Nb. It is much smaller in higher T_c materials because their short coherence lengths and high resistivity more than offset the advantage of their higher T_c's. Assuming $t_b = 0$ and a cooling solid angle of π for these materials, $P_o \approx 10$ μW. Thus, from this characteristic power level, it would require approximately 50 μW in order to reduce the critical current to 1% of its equilibrium value.

One must be careful in assessing these results. From our assumptions Nb would appear to be favored because its higher resistivity would yield higher resistance microbridges with equivalent P_o. However, while this would be true of bulk niobium, it is apparently not possible to make clean thin films of niobium, so the actual values of P_o would be considerably below 10 μW.

5.2.3 The Variable-Thickness Geometry

In the preceeding discussions we have assumed that the

collinear cone geometry is a good approximation to the variable-thickness geometry. While this is true, it is also important to consider the case of a finite bridge length L which is attached to very thick banks which are approximated by the collinear cone geometry. In this manner it is possible to assess the importance of the finite bridge length as well as to evaluate the performance of long variable-thickness microbridges where the simple radial cooling approximation breaks down. For very large power levels it is possible to approximate the bridge contribution by simply assuming the whole bridge is at the maximum temperature T_m. This establishes an upper bound to the additional contribution to the WKB exponent from the finite length of the bridge. Then from Eq. (5.17) this additional contribution is

$$W_{bridge} = \frac{L}{2\xi(0)} (t_m - 1)^{\frac{1}{2}} \tag{5.26}$$

where $t_m = T_m/T_c$. The critical current is reduced by

$$I_{co}(P) = I_{co}(P = 0)e^{-2W_{radial}-2W_{bridge}} \tag{5.27}$$

where W_{radial} is given by Eq. (5.23). Note that the bridge contribution is essentially what one expects for the reduction of the critical current in an S-N-S junction with coherence length $\xi(t_m)$.

At high voltages and low temperatures it is possible to estimate the relative contributions of W_{radial} and W_{bridge}. From Eqs. (5.8) and (5.26)

$$2W_{bridge} \lesssim \frac{L3^{\frac{1}{4}}}{\xi(0)2^{\frac{1}{2}}} \left(\frac{eV}{\pi kT_c}\right)^{\frac{1}{2}} \tag{5.28}$$

and from Eq. (5.23)

$$2W_{radial} = \frac{4_1 3}{\xi(0)2^{\frac{1}{2}}} \left(\frac{eV}{\pi kT_c}\right)^{2} \tag{5.29}$$

Their ratio is

$$\frac{W_{radial}}{W_{bridge}} = \frac{3^{3/4} r_1}{L} \left(\frac{eV}{\pi kT_c}\right)^{3/2} \tag{5.30}$$

At high voltages $eV/\pi kT_c \sim 5$ for our tin microbridges and 2.5 for lead so the bridge contribution will be important if $L \gtrsim 12\ r_1$ in tin and $L \geq 5\ r_1$ in lead. While in tin this contribution should not be important (recall $r_1 \sim 0.04\ \mu m$), in lead microbridges and other high T_c materials it can be important. At low voltages and near T_c, W_{bridge} is more important than given by Eq. (5.30); however, the nature of the approximations made and the uncertainty of the length L make it rather difficult to make quantitative comparisons with the model.

5.2.4 Voltage Limit for Microwave Induced Steps: Temperature and Material Dependence

The effect of dissipation is to reduce the critical current; this in turn reduces the widths of the ac steps observed. At high voltages this sets a limit for the observability of the ac steps, which can be compared to our data. In Section 5.1 we found the best performance in a bridge with $R_N = 0.33$ ohm, for which $V_{max} = 3.7$ mV. Using Eq. (5.8) this corresponds to $T_m = 15$ K. The total power dissipated in the bridge is 62 μW, so that if $P_o \sim 10$ μW the critical current is reduced to less than 1% of its original value. This is sufficient to reduce the height of the step below detectability.

A better way to compare the model with the data is to examine the power dependence of the ac steps in detail. In Fig. 5.3(c) we show the experimental data for dI/dV vs. V for the same bridge with $V_{max} = 3.7$ mV. Each of the equally spaced lines corresponds to an individual step, and the derivative is proportional to the step amplitude. At voltages of order 2.5 mV a striking periodicity develops in the step amplitudes. In Fig. 5.3(a) we plot the amplitude of the Bessel function for the case $P_o = \infty$ (perfect cooling). The same periodicity observed in the experimental data occurs at high n for $J_n(x)$. In Figs. 5.3(b), (d) and (e) we plot the same Bessel function but now its amplitude is affected

Figure 5.3. Step amplitudes at 10 GHz for different values of P_o compared with the experimental amplitudes for tin bridge #11.

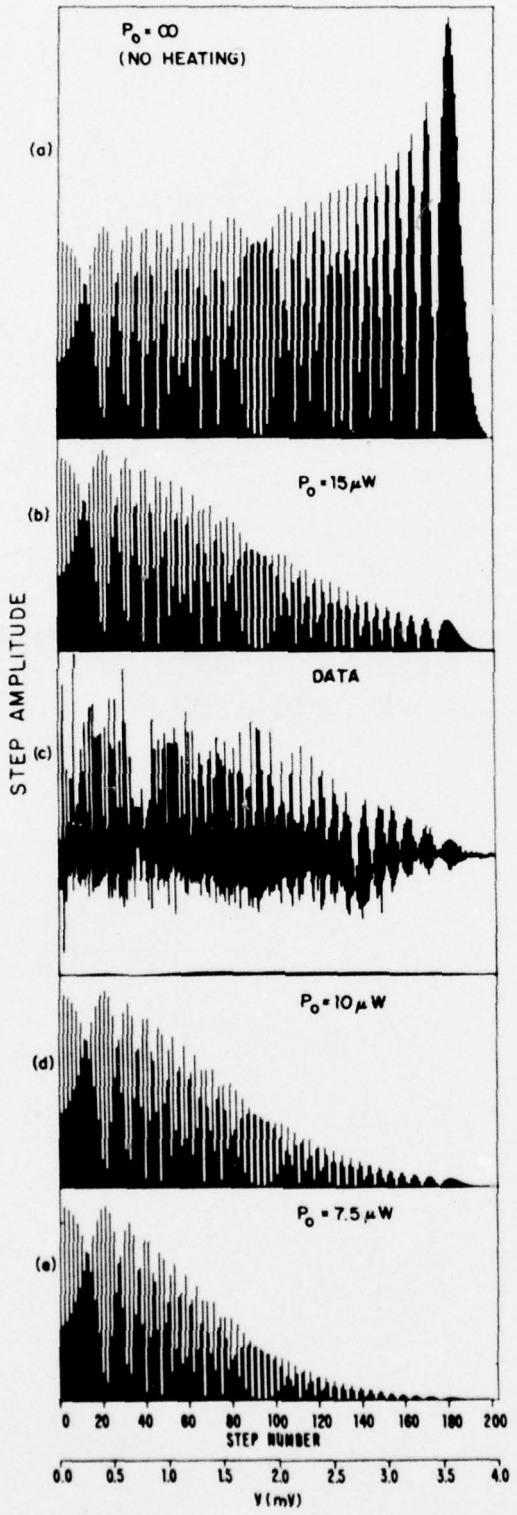
$P_0 = \infty$
(NO HEATING)
(a)
$P_0 = 15\mu W$
(b)
DATA
(c)
$P_0 = 10\mu W$
(d)
$P_0 = 7.5\mu W$
(e)
STEP AMPLITUDE
0 20 40 60 80 100 120 140 160 180 200
STEP NUMBER
0.0 0.5 1.0 1.5 2.0 2.5 3.0 3.5 4.0
V (mV)

by heating as P_o is decreased. As the voltage is increased the step width amplitudes decrease in a manner consistent with the data. The best fit for P_o appears to be somewhere between 10-15 μW. This value of P_o is in very good agreement with the heating model presented above, given the many approximations and assumptions made.

In Section 5.1 we discussed the power dependence of the ac steps and established that for $\Omega = (h\omega/2eI_{co}R_N) > 1$ the step amplitudes should behave like Bessel functions. Since at high powers I_{co} is considerably reduced below its P = 0 value it is valid to compare the amplitudes of the ac steps to Bessel functions. At lower voltages (hence powers) this breaks down as the normalized frequency $\Omega < 1$, and comparison should be made to the distorted Bessel functions of Russer.[70] All in all, the agreement at high voltages is a remarkable confirmation of the Bessel function dependence of the amplitude of the ac steps to the highest order reported to date.

While the observed data is in very good agreement with the predictions of the model, it is important to consider a criterion for the observation of the ac steps. Our low impedance microbridges have large critical currents. However, as the dissipation scales as V^2/R_N these critical currents decrease significantly with power and the ac steps become very small. A reasonable assumption based on the work of

Ambegaokar and Halperin[77] and Stephen[78] is that the n^{th} step in the absence of noise should exceed $ekT_N/\hbar$, where T_N is the noise temperature. Since $J_n(x)$ oscillates with an amplitude $\sim x^{\frac{1}{2}}$ until it reaches a maximum at $n \approx x$, as shown in Fig. 5.3(a), the most favorable amplitude of the rf power is that for which $x = n$, in which case J_n has a maximum $\pi/2n^{\frac{1}{2}} = \frac{1}{2}\pi(\hbar\omega_{rf}/2eV_{dc})^{\frac{1}{2}}$. The increased dissipation in the weak link raises the effective noise temperature $T_N = \frac{1}{2}(T_b + T_m)$. All these requirements give

$$I_{co}(P) = I_{co}(P = 0)e^{-P/P_o} \gtrsim \frac{ekT_N}{\hbar J_n}$$

$$\geq \frac{ek}{\pi\hbar}\left(\frac{2eV_{dc}}{\hbar\omega_{rf}}\right)^{\frac{1}{2}} \left\{ T_b + \left[T_b^2 + 3\left(\frac{eV}{2\pi K}\right)\right]^{\frac{1}{2}} \right\} \tag{5.31}$$

Since $P \approx 1.5\ V_{dc}^2/R_N$, for a given value of R_N, P_o, T_c and ω_{rf}. Eq. (5.31) gives the best value of V_{max} for these parameters. While in Eq. (5.31) one could use the value of $I_{co}(P = 0)$ predicted by theory, experimental values are usually higher and it is better to use the actual experimental value. Note the weak frequency dependence of Eq. (5.31). Experimentally we find the same value of $V_{max}(T)$ for 10 and 32 GHz, except in a very narrow range near T_c.

One can use Eq. (5.31) to calculate experimental values of P_o at each temperature, from the *measured* V_{max} values.

This is shown in Fig. 5.4 for one of our good performance microbridges in which P_o at low temperatures is expected to be determined exclusively by the radial contribution to the decrease of the critical current. The overall agreement between experimental data and the temperature dependence of the heating model fitted at the lowest temperature is excellent. Very near T_c, the experimentally determined P_o deviates below the model in a consistent way. This behaviour is observed in all of our high performance tin microbridges and we attribute it to the bridge contribution Eq. (5.26) becoming more important near T_c as predicted by the model. While the calculation for W_{bridge} is only approximate and represents an upper limit and the deviations from the model are small, it is nevertheless interesting to use the experimental data to attempt to obtain an estimate of the length required for W_{bridge} to yield the observed results. If the bridge contribution becomes important, rather than measuring P_o from Eq. (5.31) we measure the decrease of the critical current as $e^{-P/P_{o,eff}}$ where

$$P_{o,eff} \approx \frac{P_o}{1+\frac{W_{bridge}}{W_{radial}}} \qquad (5.32)$$

From the experimental data $P_o/P_{o,eff} \sim 1.5$ near T_c so $W_{bridge}/W_{radial} \sim 0.5$. A typical V_{max} at $T/T_c \sim 0.97$ is 1 mV which yields $t_m = 1.43$ and an effective length $L \sim 0.25$ μm.

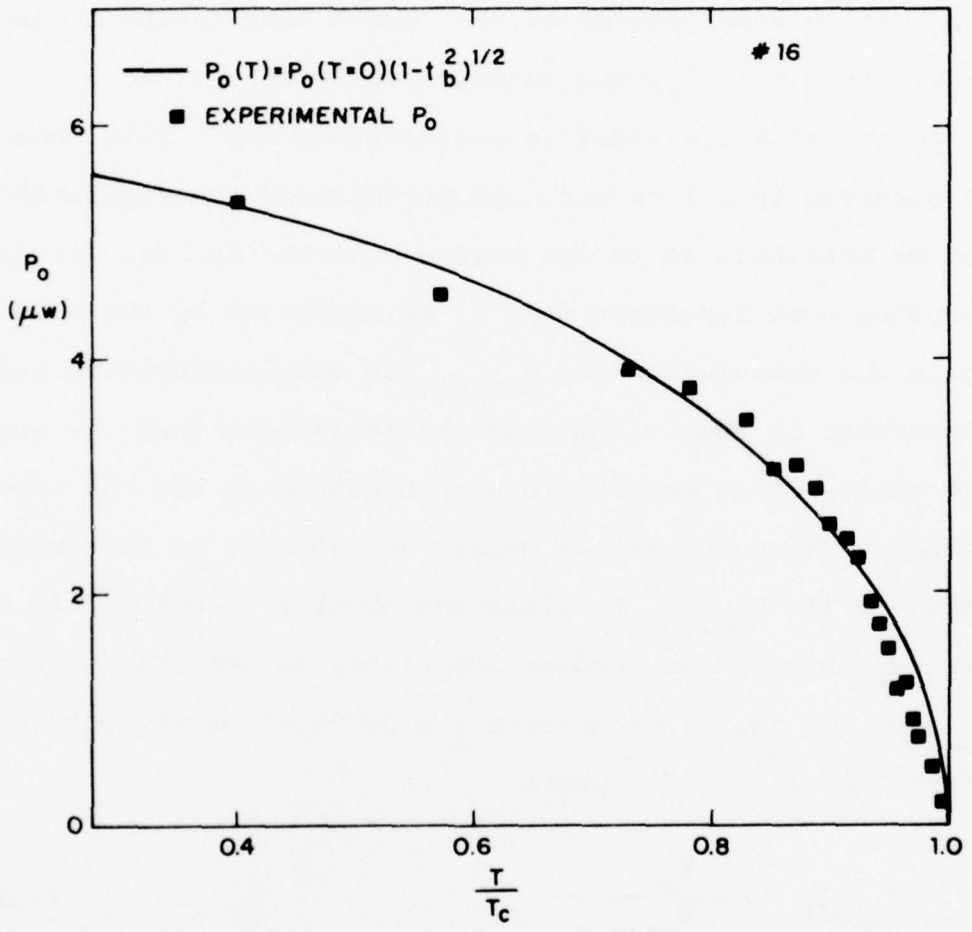

Fig. 5.4 Temperature dependence of $P_o(T)$ for a high performance microbridge (bridge #16).

Thus, the collinear cone approximation is indeed a good approximation as this length is smaller than that measured from SEM pictures of our microbridges. One should be careful however as this is only an approximate value for L because of the approximations involved in the calculation. This length is a factor of 3 smaller than that obtained in Chapter Four for a good fit to the effective resistance of the foot region. This discrepancy is of no concern as the nature of the two lengths is quite different. The length measured in Chapter Four is the length required for the order parameter in the bridge to reach the value of the order parameter in the banks. In the present case, the effective length measures the contribution from the length of the bridge which is not contained in the collinear cone approximation. From the SEM pictures shown in Chapter Two, it is clear that the collinear cone geometry would approximate at least part of the bridge.

One important conclusion of the above analysis is that for high T_c materials the contributions from the bridge will be even more important than in tin for comparable size microbridges. In Table 5.3, the best values of V_{max} and $P_o(T = 0)$ obtained from Eq. (5.25), extrapolating to $T = 0$, are shown for variable-thickness microbridges made of different materials. These values can be considered to be in good agreement with the model. The values for the lead microbridge are below that of tin; however, the zero temperature coherence length

Table 5.3

Parameters For The Best Performance Obtained in Variable-Thickness Microbridges of Different Materials

Material	T/T_c	V_{Max} (mV)	$P_o(T=0)$ (μW)
Tin	0.54	3.7	8.1
Lead	0.28	3.0	5.9
Niobium	0.94	0.45	1.0
Aluminum	0.92	0.97	0.62

$\xi(0)$ is almost a factor of two smaller in lead than in tin so that the contributions from the finite length of the bridge are more important. The niobium result corresponds to a fairly long ($\sim$ 1 μm) variable-thickness bridge made of very dirty niobium[78] so that both the thermal conductivity K and $\xi(0)$ are very small. The low values of P_o obtained by Klapwijk and Mooij[79] in aluminum variable-thickness microbridges are harder to interpret. The values are considerably below those predicted by the model, but no systematic search for the largest V_{max} was made. The value given in the table corresponds to a bridge with R_N = 0.85 ohms at a bath temperature of 1.07 K (T_c = 1.16). At the microwave power at which the measurement was made the width of the step was 5 μA, which is 4% of the zero dissipation critical current. The frequency used was 35 GHz so V_{max} = 0.965 mV corresponds to the 13th step. The Bessel function $J_{13}(x)$ has a maximum of order 0.3, for which the step width observed is 16% of the maximum width expected in the absence of dissipation. This is a sizable step and it suggests that more steps could have been observed with this sample. It should be noted that their tin microbridges of comparable size to their aluminum microbridges showed steps to relatively high voltages although they had values of V_{max} below those obtained in this work. While these explanations seem plausible, without further experimental work it can not be confirmed.

The results of the model can also be used to estimate

V_{max} for the Nb point contacts of McDonald et al.[80] For a typical resistance of $R_N \sim 10$ ohms V_{max} is estimated to be of the order of 16 mV, compared to 17 mV observed experimentally. This agreement is quite good, the superior performance of the point contact arising from its smaller size and hence larger resistance. Furthermore, the niobium points were made of bulk niobium wires with long mean free paths and thus good thermal conductivity compared to the dirty niobium films.

5.2.5 Heating Effects at Low Voltages

While we have been primarily interested in the high voltage limits for the observation of ac Josephson steps, heating effects can also significantly modify the ac steps at low voltages near the critical temperature. This is simply a consequence of the small power levels required near T_c to raise the temperature of the bridge above its critical temperature. In terms of the heating model it can be said to be a consequence of the small value of P_o near T_c.

Near T_c quantitative comparisons with the heating model become rather difficult because of the uncertainty of the bridge contribution to the decrease of the critical current. Furthermore, one has to assume a particular dependence of the widths of the ac steps on power in the absence of heating effects. In Fig. 5.5 we plot the maximum full-width of the first ac step I_1^{max} normalized by the zero power critical current I_{co} against the normalized frequency Ω. The data

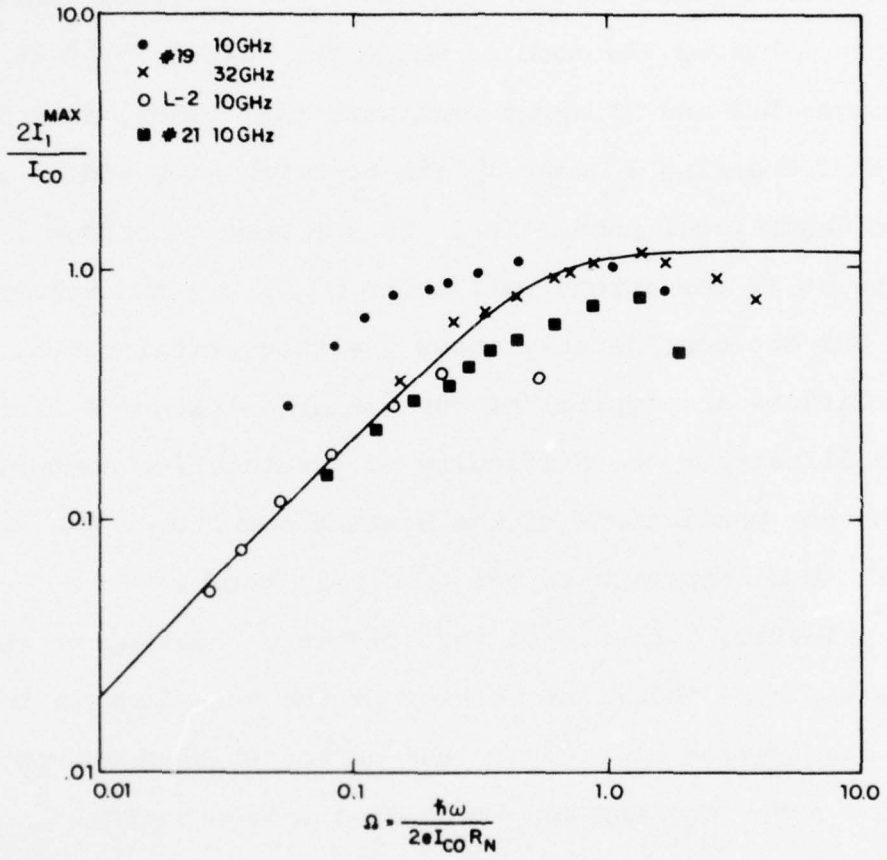

Fig. 5.5 Experimental values of the maximum width of the first Josephson step as a function of the normalized frequency. The solid line corresponds to the predictions of the current-biased RSJ model.

were taken on a tin and a lead microbridge at 10 GHz and on a second tin microbridge at both 10 and 32 GHz. The solid line corresponds to the value of I_1^{max}/I_{co} predicted by the current-biased RSJ model. While the values for $\Omega \ll 1$ for bridges L-2 and 21 agree well with this model, as Ω increases with decreasing I_c near T_c the observed step widths are below the theoretical prediction. In the case of bridge 19 the data at 32 GHz agrees well up to $\Omega \sim 1$ but the values at 10 GHz are considerably above the theoretical curve. These variations are typical of our variable-thickness microbridges and illustrate the difficulty of quantitative comparisons with any predictions of the heating model when the behaviour with no dissipation is not precisely known.

In Fig. 5.6 we show the effects of heating on the maximum width of the first ac step if the behaviour in the absence of dissipation is given by the current-biased RSJ model. The curve $\alpha = 0$ corresponds to no dissipation where $\alpha = 1.5\ V_{dc}^2/R_N P_o(T = 0)$. Since V_{dc} corresponds to the voltage at which the first step is observed; these effects are strongly dependent on frequency. The trends in Fig. 5.6 are qualitatively similar to those obtained in the experiment. Besides the difficulties noted previously, quantitative comparisons are difficult because the actual dissipation is not necessarily equal to V^2/R_N, to an extent which depends on the normalized frequency Ω.

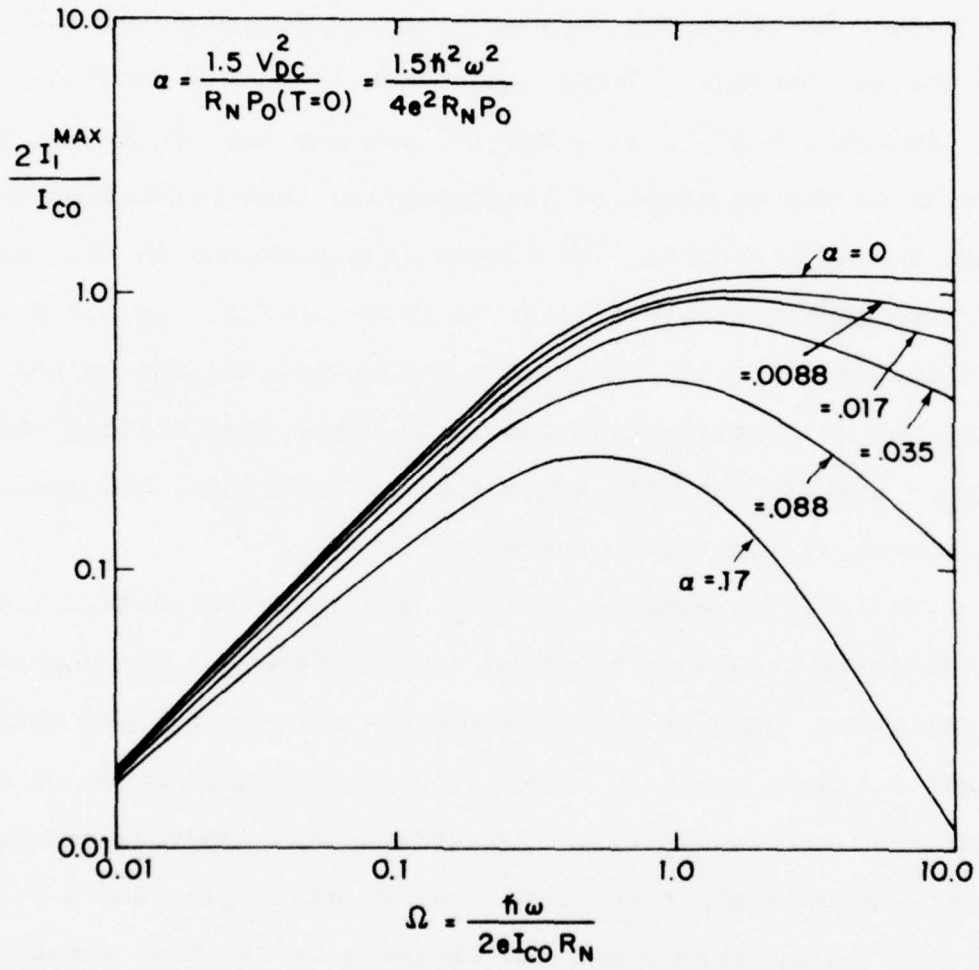

Fig. 5.6 Effects of heating on the maximum width of the first Josephson step for different values of $\alpha = P/P_o$, assuming $P = V^2/R_N$ at the step.

Behaviour similar to that shown in Fig. 5.6 has been reported as a function of frequency in cross-scratched indium microbridges by Clark and Lindelof.[80] They attributed this behaviour to the intrinsic relaxation time of the order parameter limiting the frequency of the Josephson oscillation in the microbridge. Using a phenomenological relaxation time for indium $\tau = 10^{-10} (1 - T/T_c)^{-1}$ seconds they generated the widths of the ac steps by incorporating this relaxation time into the TDGL theory. The curves they obtained in this manner are qualitatively similar to those in Fig. 5.6 for $\Omega > 1$, and agreed well with experiment. However, the use of this time has no justification and it is clear that heating can play a significant role since their microbridges had small P_o's even at low temperatures.

While it is expected that an intrinsic relaxation time should play a role in limiting the frequency of the Josephson oscillation, none of our experimental results suggest this limit has been reached. While the exact manner in which the intrinsic relaxation time will impose this limit is not understood, we have observed steps near T_c at frequencies $\nu = 10^{11}$ Hz at a temperature where the Ginzburg-Landau time corresponds to $\nu_{GL} = (\tau_{GL})^{-1} = 2 \times 10^{10}$ Hz.

The effects of self-heating can manifest themselves in yet another way by cutting off the oscillatory Bessel-function dependence (on the rf power level) of the amplitude

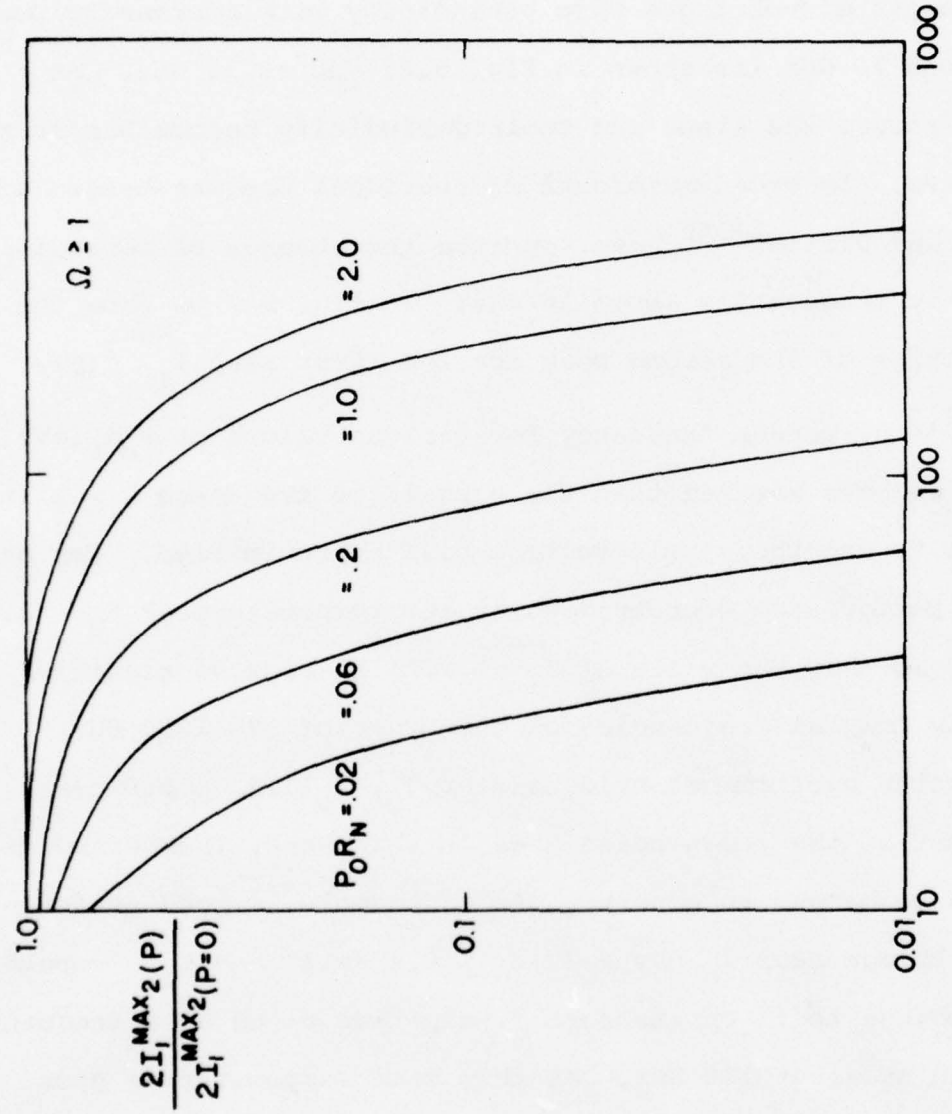

Fig. 5.7 Effects of heating on the second maximum of the width of the first ac step as a function of frequency for different values of $P_0R_N(mV)^2$.

of a given step. As the rf power is increased above the value which gives the first maximum for each step, the step widths at subsequent maxima are substantially reduced. Our variable-thickness microbridges show periodicity with increasing power at both 10 GHz (as shown in Fig. 5.2) and at 32 GHz. At high powers the steps and their periodicity become harder to observe. In two-dimensional microbridges Gregers-Hansen et al.[3] and Jillie[24,45] have reported the absence of periodicity at frequencies above 10 GHz. In Fig. 5.7 we show the reduction of the second peak for the first step $I_1^{max_2}(P)/I_1^{max_2}(P=0$, versus frequency for various values of $P_oR_N(mV)^2$. Here we have assumed that the normalized frequench $\Omega \geq 1$ in order to use the simple voltage-bias approximation. For our high performance microbridges at low temperatures $P_oR_N \sim 2.0\text{-}4.0$ $(mV)^2$ so that the value of $I_1^{max_2}$ will be reduced significantly only at frequencies of the order of 500-1000 GHz. In poorer performance bridges near T_c, $P_o(T)R_N \simeq 0.02\ (mV)^2$ so that at the frequencies used in this work, the periodicity would be harder to observe. As an example, a good performance bridge near T_c has $P_o(T)R_N \simeq 0.2\ (mV)^2$ and $I_1^{max_2}$ would be reduced to 1% of its zero dissipation value at a frequency of the order of 100 GHz. At this same temperature a poor performance bridge [$V_{max}(T = 0) = 1.0$ mV], would have $I_1^{max_2}$ reduced to 1% at 38 GHz. This qualitatively confirms our belief that for uniform-thickness microbridges the

absence of the periodicity of the ac steps at higher frequencies is due to self-heating effects, since we have assumed $P = V^2/R_N$, and thus the cut-off frequency obtained is only an upper limit.

5.2.6 Optimum Design of Thin Film Microbridges for High-Frequency Applications

The remarkable performance improvements at high frequencies observed in our tin and lead variable-thickness microbridges do not imply that they form the best possible configuration for high frequency applications. In order to design and fabricate a Josephson device useful at high frequencies one has to optimize the different parameters of the bridge to satisfy the following criteria: (a) heating effects should be minimized in order to extend the usefulness of the device to the highest possible frequency; (b) the impedance of the device should be as close to that of free space as possible in order to provide efficient coupling to the electromagnetic radiation one wishes to detect; (c) the $I_{co}R_N$ product should be maximized, since above the frequency $\omega_g = 2eI_{co}R_N/\hbar$ the resistive shunting degrades the performance of the device; (d) the capacitance C should be small since the RC time constant defines a frequency above which this capacitive shunting dominates, resulting in poorer performance.

The limitations due to capacitance are of little significance in microbridges since $C \sim 10^{-2}$ pF. On the other

hand, one requires an impedance as close to that of free space as possible. While this criterion suggests using materials with high T_c which typically have high resistivities and high $I_{co}R_N$ products, the heating model indicates that these materials are inferior because of their short coherence length and low termal conductivity. Therefore, the optimum materials appear to be In, Sn, Pb and Nb. We have discarded Al because of its low T_c and I_cR_N product. While niobium is still impractical because of its poor quality in thin films it is appealing in terms of its higher resistivity. The optimum solution to this problem should be the fabrication of a variable-thickness bridge in which the bridge and the banks are made of different materials. The bridge could be made of a high resistivity material such as niobium, and the banks of a high-conductivity material such as tin. While the niobium bridge will have a very small $\xi(0)$, the proximity to the banks, the high resistance, and the good cooling provided by the banks should outweigh this disadvantage.

The optimum design described above requires sophisticated fabrication techniques, especially in guaranteeing intimate electrical and thermal contact of the bridge with the bank materials. Two separate depostion processes would be required. However, we have tested the validity of the concept with

design shown in Fig. 5.8. This is a bridge consisting of a very dirty 0.13 μm thick tin film on top of which a clean, thick (1.5 μm) tin film is evaporated. This is done sequentially in the same deposition to insure good contact between the two films. In this manner when the film is cut with a diamond knife the bridge is made out of the very dirty material and thus should have a high R_N, while the thick clean film should provide good cooling. Initial tests of this concept have yielded a 2.5 ohm microbridge, totally non-hysteretic even at 1.5 K, which showed ac steps up to 4.2 mV. This performance is better than any of our single-material tin or lead microbridges and tends to confirm the validity of our arguments based on the heating model.

5.3 Further Evidence of The Well-Cooled Nature of The Variable Thickness Geometry

In the preceding sections we have made numerous references to the well-cooled nature of the variable-thickness microbridges based on their high-frequency performance. Additional evidence of this, some of it strikingly quantitative, can be obtained from the dc I-V characteristics of our variable-thickness microbridges.

5.3.1 Hysteresis

Skocpol et al,[4] have presented strong arguments for the connection between hysteresis and heating in both long and short microbridges. They argued that since no dissipation

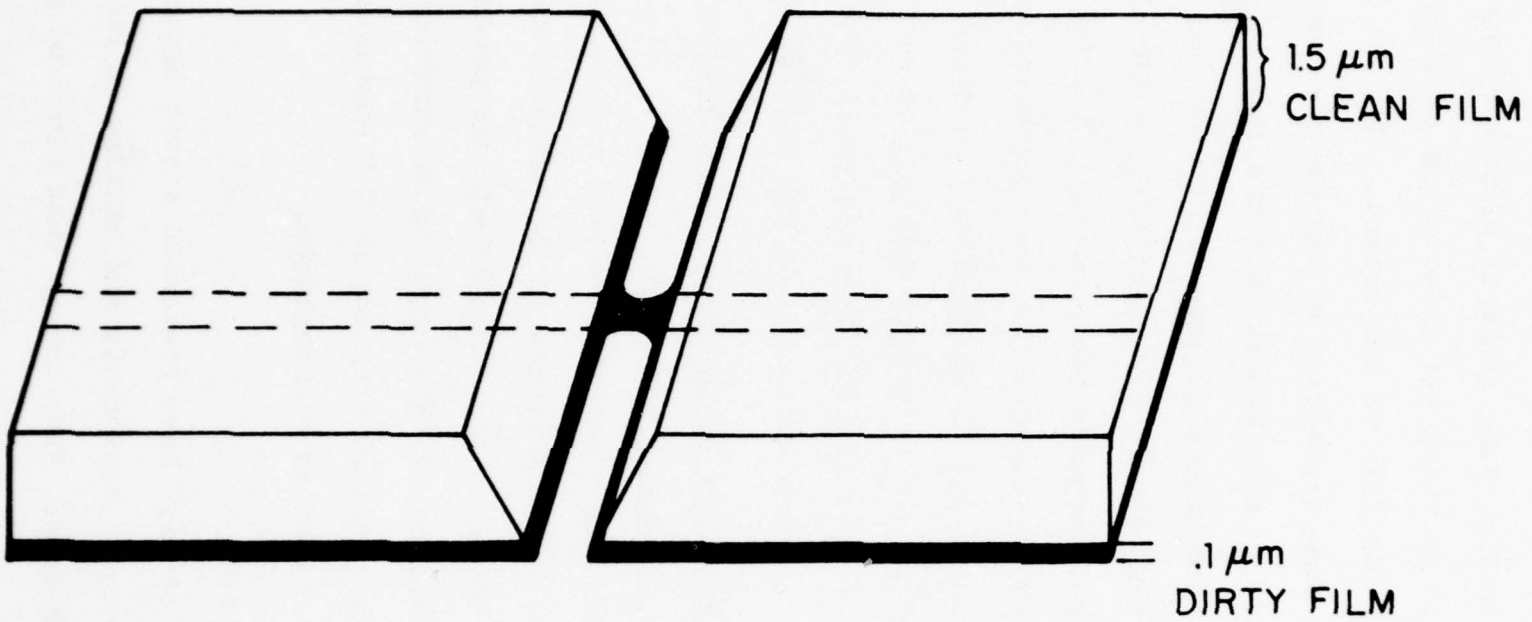

Fig. 5.8 Schematic of a bilayer microbridge for improved high-frequency performance.

occurs at zero voltage, the microbridge would reach its full critical current I_{co}. When this current is exceeded, dissipation occurs and if the bridge is not well cooled a normal spot would develop. The current required to sustain this hot spot would in many cases be smaller than I_{co} and thermal hysteresis would occur especially at low temperatures. This explanation is directly confirmed by our experiments. In Fig. 5.9(a) the I-V characteristics are shown for one of our best performance microbridges with V_{max} = 3.7 mV. Even at 2.1 K the curves are smooth and no hysteresis or multivaluedness occur. In contrast the I-V characteristics of a somewhat less optimal microbridge are shown in Fig. 5.9(b). This bridge has a V_{max} = 2.3 mV and P_o = 2.6 μW. At the lowest temperature a multivalued curve begins to develop and instabilities are observed at voltages at which the subharmonic gap structure (SGS) is observed. In microbridges showing even poorer high-frequency performance, this hysteresis becomes more pronounced and is first observed at temperatures much closer to T_c. Moreover, little or no change in the I-V characteristics or V_{max} occurs when the bath temperature passes through the lambda point. This indicates that, as was assumed in the heating model, the predominant temperature rise is associated with the thermal resistances of the metal rather than that of surface heat transfer to the bath.

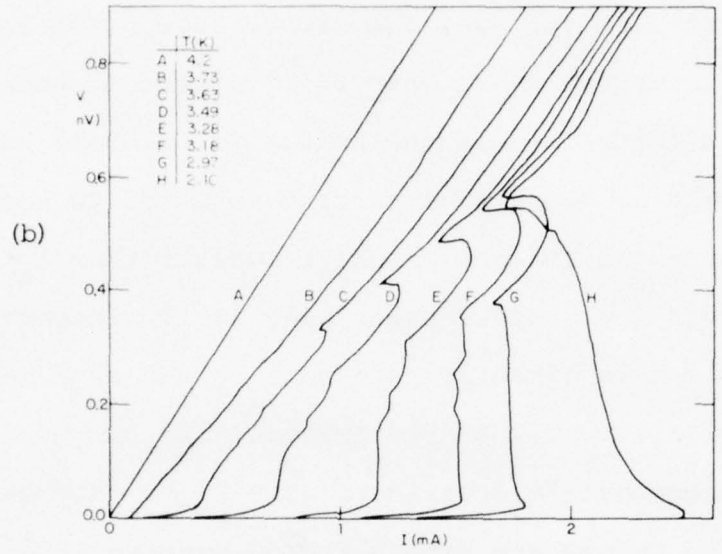

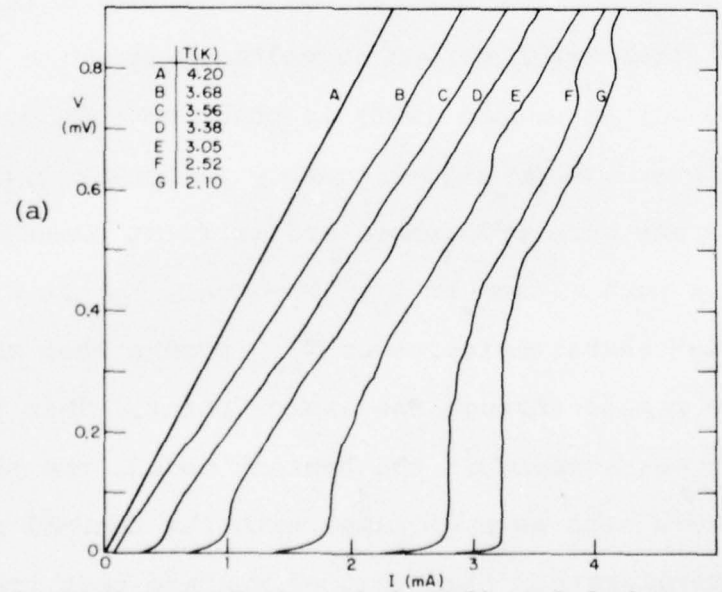

Fig. 5.9 I-V characteristics of a) Well-cooled microbridge (#9). b) Very well-cooled microbridge (#11).

5.3.2 The Subharmonic Gap Structure

Further quantitative and qualitative evidence of the amount of heating present in our microbridges is provided by the gap and subharmonic gap structure (SGS) observed on the I-V characteristics at the gap voltage $2\Delta/e$ and submultiples of it. This structure has previously been observed in thin-film microbridges and various explanations for its origin have been proposed and extensively debated.[81-83]

The reduced hysteresis of our microbridges allows us to observe this structure over the whole bath temperature range in our well-cooled microbridges. In Fig. 5.9(a) the structure is quite subtle, especially at the subharmonics of the gap $V_n = 2\Delta(T)/ne$ where $n > 1$. In Fig. 5.9(b), this structure is quite pronounced both for the gap $2\Delta(T)/e$ and its submultiples. Typically the less well-cooled the bridge, the sharper the observed structure becomes. When we plot $-dI/dV$ against voltage as shown in Fig. 5.10 (bridge #4) this structure can clearly be seen as peaks. We identify the characteristic voltage V_n for the n^{th} peak as the sharpest feature in the I-V characteristics, which corresponds to the inflection point to the right of each peak in the dI/dV measurement. The results would not vary significantly if any other part of the peak were chosen as the index, as long as the microbridge was fairly well-cooled.

As shown in Fig. 5.10, as the temperature is lowered the peaks become sharper and more peaks are observable. Typically from four to seven of these peaks are observed, depending on the microbridge. In not so well-cooled microbridges as in Fig. 5.9(b) instabilities and jumps indicating the presence of negative resistance regions appear first in the gap peak ($n = 1$) and later in the higher order peaks. Finally, at very low temperatures the whole region becomes hysteretic.

When the gap values are obtained from the SGS, we observe that the higher order peaks ($n > 2$) seem to correspond to approximately the correct value of the gap from the BCS theory, but the $n = 1$ and $n = 2$ peaks can be significantly depressed in voltage. These differences become even more pronounced at low temperatures. In Fig. 5.11(a) and (b) we have plotted the inferred gap voltages nV_n versus the voltage V_n for two microbridges. If these structures correspond to the same value of the gap they should yield a horizontal line $nV_n = 2\Delta/e$. As shown in Fig. 5.11(c) the nV_n values for large n extrapolated to zero dissipation (zero voltage) agree well with the theoretical BCS gap function for tin evaluated at that temperature. The depressed values for large dissipation seem to correspond to definite rises of the temperature above that of the bath due to the increased dissipation at higher voltages. This is shown in

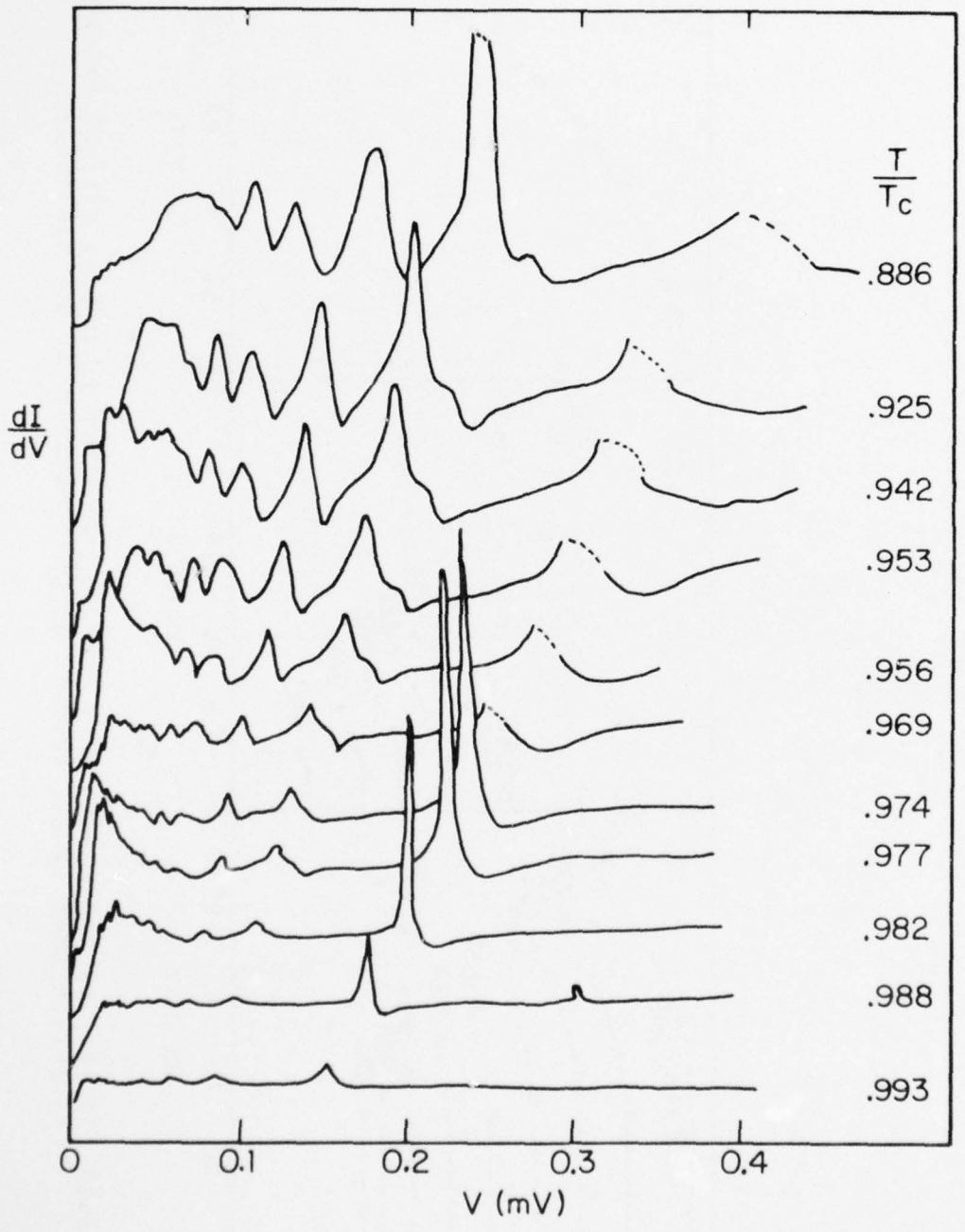

Fig. 5.10 Derivative curves showing the variation of the subharmonic gap structure with temperature (#4).

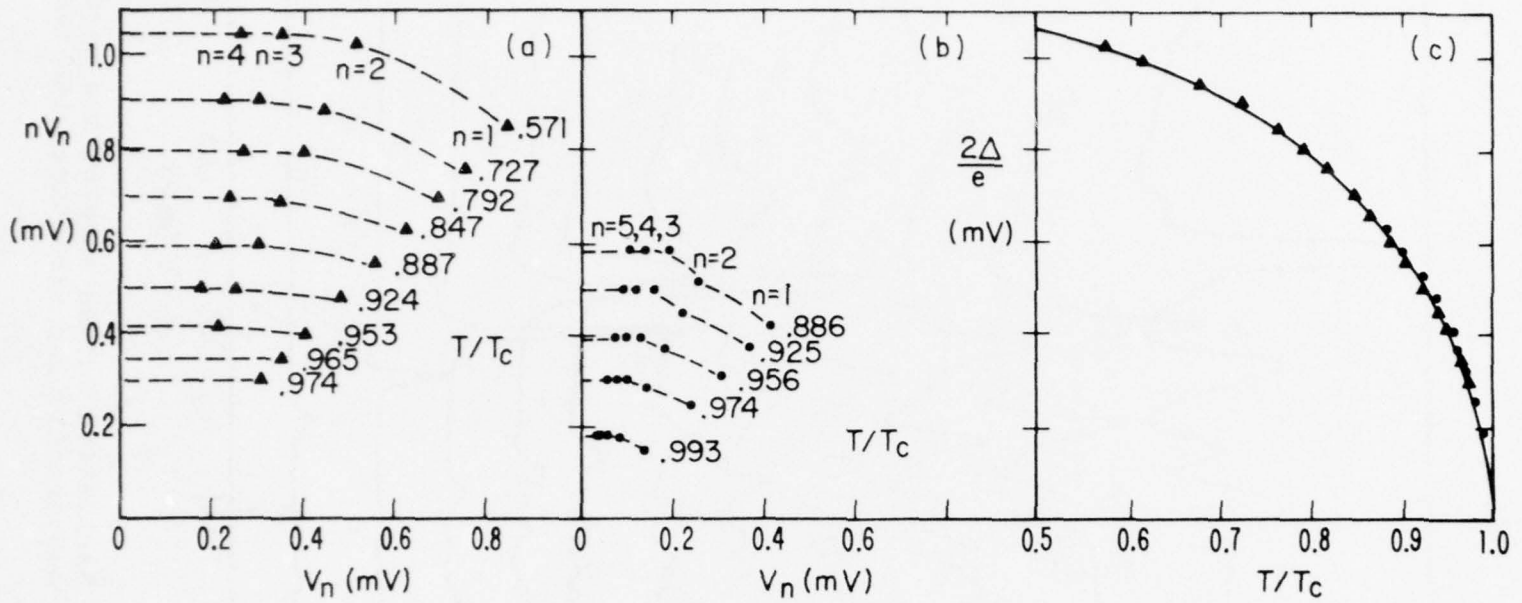

Fig. 5.11 Gap values determined from the gap structure a) bridge #11; b) bridge #4; c) low voltage limits from a) and b) compared to the BCS theory.

Fig. 5.9(a) where the gap value at the lowest temperature is below the value expected from the BCS theory, but above that observed at the same temperature in the less well-cooled bridge shown in Fig. 5.9(b). This is further confirmed in Table 5.4 where we show the experimental value of $V_1 = 2\Delta/e$ at 2.1 K as well as the value of V_{max} for a selection of microbridges. The correlation between high V_{max} and high V_1 is very good. We have found that by observing the value of the gap at low temperatures and comparing it to other microbridges, we can predict an approximate value of V_{max} from the I-V characteristics even before any microwave radiation is applied to it.

It is possible to discuss the observed temperature rises in a more quantitative fashion. In Fig. 5.12 we plot the values of the temperature rise inferred from the observed gap for the n = 1 and n = 2 peaks for one of our microbridges. To check whether the inferred temperature rises depend on the power dissipation in a reasonable way, we have adopted a simple model. The relevant gap value is taken to be determined in a region at a distance of the order of the coherence length from the bridge center since the chemical potential of the pairs μ_p, should approach a constant outside a region of size $\sim \xi$ within which μ_p is time-dependent. Assuming a three-dimensional radial heat flow which carries away the total power dissipated, we integrate from ∞ to ξ and obtain

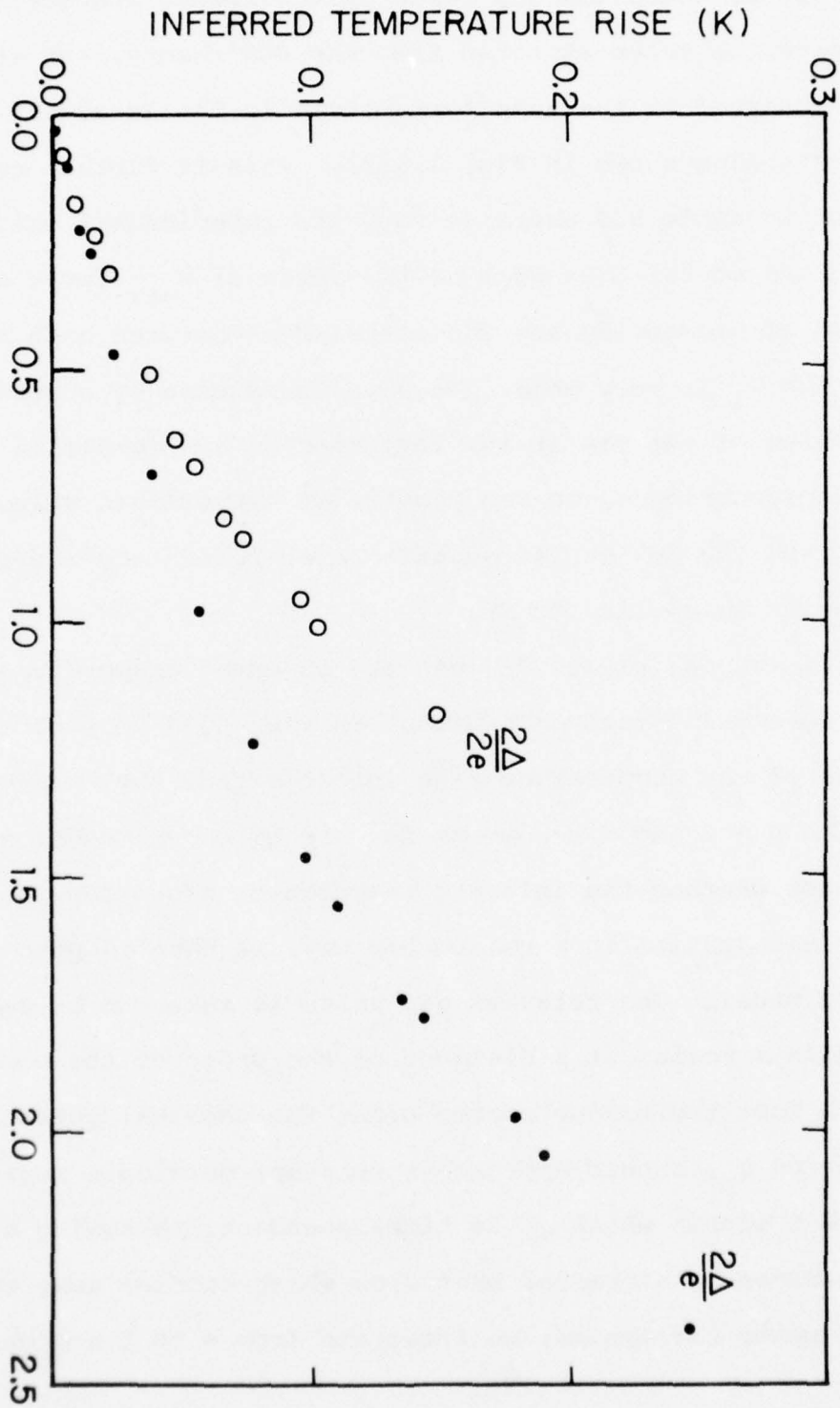

Fig. 5.12 Inferred temperature rise from the gap and n=2 subharmonic of bridge #4 as a function of the power dissipated.

Table 5.4

Values of V_{max} and V_1 at 2.1 K for a Selection of Microbridges

Bridge #	V_{max} (mV)	V_1 (mV)
23	4.2	0.98
17	> 1.5*	0.90
11	3.7+	0.86
16	3.7	0.95
10	2.6	0.84
9	2.3	0.84
18	2.0	0.73
3	0.98+	0.73
7	1.7	0.55
4	1.5+	0.56
5	1.4+	0.54
6	0.7	0.50
14	< 1.0	0.50
13	< 0.8	0.50

+ Limit had not been reached at maximum microwave power available

* Bridge was used for far-infrared experiments described in Chapter Six, and V_{max} could not accurately be measured.

the temperature rise

$$T_{local} - T_{bath} = \frac{P}{2\Omega K\xi} \tag{5.33}$$

where K is the thermal conductivity and Ω is the solid angle for heat flow in each of the banks. In Fig. 5.13 we plot the temperature rise from the SGS but now against P/ξ where we have used the coherence length at the bath temperature. The data now includes the data from the n = 1,2 peaks of the bridge in Fig. 5.12 as well as the n = 1 peak of our best cooled microbridge. The data for both microbridges fall on the same straight line as expected from Eq. (5.33). If we use $\Omega = 2\pi/3$ and the observed slope, we obtain a very reasonable value for the thermal conductivity of tin of K = 0.065 W/cm-K.

Another indication of the well-cooled nature of the microbridges is obtained when they are irradiated by microwaves. In contrast to other cross-scratched bridges,[81] the development of the ac steps does not cause the SGS to fade away until the power level is increased sufficiently that ac steps are observed at voltages well above the SGS. When the structure starts to disappear, it first decreases in strength and later shifts to lower voltages as the microwaves heat the bridge.

The effects of nonequilibrium dissipation make it

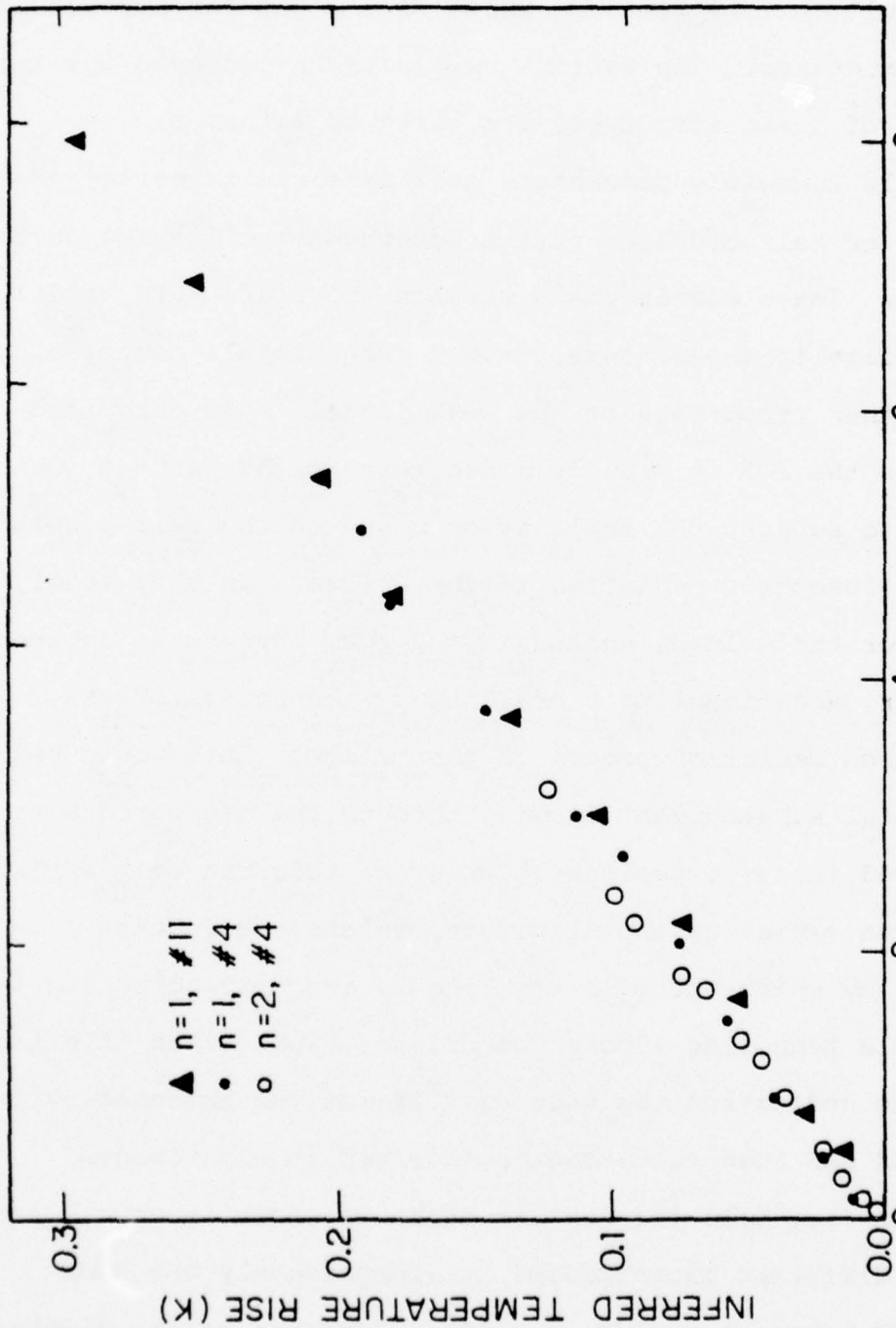

Fig. 5.13 Dependence of the temperature rise inferred from the gap structure on the power dissipated.

difficult to interpret the shape of the gap and subharmonic gap structures. The various explanations proposed for the origin of these structures are based on either single-particle tunneling processes, multiparticle tunneling processes or self-coupling of the Josephson oscillation to the bridge. These models yield results which are hard to differentiate in experiments, except for possible correlations with other properties of the weak links.[84] In our microbridges the SGS is usually a decrease in the current, which tends to support the explanation based on the self-coupling of the Josephson radiation in the bridge. In this model, whenever the voltage exceeds $V = 2\Delta/me$, where m is an even integer, additional pair breaking by absorption of the Josephson radiation occurs in the bridge. This would reduce the total supercurrent flowing through the microbridge as observed in our experiment. However, this can only explain the even series of the structure, unless one invokes processes by which the pair-breaking is accompanied by quasiparticle tunneling across the bridge. This makes it difficult to understand the near equality of the intensities of the odd and even subharmonics observed in experiments.

In Fig. 5.14 the gap structure is shown in detail for seven different microbridges at approximately the same reduced temperature $T/T_c = 0.885$. (Because of the difference in T_c and variations in the temperature at which the curves were taken, T/T_c values range from $T/T_c = 0.882$ to 0.891,

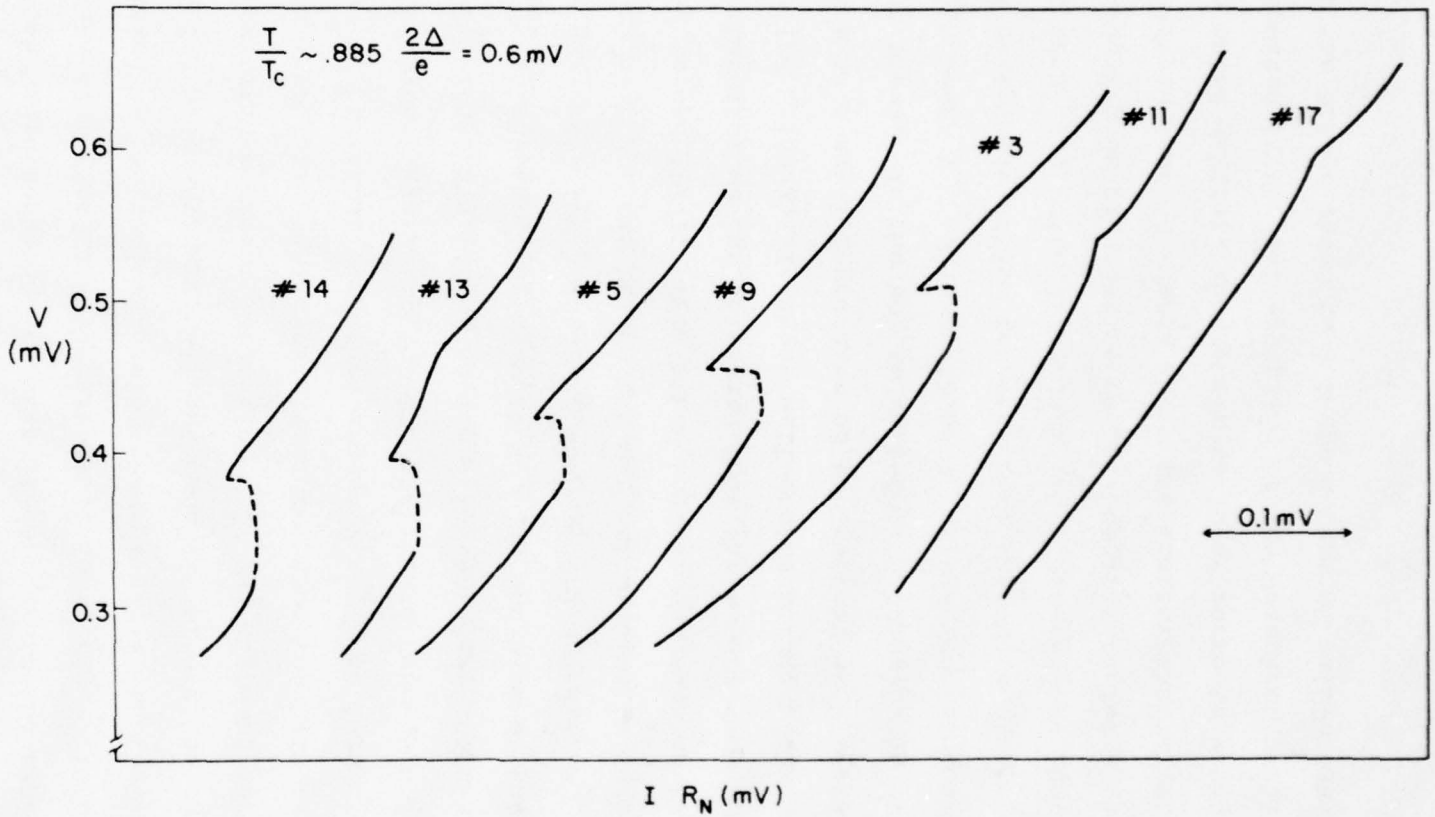

Fig. 5.14 Shape of the gap structure for various bridges with different degrees of cooling at T/T_c=0.885.

which would result in only small changes in the expected value of the gap.) The current scale in Fig. 5.14 has been scaled by the resistances of the bridges so that all the curves have approximately the same slope, and the curves plotted in order of increasing V_1. The shape of the I-V characteristic varies significantly from the bridges with a low V_1, to those with the largest V_1. While accurate V_{max} data is not available for all the bridges shown in Fig. 5.14, where it is available the trend in the shape correlates with V_{max} in the same way as with V_1. In the case of those bridges with the highest V_1 such as #11 and #17, V_{max} was very high for one bridge and was not studied in detail for the second (#17). From other indications such as the hysteresis, we can determine that these were very well-cooled bridges. In these well-cooled bridges, the gap structure is a small depression of the current at V_1 relative to the trend. In the not so well-cooled bridges, as determined from lower V_{max} values, lower V_1 values and large amounts of hysteresis at low temperatures, the shape of the gap structure is quite different. In these bridges there is a broad region of negative resistance accompanied by a large shift to lower currents above the characteristic voltage V_1. As noted earlier, this shift to lower currents would be expected if the self-coupling of the Josephson oscillation in the bridge leads to a large amount of pair-breaking and

therefore a reduction of the supercurrent flowing through the bridge.

We believe that the voltage width of the gap structure observed in our microbridges can be attributed to the temperature rise producing a gradient of the gap in the microbridge and part of the banks. Thus, the onset of the pair braking will not be sharply defined at $V_1 = 2\Delta(T_b)/e$, corresponding to the bath temperature but rather spread over a range of gap values determined by the temperature rise near the bridge. The actual origin of the negative resistance regions is more difficult to explain. The current jumps suddenly to a stable lower value at higher voltages. One could envision some sort of instability created by the nonequilibrium nature of the quasi-particles created at the gap edge, which will not readily diffuse out of the region of depressed gap in a poorly-cooled microbridge. The occupation numbers of the quasi-particles near the gap will be strongly modified, leading to changes in the gap and thus the total supercurrent through the bridge. Any further interpretation of these features in poorly-cooled bridges is complicated by the temperature distribution present as well as by the "feedback effect" that a change in the gap will have in the pair-breaking process.

The overall trend observed in the gap structure as the cooling is improved is similar to that reported by Yanson[34] in

microbridges formed as shorts through dielectric layers. In Yanson's bridges, however, a change is observed from a reduction of the total current above V_1, to an increase of the total current above V_1. The latter was only observed in microbridges with normal state resistances higher than those of our microbridges. This increase of the current at the gap is typically observed[84] in high-resistance well-cooled point contacts, and suggests a common origin for the SGS in these two types of weak links when they are very well-cooled.

CHAPTER SIX

OTHER TOPICS

6.1 Detection of Far-Infrared Radiation with Variable-Thickness Microbridges

The observation of microwave-induced Josephson steps up to voltages corresponding to far-infrared frequencies in our variable-thickness microbridges encouraged us to attempt the observation of an a step induced by far-infrared (FIR) radiation. This unsuccessful attempt is described in this section and the experimental difficulties encountered are discussed.

An optically-pumped dielectric-waveguide FIR laser built in our laboratory by D. Weitz was used in these experiments. We used the 496 μm line of CH_3F gas with a maximum output power of ~ 10 mW. The radiation was focused on the microbridge through two crystal quartz windows in the side of the helium dewar.

The samples used in these experiments were similar to those used in our earlier work, except that a thin-film half-wave dipole antenna which was cut with a diamond knife next to the bridge as shown schematically in the inset of Fig. 6.1(a). The purpose of this antenna was to improve the coupling of the radiation to the microbridge. The actual length of the antenna was 150-250 μm depending on the sample

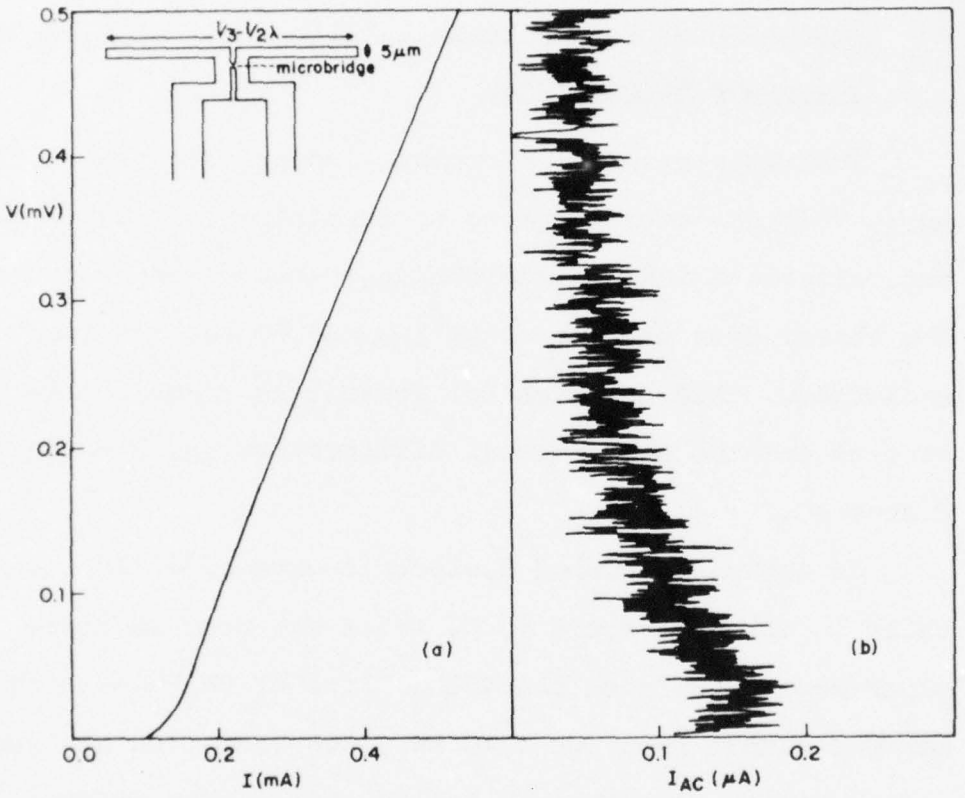

Fig. 6.1 (a) I-V characteristic of bridge #17. (b) Response I_{ac} of the same bridge to far-infrared radiation. The inset shows the antenna geometry.

and run. The length of the antenna was purposely made shorter than half the wavelength of the radiation in order to compensate for the reduction factors due to the finite width of the antenna arms, the dielectric constant of the substrate, and the thickness of the sapphire substrate.[84,85] At 4.2 K, the absorption of the far-infrared radiation by the sapphire should be small and no significant heating of the substrate should occur. The sample was mounted so that the antenna arms could be rotated about an axis perpendicular to the polarization and the direction of the incident radiation.

A total of six samples with resistances ranging from 0.15-1.25 ohms were tested. In none of these samples was the strength of the coupling sufficient to detect the effects of the FIR directly on the I-V characteristics or its derivative dI/dV. No ac Josephson steps were observed at 1.25 mV.

A small response of the sample to the radiation could be observed by chopping the laser beam and detecting the current change, I_{ac}, through the bridge by measuring the voltage across the 0.1 ohm resistor in series with the bridge at the chopping frequency with a PAR 124 lock-in amplifier. In Fig. 6.1(a) and (b) we show the I-V characteristic at 3.4 K and we show the observed response I_{ac} as a function of voltage for the best sample used. This sample had a normal state resistance of 1.25 ohm and therefore was essentially

voltage-biased by the biasing circuit and current-biased by the radiation. The sample was completely nonhysteretic at 2.1 K with a gap structure at $V_1 = 0.90$ mV. From the discussions of Chapter Five, one would expect a V_{max} of at least 3.0 mV for these characteristics. Microwave steps were observed up to 1.5 mV by irradiating the sample with 32 GHz radiation with the Gunn diode placed three inches away from the crystal quartz windows in the side of the dewar. This did not constitute an upper limit as not enough microwaves could be coupled with this crude arrangement to determine V_{max}. The FIR response shown in Fig. 6.1(b) is the maximum response observed for any orientation of the sample. The response was found to be quite sensitive to the orientation, suggesting some form of antenna response. However, the small response observed made it difficult to accurately determine the antenna pattern. If one assumes that the depression of the critical current in the presence of the radiation is given by the zero order Bessel function, then for small signal currents this reduction I_o can be written as

$$I_o = I_{co}\left[1 - \left(\frac{eV_{rf}}{\hbar\omega_{rf}}\right)^2\right] \qquad (6.1)$$

where V_{rf} is the rf voltage. Then assuming the I-V characteristic is described by the RSJ model, the current change I_{ac} will be proportional to

$$I_{ac} \propto \frac{I_{co}^2 V_{rf}^2}{I} \qquad (6.2)$$

as long as $I > I_{co}$. While the observed response is qualitatively similar to Eq. (6.2) at least at low voltages, this does not necessarily rule out the possibility that the observed response is due to heating in the metal. From Eq. (5.24), the change in I_{co} in the presence of small dissipation, also has the form of Eq. (6.1). In order to separate these two effects, one would need a more extensive knowledge of the coupling or the direct observation of an ac step.

If the observed response corresponded to a true Josephson response, it would not be surprising that no ac step was observed directly on the I-V characteristics. Thermal noise rounding would prevent the observation of a step until $I_n = I_{co} J_n(2eV_{rf}/\hbar\omega_{rf}) \gtrsim ekT_n/\hbar$. In our experiment $I_1 \lesssim 10^{-8}$ amps in the best case and $ekT_n/\hbar \approx 10^{-7}$ so that better coupling would have been required in order to observe the first ac step of the 496 μm radiation.

These results emphasize the disadvantage of the low impedance of our microbridges. If their impedance could be increased to $R_N \approx 10$ ohm without significantly decreasing the thermal conductivity of the banks as suggested in section 5.2.6, the coupling should be significantly improved and an

ac step might be observed. Further improvements could be made in the antenna design by reducing the width of the antenna or by attempting to determine its optimum length. However, determining this length can be very difficult as it would require a series of runs in which the antenna length was shortened each time by small amounts and the same microbridge used without any change of its properties.

6.2 Arrays of Microbridges in Series

In the course of our experiments, we became interested in exploring the feasibility of studying arrays of microbridges made with our fabrication technique. This effort was not a comprehensive study of such arrays, but rather a test of whether we could produce with sufficient reliability many microbridges in series with properties as nearly identical as possible. Arrays of microbridges are quite interesting from the point of view of applications and as useful tools for the study of the nonequilibrium properties of superconductors. From a practical point of view, if it were possible to fabricate a coherent array of n identical microbridges then the impedance of the array would be nR_N, where R_N is the normal state resistance of each individual microbridge. Furthermore, the power of the radiation emitted by such an array would scale as n^2 as long as $nR_n \ll Z_o$, the impedance of free space.[86] This super-radiant property of arrays has been observed in series arrays of tunnel

junctions[87] as well as proximity effect microbridges.[88] These arrays can also be useful in studying nonequilibrium properties of superconductors by investigating the interactions between pairs of microbridges which are independently biased with currents flowing in either the same or opposite directions.[24,45,89-91]

The samples used in our experiments were fabricated using the same techniques outlined in Chapter Two. Care was taken that the pressure applied in making the cuts with the diamond knife was similar for both bridges. The thickness of the banks had to be less than 0.5-0.7 μm in order to fabricate closely spaced pairs of microbridges. Otherwise when we attempted to fabricate microbridges separated by less than 3 μm from center-to-center, making the second microbridge would push the thick bank material onto the first bridge and it would be severely distorted if not destroyed.

All of our pairs of microbridges were biased in series. For separations larger than 6 μm our pairs behaved as two independent microbridges with two distinct critical currents. It was possible to observe separately the gap and subharmonic gap structure for each microbridge. When irradiated with microwaves with low amounts of power, the total voltage across the two bridges showed ac steps with nonzero differential resistance, corresponding to the sum of a flat step in one bridge, and the differential resistance of the other. At fairly high microwave powers these ac steps would overlap

in current and a zero differential resistance would be observed in this region of overlap at twice the Josephson voltage V_J for a single bridge. This so-called "synchronization" has been observed in arrays of flat microbridges separated by as much as 50 μm.[24,45]

For separations smaller than 6 μm, a different behaviour was observed both in the absence and presence of microwave radiation. A single critical current I_{co} could be identified for a wide range of temperatures. This form of critical current locking was observed in most microbridges separated by less than 6 μm. Similar results have previously been reported in pairs of flat indium microbridges by Jillie et al.[24,89] They interpreted this behaviour as being due to the mutual reinforcement of the bridges, when they are separated by a distance smaller than the quasi-particle diffusion length. In our samples we observe this critical current locking over a much wider temperature range (down to T/T_c of 0.8 or less). This was possible because heating effects in our samples do not become important until much lower temperatures. For temperatures below $T/T_c \sim 0.75$ a very small feature suggestive of a second critical current was observed when dI/dV was plotted against voltage. This second feature was, however, quite different than that observed when the first bridge began to develop a voltage and it was not clear whether it truly corresponded to a second

critical current. Whenever a single critical current was observed, a single gap structure was observed at twice the gap voltage V_1 for a single bridge, at all temperatures, suggesting the I-V curves of the two bridges were indeed quite similar to each other.

The most interesting effect observed in our pairs of microbridges occurred for our highest impedance pair $R_N \sim 2$ ohm where the bridges were separated by 6 μm. This pair exhibited critical current locking and when irradiated with microwaves it showed the behaviour seen in Fig. 6.2. At very small microwave powers a small ac step with nonzero differential resistance was observed at $2V_J$ ($\sim$ 132 μV). Any increase of the power yielded zero differential resistance steps at $2V_J$. Note, however, the large width of the step at $2V_J$. If one compares the maximum width of this first step to the zero power critical current, a value $2I_1^{max}/I_{co} \sim 1.5 - 2.0$ is obtained, which is twice as large as any observed in our single microbridges as described in section 5.2.5 and is almost twice as large as the maximum width predicted by the RSJ model for any bias condition. Note also that there is also a large Wyatt-Dayem effect, which is quite large considering the high resistance of the microbridges. At higher voltages the next 2-3 steps also show a zero differential resistance and large widths. For high microwave powers the ac steps begin exhibiting a finite slope as seen

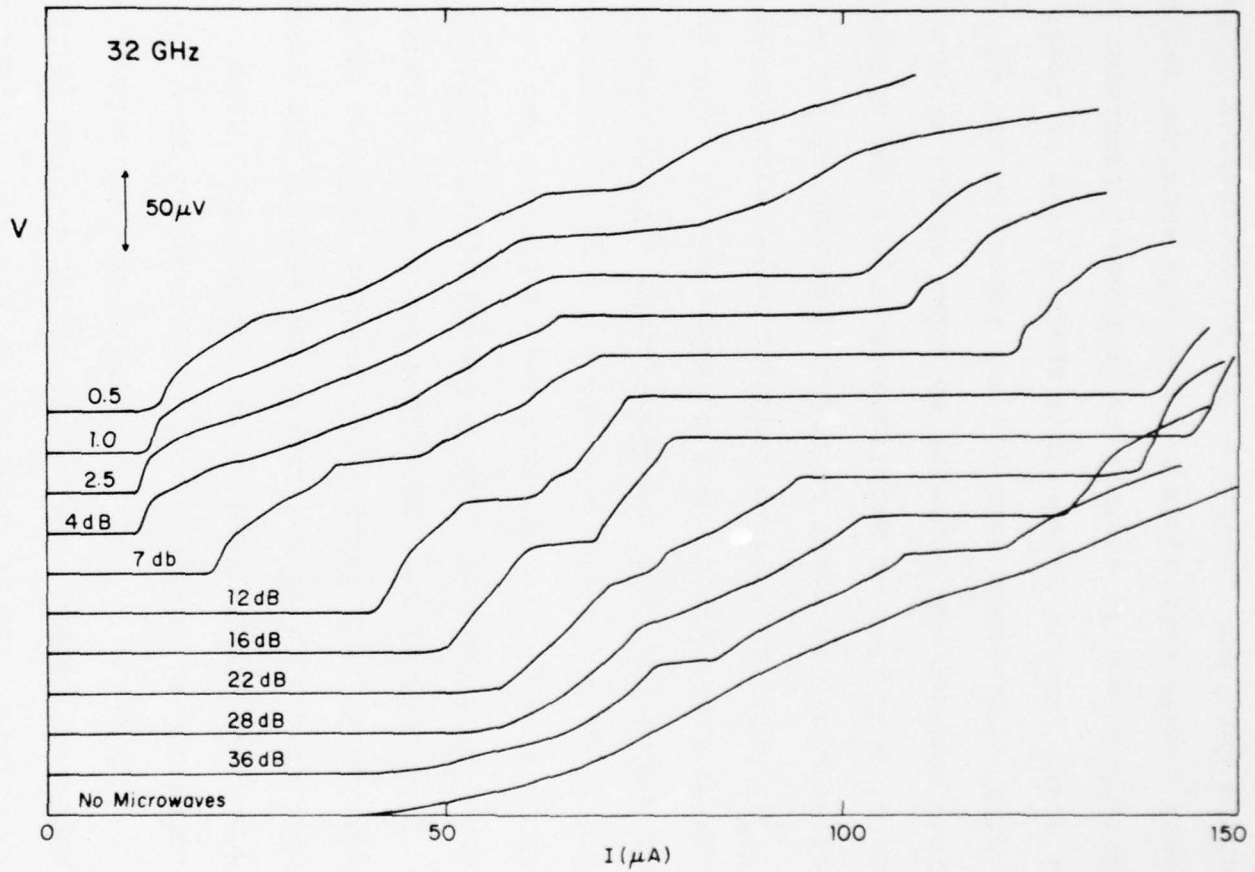

Fig. 6.2 Response of a high resistance pair of microbridges to 32 GHz radiation.

in the last curve of Fig. 6.2. As the temperature is lowered the observed behaviour is similar to that shown in this figure down to $T/T_c \sim 0.74$. Below this temperature a zero differential resistance step is only observed at high microwave powers when the individual steps are large enough to partially overlap. Because of the large separation of the bridges ($\sim 6\ \mu m$), this suggests the interaction occurs through the branch-mixing length λ_Q.[65] At these temperatures the width of the ac step at V_J becomes comparable to that of the step at $2V_J$. The interpretation of these results is quite difficult without knowing the behaviour of the ac steps for each independent microbridge. From our experiments on single microbridges it appears quite unlikely that the individual steps would be so large for each microbridge. It could be that the large steps are due to a voltage-locking of both microbridges whenever one of the microbridges is biased to a constant voltage step.

These observations in arrays of microbridges indicate that our fabrication technique could be quite useful in studying the interactions of microbridges. Because of reduced heating, the variable-thickness geometry would have the advantage of providing a wider temperature range to study the interactions of the bridges. Obviously in order to further clarify the nature of the effects observed, independent bias of the microbridges would be necessary.

CHAPTER SEVEN

CONCLUSIONS

When our experimental investigation of the properties of variable-thickness microbridges began it was clear that heating effects severely limited the high frequency performance of two-dimensional microbridges. It was our initial objective to fabricate microbridges in which heating effects would be significantly reduced by the thicker banks so that their performance at high frequencies could be extended to the far-infrared region of the spectrum. We found that besides obtaining the improved high frequency performance, our variable-thickness microbridges were quite useful in studying the properties of microbridges, as the improved cooling allowed us to study them over a wider temperature range than had previously been possible. Furthermore by fabricating bridges with varying degrees of cooling, it was possible to study and explain how the various regimes of the I-V characteristics and the ac response of the microbridges were affected by heating. Our study of the wide variety of phenomena observed in our microbridges in different regimes has helped identify and explain the extent to which their Josephson behaviour is modified by nonequilibrium dissipation and other nonequilibrium effects. In what follows we will consider regions of increasing voltage along the I-V

curves of the bridges summarizing our current understanding of the phenomena, and identifying areas where further investigation is required.

The zero voltage critical currents of both our tin and lead microbridges were found to have a Josephson-like temperature dependence, as expected from their small size and the presence of the thick banks. This is to be contrasted with the wide range of behaviour observed in two-dimensional microbridges. The magnitudes of the $I_{co}R_N$ products of our microbridges at all temperatures were found to be larger than those expected for weak link devices. While these larger values are consistent with recent[32] microscopic calculations at low temperatures, no explanation is yet available for the magnitudes of the critical currents near T_c. In this regime it is clear that further theoretical analysis is required for the case of the neck radius of the weak link being comparable to the mean free path or the coherence length of the material. Even at the lowest temperatures the onset of resistance at I_{co} in our best-cooled microbridges was found to be completely nonhysteretic, confirming the heating-related origin of the hysteresis which is observed in most superconducting microbridges.

At low voltages (0-50 μV) all of our tin microbridges exhibited a foot-like feature characterized by an initial region of constant differential resistance followed by a

rapid growth of the voltage with little current change at a characteristic current I_{c1}. This feature became more pronounced at low temperatures unless heating effects became significant. Systematic evidence has been presented which supports the idea that this low voltage feature is caused by an enhancement of the supercurrent flowing through the weak link. This enhancement is produced by the nonequilibrium quasi-particles not being able to relax because their relaxation time is slow compared to the Josephson period. Comparisons of the experimental data with the predictions of the models of Golub and of Aslamazov and Larkin have shown many points of agreement in the regimes where the theories are applicable. Good agreement was found with the magnitude and temperature dependence of the initial differential resistance observed, the maximum enhanced supercurrent I_{c1} and the relation of the excess supercurrent $\overline{I}_s$ to I_{c1} rather than I_{co}.

While both the Golub and the Aslamazov-Larkin models agree well with some aspects of our experimental data, further theoretical work will be required in order to achieve a complete understanding of all of the observed phenomena. The models are only complementary, being applicable in different regimes. Furthermore, some of the observed behaviour, such as the absence of an initial steep rise in voltage at I_{co} and the saturation of I_{c1} at low temperatures, are not predicted by the models. Golub's model has been used in the

low voltage regime where approximate solutions to the non-equilibrium Ginzburg-Landau equations for short weak links are valid. Numerical solutions of this equation are required to extend the comparison of this theory to higher voltages. At still higher voltages the assumptions of both models would break down, as the Josephson period τ_J becomes comparable to the diffusion time τ_D or the finite relaxation time of the order parameter τ_{GL}. The role of these relaxation times in determining the I-V characteristics remains unclear at this time except in the context of time-dependent Ginzburg-Landau theory, which might not be justified in the regimes of interest.

Experimentally, further work is required in order to understand the low voltage I-V characteristics of bridges of other materials. We found the characteristics of our lead microbridges to be quite different at low voltages than those of our tin bridges. It is probable that these differences arise from the large width of these bridges compared to the coherence length, which would allow single vortices to flow through the bridges, making flux-flow effects important. Studies of other materials with small coherence lengths might help clarify this point. It would also be quite interesting to investigate the low voltage regime of aluminum microbridges. For bridge lengths larger than those of our microbridges one would expect to observe similar enhancement

effects although at much lower voltages than in tin.

At higher voltages ($V \geq 50\ \mu V$) the I-V characteristics of tin microbridges are severely affected by heating effects and modified by the characteristic features of the gap and subharmonic gap structures at $V_n = 2\Delta(T)/ne$ where $n = 1,2, \ldots$. We found the actual voltages at which this structure was observed could be depressed significantly by heating effects. The actual shape of the SGS structure was found to be broadened both in voltage and current by heating effects, particularly when it occurred at lower voltages in bridges with poorer high frequency performance and more hysteresis at low temperatures. This confirmed the correlation between heating, hysteresis and the voltage limit for high frequency performance in superconducting microbridges. Using a simple heating model we have confirmed that the temperature rise inferred from the gap and subharmonic gap structure depends on the dissipated power in a reasonable way. The values of the gap obtained from the zero dissipation extrapolation were found to be in very good agreement with the BCS theory.

When our variable-thickness microbridges were irradiated with microwaves, nonequilibrium effects were found to significantly modify their properties at all voltages. We observed the Wyatt-Dayem effect only in our tin microbridges, and enhancements of the critical current of as much as 50%

AD-A049 779 HARVARD UNIV CAMBRIDGE MA DIV OF APPLIED SCIENCES F/G 9/5
NONEQUILIBRIUM PROPERTIES OF VARIABLE-THICKNESS SUPERCONDUCTING--ETC(U)
JAN 78 M OCTAVIO N00014-77-C-0085
UNCLASSIFIED TR-13 NL

3 OF 3
AD A049779

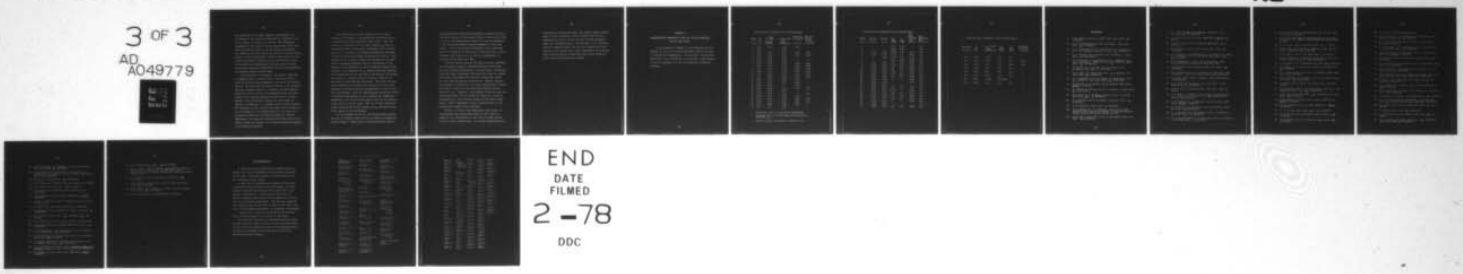

END
DATE FILMED
2-78
DDC

were observed in our lowest impedance microbridges. No enhancement of the critical temperature was observed in any of our samples at either 10 or 32 GHz. The temperature dependence of the critical current enhancements differ from those observed by others in tin and indium microbridges. Our results do not help clarify the origin of the Wyatt-Dayem effect in short microbridges. Further understanding of this effect would require theoretical work more closely related to the particular experimental situations used and would require more extensive experimental study of the enhancements in variable-thickness microbridges.

In the presence of microwaves, our bridges showed the ac Josephson effect, and the maximum voltage at which it could be observed clearly depended on the extent of heating effects. We found that the improved cooling of the variable-thickness geometry allowed us to observe microwave-induced steps up to 4 mV, a factor of 4 improvement over any microbridge of any material reported by other workers to date. However, with far-infrared radiation we were unable to observe a fundamental n = 1 Josephson step at these voltages. The limitation in this case did not appear to be heating, but the low impedance of our samples which did not allow us to efficiently couple the far-infrared radiation. Further improvements in antenna and bridge design should make it possible to study the response of variable-thickness microbridges to far-infrared radiation.

Our observations at high voltages led to a simple analysis of the effect of nonequilibrium dissipation on the ac properties of three-dimensional weak links. From this analysis, we found that the critical current I_{co} falls as $\exp(-P/P_o)$, where P is the power dissipated in the junction and P_o is a material- and temperature-dependent parameter of order 10 μW for most typical materials far from T_c. This decrease of the critical current with dissipation was found to be in excellent agreement with our observations of the decrease of the amplitudes of the ac Josephson steps at high voltages. This reduction of I_{co} together with the increased noise temperature of the weak link in the presence of dissipation leads to a maximum voltage at which ac steps can be observed for given junction parameters. The values for this limit predicted by the model were found to be in very good agreement with those observed experimentally in both tin and lead microbridges. Using the experimentally determined limits at different temperatures we have confirmed the temperature dependence of the characteristic power level for the decrease of the critical current $P_o(T)$. Near T_c, we have found additional contributions to the decrease of I_{co} arising from the finite length of the microbridge.

At low voltages and near T_c, the heating model predicts that the ac Josephson steps can also be modified strongly by heating effects. Comparisons of these predictions with our

experimental data showed good qualitative agreement with the observed reduction of the maximum height of the first ac step as well as the observation by others of a cut-off frequency of the oscillatory Bessel-function dependence of the step widths. In our well-cooled microbridges, the cut-off frequency is comparable to those used in this work only at temperatures very close to T_c; at very low temperatures it should be of the order of 1 THz.

From the heating model we were able to obtain conditions for the optimum design of variable-thickness microbridges for high frequency applications. We found that a microbridge made from single homogeneous film would not yield any further significant improvement over our best microbridges unless the size could be reduced significantly. However, improvements should be observed in a bi-layer configuration in which the bridge is made of a high resistance material and the banks of a clean material. This geometry should maintain the well-cooled nature of our bridges but would give a smaller dissipation at a given voltage because of the higher resistance. Initial experiments using an approximation to this configuration support this conclusion.

Finally, we believe that experiments using arrays of variable-thickness microbridges could be very useful in improving our understanding of the nature of these devices as well as their interactions. Our initial experiments with

series-biased bridges have shown that closely spaced bridges appear to have significant locking effects even when not independently biased. In one case the observed Josephson steps were abnormally large. One advantage of the variable-thickness geometry seems to be that the interaction of the bridges can be studied over a wider temperature range without simple heating effects overwhelming more subtle nonequilibrium interactions between the bridges.

APPENDIX A

CHARACTERISTIC PROPERTIES OF TIN AND LEAD MICROBRIDGES USED IN THIS REPORT

In this appendix a summary of the characteristic properties of all tin and lead microbridges cited in the text is included for completeness. In many cases, a particular parameter is not included for a microbridge, either because it was not measured or it was not known with sufficient accuracy.

Characteristic Properties of Tin Microbridges

Bridge #	R_N (Ω)	$R_N \frac{dI_{co}}{dT}$ (mV/K)	$I_{co}R_N$(2.1K) (mV)	Exponent of $I_{co}(T)$	Maximum Dayem $\Delta I_{co}/I_{co}$
1	0.15	0.78	1.65	1.50	-
2	0.08		0.80		
3	0.14	0.71	1.75	1.09	0.04
4	0.24	1.37	2.71	1.07	0.24
5	0.27	0.96	4.67	-	-
6	0.40	0.46	1.40	-	-
7	0.43	1.02	1.63	1.03	0.06
8	0.44	0.75	3.30	1.09	0.04
9	0.36	0.56	0.90	1.07	0.11
10	0.85	1.27	1.62	0.87	0.01
11	0.33	0.56	1.32	0.97	0.03
12	1.14	1.05	1.49	1.05	0.08
13	0.09	0.68	1.16	0.87	-
14	0.20	1.16	1.38	1.00	-
15	0.06	0.53	-	1.10	-
16	0.44	0.80	1.19	0.96	0.13
17	1.25	0.69	1.25	-	-
18	0.13	0.77	1.23	-	0.27
19	0.06	0.76	0.88	0.94	-
20	1.76	0.42	1.44	0.91	0.09
21	0.07	0.77	1.10	1.25	0.43
22	0.62	0.43	1.60	1.03	-
23	2.5 [c]	1.0	0.85	-	-

a Microbridge used in far-infrared experiments

b Indicates that not enough power was available to determine V_{max}

c Bilayer bridge as described in Section 5.2.6

Characteristic Properties of Tin Microbridges

Bridge #	I_{c1}/I_{co}	$\bar{I}_s/I_{c1}$	V_{max} (mV)	P_o (μW)	Gap Value (low T) (mV)	Bank Thickness (μm)
1	-	-	0.30	0.10	-	0.1
2			0.63	0.63		1.0
3	1.96	0.70	0.98[b]	1.0	0.73	1.0
4	1.29	0.71	1.5 [b]	1.5	0.56	3.0
5	c	0.71	1.4 [b]	1.2	0.54	3.0
6	-	-	0.70	0.18	0.50	0.1
7	1.28	0.78	1.7	1.2	0.55	1.0
8	1.38	0.70	1.3[b]	0.75	0.50	1.0
9	1.70	0.72	2.3	2.6	0.84	1.0
10	1.19	0.65	2.6	1.7	0.84	1.0
11	1.84	0.72	3.7[b]	8.1	0.86	1.7
12	1.44	0.77	1.6	0.5	0.62	1.0
13	1.67	0.78	-	-	0.50	1.0
14	1.62	0.79	-	-	0.50	1.5
15	2.00	0.77	-	-	-	1.0
16	1.72	0.75	3.7	6.3	0.95	1.5
17	1.59	0.77	> 1.5[a]	-	0.90	1.5
18	1.62	0.72	2.0	4.5	0.73	1.5
19	1.48	0.75	1.5	7.2	0.59	1.5
20	1.28	0.73	2.2	0.6	0.56	1.0
21	1.34	0.74	-	-	0.40	1.0
22	1.20	0.77	-	-	-	1.5
23	1.40	0.71	4.2	2.2	0.98	1.5

Characteristic Properties of Lead Microbridges

Bridge #	R_N (Ω)	I_{co} (4.2K) (mA)	V_{max} (mV)	P_o (μW)	Exponent of $I_{co}(T)$
L-1	0.80	1.87	3.0	2.4	-
L-2	0.16	33.6	1.9	3.8	1.06
L-3	0.60	3.5	1.8	0.98	1.00
L-4	0.08	37.5	1.8	5.9	-
L-5	0.08	20.5	1.8	5.7	-
L-6	0.07	16.8	1.6	5.2	-
L-7	10.0	0.042	No steps	-	-
L-8	0.10	4.1	1.1	2.7	-

REFERENCES

1. P. W. Anderson and A. H. Dayem, Phys. Rev. Lett. 13, 195(1964).

2. P. E. Gregers-Hansen and M. T. Levinsen, Phys. Rev. Lett. 27, 847(1971).

3. P. E. Gregers-Hansen, P. E. Hendricks, M. T. Levinsen, and G. F. Pedersen, Phys. Rev. Lett. 31, 524(1973).

4. W. J. Skocpol, M. R. Beasley, and M. Tinkham, J. Appl. Phys. 45, 4054(1974).

5. V. N. Gubankov, V. P. Koshletes, K. K. Likharev, and G.A. Ovsyannikov, ZhETF Pis. Red. 18, 292(1973) [JETP Lett. 18, 171(1973)].

6. M. Octavio, W. J. Skocpol, and M. Tinkham, to be published, Phys. Rev. B, Jan. 1978.

7. A. A. Golub, Zh. Eksp. Teor. Fiz. 71, 341(1976) [Sov. Phys.-JETP 44, 178(1976)].

8. L. G. Aslamazov and A. I. Larkin, Zh. Eksp. Teor. Fiz. 70, 1340(1976) [Sov. Phys.-JETP, 43, 698(1976)].

9. M. Octavio, W. J. Skocpol, and M. Tinkham, IEEE Trans. MAG-13, 739(1977).

10. M. Tinkham, M. Octavio, and W. J. Skocpol, J. Appl. Phys. 48, 1311 (1977).

11. R. Y. Chiao, M. J. Feldman, H. Ohta, and P. T. Parrish Rev. Phys. Appl. 9, 183(1974).

12. L. B. Holdeman and P. N. Peters, App. Phys. Lett. 28, 632(1976).

13. B. D. Josephson, Phys. Lett. 1, 251(1962).

14. H. A. Notarys and J. E. Mercerau, Proc. of the 1969 Stanford Conference on the Science of Superconductivity [North Holland, Amsterdam (1971)], p. 424.

15. T. W. Wong, J.T.C. Yeh, and D. N. Langenberg, Phys. Rev. Lett. 37, 150(1976).

16. E. P. Harris, IEEE Trans MAG-11, 785(1975); J. Vac. Sci. Tech. 12, 1383(1975).

17. G. J. Dolan and J. E. Lukens, IEEE Trans. MAG-13, 581 (1977).

18. L. G. Aslamazov and A. I. Larkin, JETP Lett. 9, 87 (1969).

19. T. A. Fulton and R. C. Dynes, Phys. Rev. Lett. 25, 794(1970).

20. L. D. Jackel, J. M. Warlamount, T. D. Clark, J. C. Brown, R. A. Buhrman, and M. T. Levinsen, Appl. Phys. Lett. 28, 353(1976).

21. R. C. Sandell, S. S. Pei, and J. E. Lukens. Appl. Superconductivity Conference, Stanford, 1976.

22. V. Ambegaokar and A. Baratoff, Phys. Rev. Lett. 10, 486(1963).

23. K. K. Likharev and L. A. Yakobson, Zh. Tekh. Fiz. 45, 1503(1975). [Sov. Phys. Tech. Phys., 20. 950(1976)].

24. D. Jillie, Ph.D. Thesis, S.U.N.Y., Stony Brook, (1976) (unpublished).

25. T. M. Klapwijk, M. Sepers, and J. E. Mooij, J. Low Temp. Phys. 27, 801(1977).

26. Y. Song and G. I. Rochlin, Phys. Rev. Lett. 29, 416 (1972).

27. L. K. Wong, A. Callegari, B. S. Deaver, D. W. Barr, and R. J. Mattauch, App. Phys. Lett. 31, 306(1977) and private communication.

28. G. M. Daalmans, T. M. Klapwijk, and J. E. Mooij, IEEE Trans. MAG-13, 719(1977).

29. A. Baratoff, J.A. Blackburn, and B. B. Schwartz, Phys. Rev. Lett. 25, 1096(1970).

30. P. V. Christiansen, E.B. Hansen, and C. J. Sjostron, J. Low Temp. Phys. 4, 399(1971).

31. P. G. Gregers-Hansen, M. T. Levinsen, and G. F. Pedersen, J. Low Temp. Phys. 7, 99(1971).

32. I. O. Kulik and A. N. Omelyanchouk, Sov. J. Low. Temp. Phys. (to be published).

33. J. E. Zimmerman, Applied Superconductivity Conference, Annapolis, 1972 (IEEE, CH0682-5-TABSC, New York, 1972), p. 544.

34. I. K. Yanson, Sov. J. Low Temp. Phys. 1, 67 (1975).

35. I. O. Kulik and Omelyanchuk, ZhETF Pis. Red. 21, 216 (1975) [JETP Lett. 21, 96(1975)].

36. Y. N. Mitsai, Sov. J. Low Temp. Phys. 2, 94(1976).

37. A. F. G. Wyatt, V. M. Dmitriev, W. S. Moore, and F. W. Sheard, Phys. Rev. Lett. 16, 1166(1966).

38. A. H. Dayem and J. J. Wiegand, Phys. Rev. 155, 419(1967).

39. S. Shapiro, A. R. Janus, and S. Holly, Rev. Mod. Phys. 36, 223(1964).

40. H. A. Notarys, M. L. Yu, and J. E. Mercerau, Phys. Rev. Lett. 30, 743(1973).

41. B. R. Fjordboge, T. D. Clark, and P. E. Lindelof, Phys. Rev. Lett. 37, 1302(1976).

42. T. Kommers and J. Clarke, Phys. Rev. Lett. 38, 1091 (1977).

43. T. J. Tredwell and E. H. Jacobsen, Phys. Rev. Lett. 35 244(1975); Phys. Rev. B13, 2931(1976).

44. G. M. Eliashberg, JETP Lett. 11, 114(1970); Sov. Phys. JETP. 34, 668(1972).

45. D. W. Jillie, J. Lukens, and Y. W. Kao, IEEE Trans. MAG-11, 671(1971).

46. Yu. I. Latyshev and F. Ya. Nad, IEEE Trans. MAG-11, 877(1975).

47. M. T. Levinsen, Rev. Phys. Appl. 9, 135(1974).

48. T. M. Klapwijk and J. E. Mooij, Physica (Utr.) 81B, 132(1976).

49. T. M. Klapwijk and T. B. Veenstra, Phys. Lett. A47, 351(1974).

50. J. E. Mooij, Private Communication.

51. V. M. Dmitriev, E. B. Khristenko, and S. Shapiro, Fiz. Kondens. Sostoyaniya 28, 3(1973).

52. H. Hojaard Jensen and P. E. Lindelof, J. Low. Temp. Phys. 23, 468(1976).

53. V. N. Gubankov, V. P. Koshelets, and G. A. Ovsyannikov, Zh. Eksp. Teor. Fiz. 71, 348(1976).

54. V. N. Gubankov, V. P. Koshelets and G. A. Ovsyannikov, IEEE Trans. MAG-13, 228(1977).

55. H. A. Notarys and J. E. Mercerau, Physica (Utr.) 55, 424(1971).

56. T. J. Rieger, D. J. Scalapino, and J. E. Mercereau, Phys. Rev. B 6, 1734(1972).

57. W. J. Skocpol, M. R. Beasley, and M. Tinkham, J. Low Temp. Phys., 16, 145(1974).

58. K. K. Likharev and L. A. Yakobson, Zh. Eksp. Teor. Fiz. 68, 1150(1975) [Sov. Phys., JETP, 41, 570(1975)].

59. L. Kramer and A. Baratoff, Phys. Rev. Lett. 38, 518 (1977) and preprint.

60. B. S. Deaver, B. G. Boone, and R. Rifkin, Phys. Lett. 57A, 186(1976).

61. B. S. Deaver, B. G. Boone, and R. Sandell, J. Low Temp. Phys. 25, 409(1976).

62. A. Schmid and G. Schön, J. Low Temp. Phys. 20, 207(1975).

63. A. I. Larkin and Yu. N. Ovchinnikov, Zh. Eksp. Teor. Fiz. 68, 1915(1975) [Sov. Phys. JETP, 41, 960(1975)].

64. M. Tinkham and J. Clarke, Phys. Rev. Lett. 28, 1366 (1972).

65. M. Tinkham, Phys. Rev. B6, 1747(1972).

66. T. M. Klapwijk and J. E. Mooij, Phys. Lett. 57A, 97 (1976).

67. K. K. Likharev, Zh. Eksp. Teor. Fiz. 61, 1700(1971) [Sov. Phys. JETP, 34, 906(1972)].

68. I. K. Yanson, V. M. Svistunov, and I. M. Dimitrenko, Sov. Phys. JETP 21, 650(1965).

69. N. F. Pedersen, O. H. Sorensen, J. Mygind, P. E. Lindelof, M. T. Levinsen, and T. D. Clark, Appl. Phys. Lett. 28, 562(1976).

70. P. Russer, J. App. Phys. 43, 2008(1972).

71. M. J. Renne and D. Polder, Rev. Phys. App. 9, 25(1974).

72. N. R. Werthamer, Phys. Rev. 147, 255(1966).

73. D. A. Weitz, W. J. Skocpol, and M. Tinkham, to be published.

74. T. M. Klapwijk and J. E. Mooij, IEEE Trans. MAG-11, 858(1975).

75. R. Holm, Electrical Contacts (Springer-Verlag, Berlin, 1967), p. 31.

76. F. Kohlrausch, Ann. Phys. (Leipzig) 1, 132(1900).

77. V. Ambegaokar and B. I. Halperin, Phys. Rev. Lett. 22 1364(1969).

78. M. J. Stephen, Phys. Rev. 182, 531(1969); 186, 393 (1969).

79. T. M. Klapwijk and J. E. Mooij, Private communication.

80. T. D. Clark and P. E. Lindelof, Phys. Rev. Lett. 37, 368(1976).

81. L. E. Hasselberg, M. T. Levinsen, and M. R. Samuelsen, J. Low Temp. Phys. 21, 567(1975).

82. L. E. Hasselberg, M. T. Levinsen, and M. R. Samuelsen, Phys. Rev. B9, 3757(1974).

83. O. Hoffman Soerensen, B. Kofoed, N. F. Pedersen, and S. Shapiro, Phys. Rev. B9, 3746(1974).

84. S. A. Schelkunoff and H. T. Friis, Antennas: Theory and Practice, Wiley, New York, 1952, pp. 332-359; 450-454.

85. K. Mizuno, Y. Daiku, and S. Ono, IEEE Trans. MIT-25, 470(1977).

86. D. R. Tilley, Phys. Lett. 33A, 205(1970).

87. T. F. Finnegan and S. Wahlsten, Low Temperature Physics, LT-13, Vol. 3, edited by K. D. Timmerhaus, W. J. O'Sullivan and E. F. Hammel (Plenum Pub. Corp., New York), 1974, p. 272.

88. D. W. Palmer and J. E. Mercereau, Phys. Lett. 61A, 135(1977).

89. D. W. Jillie, J. E. Lukens, and Y. H. Kao, Phys. Rev. Lett. 38, 915(1977).

90. D. W. Jillie, J. E. Lukens, Y. H. Kao, and G. J. Dolan, Phys. Lett. 55A, 381(1976).

91. P. E. Lindelof and J. Binslev Hansen, preprint.

ACKNOWLEDGEMENTS

I would like to thank Professors M. Tinkham and W. J. Skocpol for their encouragement and help during all phases of this work. Their many insights and contributions have been invaluable to the author.

I would like to acknowledge the members of the superconductivity group at Harvard, past and present, for their technical help and for providing comic relief when it was needed. In particular, I would like to thank Dr. L. N. Smith for numerous discussions and D. A. Weitz for his help with the far-infrared experiments. The machining expertise of L. DeFeo, R. Rex and J. Keith, as well as the help of the staff of Gordon McKay Laboratories is gratefully acknowledged.

I would like to thank my wife Kathy for her patience, love, and encouragement at all stages of this work.

The Instituto Venezolano de Investigaciones Cientificas provided financial support during my years of graduate work. This work has been supported in part by the National Science Foundation, the Office of Naval Research and the Joint Services Electronic Program.

DISTRIBUTION LIST FOR ONR ELECTRONIC AND SOLID STATE SCIENCES

Director
Advanced Research Projects Agency
Attn: Technical Library
1400 Wilson Boulevard
Arlington, Virginia 22209

Office of Naval Research
Electronics Program Office (Code 427)
800 North Quincy Street
Arlington, Virginia 22217

Office of Naval Research
Code 105
800 North Quincy Street
Arlington, Virginia 22217

Director
Naval Research Laboratory
4555 Overlook Avenua, S.W.
Washington, D.C. 20375
Attn: Technical Library (6 cps)
Code 5200 (1 copy)
5210 (1 copy)
5270 (1 copy)
6400 (1 copy)

Office of the Director of Defense
Research and Engineering
Office of the Assistant Director
Electronics & Physical Sciences
The Pentagon, Room 3D1079
Washington, DC 20301

Defense Documentation Center (12 cps)
Cameron Station
Alexandria, Virginia 22314

Commanding Officer
Office of Naval Research Branch Office
536 South Clark Street
Chicago, Illinois 60605

San Francisco Area Office
Office of Naval Research
50 Fell Street
San Francisco, California 94102

Commanding Officer
Office of Naval Research Branch Office
1030 East Green Street
Pasadena, California 91101

Commanding Officer
Office of Naval Research Branch Office
495 Summer Street
Boston, Massachusetts 02210

New York Area Office
Office of Naval Research
115 Broadway 5th Floor
New York, New York 10003

ODDR&E Advisory Group on Electron Devices
201 Varick Street
New York, New York 10014

Naval Air Development Center
Attn: Technical Library
Johnsville
Warminster, Pennsylvania 18974

Naval Weapons Center
China Lake, Califronia 93555
Attn: Technical Library (1 copy)
Code 6010 (1 copy)

Naval Research Laboratory
Underwater Sound Reference Division
Technical Library
P.O. Box 8337
Orlando, Florida 32806

Navy Underwater Sound Laboratory
Technical Library
Fort Trumbull
New London, Connecticut 06320

Commandant, Marine Corps
Scientific Advisor (Code AX)
Washington, D.C. 20380

Naval Ordnance Station
Technical Library
Indian Head, Maryland 20640

Naval Postgraduate School
Monterey, California 93940
Attn: Technical Library (1 copy)
Elect. Engin. Depart. (1 copy)

Naval Missile Center
Technical Library (Code 5632.2)
Point Mugu, California 93010

Naval Electronics Laboratory Center
San Diego, California
Attn: Technical Library (1 copy)
Code 2300 (1 copy)
2600 (1 copy)
4800 (1 copy)

Naval Undersea Center
Technical Library
San Diego, California 92132

Naval Weapons Laboratory
Technical Library
Dahlgren, Virginia 22448

Naval Ship Research and Development Center
Central Library (Codes L42 and L43)
Washington, D.C. 20007

Naval Surface Weapons Center
White Oak Laboratory
Silver Spring, Maryland 20910
Attn: Technical Library (1 copy)
Code 200 (1 copy)
212 (1 copy)

Deputy Chief of Naval Operations
(Development)
Technical Analysis and Advisory Group
(Code NOP-077D)
Washington, D.C. 20350

Commander
Naval Air Systems Command
Washington, D.C.
ATTN: Code 310 (1 copy)
360 (1 copy)

Commander
Naval Electronics Systems Command
Washington, D.C. 20360
Attn: Code 304 (1 copy)
310 (1 copy)

Commander
Naval Sea Systems Command
Washington, D.C. 20360

Naval Surface Weapons Center
Attn: Library
Dahlgren, Virginia 22448

Air Force Office of Scientific Research
Attn: Electronic and Solid State
Sciences Division
Department of the Air Force
Washington, D.C. 20333

Air Force Weapon Laboratory
Technical Library
Kirtland Air Force Base
Albuquerque, New Mexico 87117

Air Force Avionics Laboratory
Air Force Systems Command
Technical Library
Wright-Patterson Air Force Base
Dayton, Ohio 45433

Air Force Cambridge Research Laboratory
L.G. Hanscom Field
Technical Library
Cambridge, Massachusetts 02138

Harry Diamond Laboratories
Technical Library
Connecticut Avenue at Van Ness, N.W.
Washington, D.C. 20438

U.S. Army Research Office
Box CM, Duke Station
Durham, North Carolina 27706

Director
U.S. Army Engineering Research
and Development Laboratories
Fort Belvoir, Virginia 22060
Attn: Technical Documents Center

Director National Bureau of Standards
Attn: Technical Library
Washington, D.C. 20234

Naval Research Laboratory
4555 Overlook Avenue, S.W.
Washington, D.C. 20375
Attn: Code 5300 (1 copy)
7100 (1 copy)
7900 (1 copy)

Naval Electronics Laboratory Center
San Diego, California 92152
Attn: Code 2100 (1 copy)
2200 (1 copy)

C.C. Klick
Superintendent
Materials Sciences Division
Naval Research Laboratory
4555 Overlook Avenue, S.W.
Washington, D.C. 20375

Naval Research Laboratory
4555 Oberlook Avenua, S.W.
Washington, D.C. 20375
Attn: Code 5220 (1 copy)
5230 (1 copy)
5250 (1 copy)
5260 (1 copy)
5270 (1 copy)
5500 (1 copy)

Naval Electronics Laboratory Center
San Diego, California 92152
Attn: Code 2500 (1 copy)
4000 (1 copy)

Office of Naval Research (2 cps)
800 N. Quincy Street
Arlington, Virginia 22217
Attn: Code 430 (2 copies)

Naval Research Laboratory
4555 Overlook Avenue, S.W.
Washington, D.C. 20375
Attn: Code 5400

Naval Electronics Laboratory Center
San Diego, California 92152
Attn: Code 3000 (1 copy)
5000 (1 copy)
5600 (1 copy)

Air Force Office of Scientific Research
Mathematical and Information Sciences
Directorate
1400 Wilson Blvd.
Washington, D.C. 20333

JSEP MEPhase DISTRIBUTION LIST

Director
National Security Agency
ATTN: Dr. T. J. Beahn
Fort George G. Meade, MD 20755

Defense Documentation Center
ATTN: DDC-TCA (Mrs. V. Caponio)
Cameron Station
Alexandria, VA 22314

Asst. Dir.
Office of Director of Defense
Research and Engineering
The Pentagon
Washington, DC 20315

Defense Advanced Research
Projects Agency
ATTN: (Dr. R. Reynolds)
1400 Wilson Boulevard
Arlington, VA 22209

Commandant
US Army Air Defense School
ATTN: ATSAD-T-CSM
Fort Bliss, TX 79916

Commander
US Army Armament R&D Command
ATTN: DRDAR-SC
Dover, NJ 07801

Commander
US Army Ballistic Research Lab.
ATTN: DRXBR-BAD
Aberdeen Proving Ground
Aberdeen, MD 21005

Commandant
US Army Command and General
Staff College
ATTN: Acquisitions, Lib. Div.
Fort Leavenworth, KS 66027

Commander
US Army Communication Command
ATTN: CC-OPS-PE
Fort Huachuca, AZ 85613

Commander
US Army Materials and Mechanics
Research Center
ATTN: Chief, Materials Sciences
Division
Watertown, MA 02172

Commander
US Army Material Development
and Readiness Command
ATTN: Technical Library, Bn.7S 15
5001 Eisenhower Avenue
Alexandria, VA 22333

Commander
US Army Missile R&D Command
ATTN: Chief, Document Section
Redstone Arsenal, AL 35809

Commander
US Army Satellite Communications
Agency
Fort Monmouth, NJ 07703

Commander
US Army Security Agency
ATTN: IAMG-C
Arlington Hall Station
Arlington, VA 22212

Project Manager
AFTADS
EAT Building
West Long Branch, NJ 07764

Commander/Director
Atmospheric Sciences Lab. (DELAS)
ATTN: DELAS-BL-DD
White Sands Missile Range, NM 88002

Commander
US Army Electronics Command
ATTN: DRSEL-RD-C (Dr. R.G. Bennett)
Fort Monmouth, NJ 07703

Director
NSA/CSS
ATTN: PT-AC (Mrs. Brilley)
Fort Monmouth, NJ 07703

Commander
US Army Electronics Command
ATTN: DRSEL-CT-L (Dr. K. Bure)
Fort Monmouth, NJ 07703

Director
Electronic Warfare Lab. (DELEW)
ATTN: DRSEL-WL-MY
White Sands Missile Range, NM 88002

Executive Secretary, TAC/JSEP
U. S. Army Research Office
P.O. Box 12211
Research Triangle Park, NC 27709

Commander
Frankford Arsenal
Deputy Director,
Pitman-Dunn Laboratory
Philadelphia, PA 19137

Project Manager
Ballistic Missile Defense Program Office
ATTN: (BMDP-BMP (Dr. A. Gold)
1300 Wilson Blvd.
Arlington, VA 22209

Commander
Harry Diamond Laboratories
ATTN: Dr. John E. Rosenberg
2800 Powder Mill Road
Adelphi, MD 20783

NSEA (Code-AXS-A)
Washington, DC 20310

Commander
US Army Electronics Command
Fort Monmouth, NJ 07703
ATTN: DRSEL-TL-E (Dr. I.A. Kohn)
DRSEL-TL-EM (Dr. A. Kronenberg)
DRSEL-NL-T (Mr. A. Rolley)
DRSEL-NL-A (Dr. P. Liebelt)
DRSEL-TL-MP (Dr. M. Lipsky)
DRSEL-NL-C (Dr. W.S. McAfee)
DRSEL-NL-R (Dr. D.C. Pearce)
DRSEL-NL-RH-1 (Dr. F. Schwering)
DRSEL-TL-I (Dr. C.O. Thornton)

CDR Robert Moss
Senior Standardization Representative
US Army Standardization Group, Canada
Canadian Forces Headquarters
Ottawa, Ontario, Canada K1A 0K2

Director
Night Vision Laboratory
ATTN: DRSEL/NV-D
Fort Belvoir, VA 22060

Commander
Picatinny Arsenal
ATTN: SMCPA-TS-T-S
Dover, NJ 07801

Dr. Sidney Ross
Technical Director
SARPA-TS
Frankford Arsenal
Philadelphia, PA 19137

US Army Research Office (Ispe)
ATTN: Library
P.O. Box 12211
Research Triangle Park, NC 27709

Director
Division of Neuropsychiatry
Walter Reed Army Institute of
Research
Washington, DC 20012

Commander
White Sands Missile Range
ATTN: STEWS-ID-R
White Sands Missile Range, NM 88002

Mr. Robert Barrett
AADC/DTA
Hanscom AFB, MA 01731

Dr. Carl E. Baum
AFWL (NS)
Kirtland AFB, NM 87117

Dr. E. Champagne
AFAL/DH
Wright-Patterson AFB, OH 45433

Dr. R. E. Dolan
RADC/ETSD
Hanscom AFB, MA 01731

Mr. W. Edwards
AFAL/TS
Wright-Patterson AFB, OH 45433

Professor K.E. Fontana
Head, Dept. of Electrical Eng
AFIT/ENH
Wright-Patterson AFB, OH 45433

Dr. Alan Garscadden
AFAPL/POD
Wright-Patterson AFB, OH 45433

USAF European Office of Aerospace
Research
ATTN: Major J. Worrell
Box 14, FPO, New York 09510

LTC Richard J. Gowen
Dept. of Electrical Engineering
USAF Academy, CO 80840

Mr. Murray Kesselman (ISCP)
Rome Air Development Center
Griffiss AFB, NY 13441

Dr. G. Knausenberger
Air Force Member, TAC
Air Force Office of Scientific
Research
(AFSC) AFOSR/NE
Bolling Air Force Base, DC 20332

Dr. C. Krenitz
Air Force Member, TAC
Air Force Office of Scientific
Research
(AFSC) AFOSR/NE
Bolling Air Force Base, DC 20332

Mr. R. D. Larson
AFAL/TAN
Wright-Patterson AFB, OH 45433

Dr. Richard B. Mack
RADC/ETSD
Hanscom AFB, MA 01731

Mr. John Mottmith (MCIT)
HQ ESD (AFSC)
Hanscom AFB, MA 01731

Dr. Richard Picard
RADC/ETSL
Hanscom AFB, MA 01731

Dr. J. Ryles
Chief Scientist
AFAL/CA
Wright-Patterson AFB, OH 45433

Dr. Allan Schell
RADC/ETE
Hanscom AFB, MA 01731

Mr. W.E. Wade, Jr. (ISCP)
Rome Air Development Center
Griffiss AFB, NY 13441

LTC G. Hopfer
Air Force Office of Scientific
Research
(AFSC) AFOSR/NP
Bolling Air Force Base, DC 20332

LTC G. McKenzie
Air Force Office of Scientific
Research
(AFSC) AFOSR/NM
Bolling Air Force Base, DC 20332

Dr. R. E. Allenby
Naval Surface Weapons Center
Code WR-307
White Oak
Silver Spring, MD 20910

Naval Weapons Center
ATTN: Code 5515 - R.F. Kiesz
China Lake, CA 93555

Dr. A. L. Slafkosky
Technical Director
Naval Ordnance Center
San Diego, CA 92152

Naval Research Laboratory
4555 Overlook Avenue, SW
Washington, DC 20375
ATTN: Code 5200 - A. Brodzinsky
Code 7701 - J. D. Brown
Code 5210 - J. E. Davey
Code 5460/5410 - J.H. Davis
Code 5510 - W. L. Faust
Code 2627 - Mrs. D. Folen

Naval Ocean Systems Center
ATTN: Code 75 - W.J. Deija
271 Catalina Boulevard
San Diego, CA 92152

Naval Weapons Center
ATTN: Code 601 - F.C. Essig
China Lake, CA 93555

Dr. Robert K. Fossum
Dean of Research
Naval Postgraduate School
Monterey, CA 93940

Dr. D. G. Gould
Technical Director
Naval Coastal System Lab.
Panama City, FL 32401

Naval Ocean Systems Center
ATTN: Code 7203 - V.E. Hildebrand
271 Catalina Boulevard
San Diego, CA 92152

Naval Ocean Systems Center
ATTN: Code 733 - F.A. Johnson
271 Catalina Boulevard
San Diego, CA 92152

Donald E. Kirk
Professor and Chairman
Electrical Engineer, EF-304
Naval Postgraduate School
Monterey, CA 93940

Naval Air Development Center
ATTN: Code 01 - Dr. R. E. Lobb
Johnsville
Warminster, PA 18974

Naval Research Laboratory
ATTN: Code 5270 - H.D. McCombs
4555 Overlook Avenue, SW
Washington, DC 20375

Capt. R.B. Meeks
Naval Sea Systems Command
SC #3
3351 Jefferson Davis Hwy
Arlington, VA 20362

Dr. R. J. Mueller
Naval Air Systems Command
Code 310
JP #1
1411 Jefferson Davis Hwy
Arlington, VA 20360

Dr. J.M. Mills, Jr.
Naval Surface Weapons Center
Electronics Systems Department
Code DF
Dahlgren, VA 22448

Naval Ocean Systems Center
ATTN: Code 702 - W.T. Mortimer
271 Catalina Boulevard
San Diego, CA 92152

Naval Air Development Center
ATTN: Technical Library
Johnsville
Warminster, PA 18974

Naval Ocean Systems Center
ATTN: Technical Library
271 Catalina Boulevard
San Diego, CA 92152

Naval Research Laboratory
Underwater Sound Reference Division
Technical Library
P.O. Box 8337
Orlando, FL 32806

Naval Surface Weapons Center
ATTN: Technical Library
Code DX-21
Dahlgren, VA 22448

Naval Surface Weapons Center
ATTN: Technical Library
Building 1-130, Code WR-40
White Oak
Silver Spring, MD 20910

Naval Training Equipment Center
ATTN: Technical Library
Orlando, FL 32813

Naval Undersea Center
ATTN: Technical Library
San Diego, CA 92152

Naval Underwater Systems Center
ATTN: Technical Library
Newport, RI 02840

Office of Naval Research
Electronic & Solid State Sciences
Program (Code 427)
800 North Quincy Street
Arlington, VA 2217

Office of Naval Research
Mathematics Program (Code 432)
800 North Quincy Street
Arlington, VA 22217

Office of Naval Research
Naval Systems Division
Code 220/221
800 North Quincy Street
Arlington, VA 22217

Director
Office of Naval Research
New York Area Office
715 Broadway, 5th Floor
New York, NY 10003

Office of Naval Research
San Francisco Area Office
One Hallidie Plaza - Suite 601
San Francisco, CA 94102

Director
Office of Naval Research Branch
Office
495 Summer Street
Boston, MA 02210

Director
Office of Naval Research Branch
Office
536 South Clark Street
Chicago, IL 60605

Director
Office of Naval Research Branch
Office
1030 East Green Street
Pasadena, CA 91101

Mr. H. R. Riedl
Naval Surface Weapons Center
Code WR-14
White Oak Laboratory
Silver Spring, MD 20910

Naval Air Development Center
ATTN: Code 202 - T. J. Shopple
Johnsville
Warminster, PA 18974

Naval Research Laboratory
ATTN: Code 5403-J. E. Shore
4555 Overlook Avenue, SW
Washington, DC 20375

A. L. Slafkosky
Scientific Advisor
Headquarters Marine Corps
HC-RD-1
Arlington Annex
Washington, DC 20380

Harris R. Stone
Office of Research, Development,
Test and Evaluation
NSP-987
The Pentagon, Room 5D760
Washington, DC 20350

Mr. L. Sumney
Naval Electronics Systems Command
Code 3042, MC #1
3511 Jefferson Davis Hwy
Arlington, VA 20360

David M. Taylor
Naval Ship Research and
Development Center
Code 522.1
Bethesda, MD 20084

Naval Research Laboratory
ATTN: Code 4105-Dr. S. Teitler
4555 Overlook Avenue, SW
Washington, DC 20375

LA Cdr. John Turner
NAVMAT 0161
CP #5, Room 1044
3311 Jefferson Davis Hwy.
Arlington, VA 20360

Naval Ocean Systems Center
ATTN: Code 746-R.E. Wiebe
271 Catalina Boulevard
San Diego, CA 92152

Dr. W. A. Von Winkle
Associate Technical Director
for Technology
Naval Underwater Systems Center
New London, CT 06320

Dr. Gernot M. R. Winkler
Director, Time Service
US Naval Observatory
Massachusetts Avenue at
34th Street, NW
Washington, DC 20390

Dr. Howard W. Wood
Deputy Director
Division of Materials Research
National Science Foundation
1800 G Street
Washington, DC 20550

Mr. J. C. French
National Bureau of Standards
Electronics Technology Division
Washington, DC 20234

Dr. Jay Harris
Program Director
Devices and Waves Program
National Science Foundation
1800 G Street
Washington, DC 20550

Los Alamos Scientific Laboratory
ATTN: Reports Library
P.O. Box 1663
Los Alamos, NM 87544

Dr. Dean Mitchell
Program Director
Solid-State Physics
Division of Materials Research
National Science Foundation
1800 G Street
Washington, DC 20550

Mr. P. C. Schwenk, RD-T
National Aeronautics and Space
Administration
Washington, DC 20546

M. Rene Thornton
Deputy Director,Institute for
Computer Sciences and Technology
National Bureau of Standards
Washington, DC 20234

Director
Columbia Radiation Laboratory
Columbia University
538 West 120th Street
New York, NY 10027

Director
Coordinated Science Laboratory
University of Illinois
Urbana, IL 61801

Director of Laboratories
Division of Applied Sciences
Harvard University
Pierce Hall
Cambridge, MA 02138

Director
Electronics Research Center
The University of Texas
Engineering-Science Bldg. 112
Austin, TX 78712

Director
Electronics Research Laboratory
University of California
Berkeley, CA 94720

Director
Electronics Sciences Laboratory
University of Southern California
Los Angeles, CA 90007

Director
Microwave Research Institute
Polytechnic Institute of New York
333 Jay Street
Brooklyn, NY 11201

Director
Research Laboratory of Electronics
Massachusetts Institute of
Technology
Cambridge, MA 02139

Director
Stanford Electronics Laboratory
Stanford University
Stanford, CA 94305

Stanford Ginzton Laboratory
Stanford University
Stanford, CA 94305

Office in Charge
Cardbyrak Laboratory
Code 18-G.R. Cleteanu
David Taylor Naval Ship Research
and Development Center
Bethesda, MD 20084

Dr. Ray F. Rutter
3868 Talbot Street
San Diego, CA 92106